

**Observation of Forces on Microparticles
in Acoustic Standing Waves**

BY

ANDREW HANCOCK

B.E. (State University of New York, Stony Brook)

P.E. (New York State Department of Education, Albany)

THESIS

Submitted in partial satisfaction of the requirements for the degree of

MASTER OF SCIENCE

in

Biomedical Engineering

in the

OFFICE OF GRADUATE STUDIES

of the

UNIVERSITY OF CALIFORNIA

DAVIS

Approved:

Michael F. Insana

Katherine W. Ferrara

Scott I. Simon

John S. Allen

Committee in Charge

2001

DEDICATION

To Mom, Dad, and my sisters Gwen and Adrienne.

SECOND DEDICATION

To those innocents who lost their lives in
New York City, Washington D.C. and in the air
on September 11, 2001.

God Bless America.

A WORD ABOUT THIS WORK:

Captain, we have to take the Mains offline...

it's radiation.

Scotty

ACKNOWLEDGMENTS

I would like to thank everyone in the UC Davis Ultrasound research and Cellular Mechanics research laboratories for their assistance in the development of this work. From Dr. Michael F. Insana's research laboratory, Jerome J. Mai for his skill in cooking up low attenuation phantoms, and Dr. Christian Kargel for his help in developing the Labview VIs for the Parker Daedal XYZ positioner. From Dr. Katherine W. Ferrara's research laboratory, Dustin E. Kruse and Paul A. Dayton for their invaluable suggestions and material and equipment loans. Special mention must also be given to Dr. John S. Allen for his insights into radiation force theory. And grateful appreciation to Dr. Michael F. Insana for his patience and understanding. No research occurs without financial support, which came partially in the form of a grant from the National Institute of Health, NIH R01 CA82497.

Davis, California
November 9, 2001

Andrew Hancock

TABLE OF CONTENTS

1	INTRODUCTION	1
1.1	Approach	1
1.2	Erythrocyte Sedimentation and Cellular Adhesion	1
1.3	Plug Flow Cytometry	5
1.4	Atomic Force Microscopy	6
1.5	Laser Tweezers	7
1.6	Ultrasound	11
1.7	Research Goals	15
1.7.1	Hypotheses and Objectives	16
2	RADIATION FORCE: ANALYSIS AND REVIEW	18
2.1	1D Analysis of the Radiation Field	18
2.1.1	Pressure	18
2.1.2	Forces	22
2.2	2D Analysis of the Radiation Field	29
2.2.1	Pressure	29
2.2.2	Forces	30
2.3	Prediction of Medium Pressure from Piston Radiators	35

3	ORDER-OF-MAGNITUDE ANALYSIS OF FORCES	39
3.1	Viscous and Thermal Dissipation	39
3.2	Secondary Radiation Forces	39
3.3	Acoustic Streaming	43
3.4	Thermal Convection	44
3.5	Viscous Drag Forces	44
3.6	Pressure Field Distortion	45
3.7	Brownian Motion and Diffusion	46
3.8	Influence of Hydrostatic Pressure Gradients	46
3.9	Cavitation and Rectified Diffusion	46
4	ENGINEERING DESIGN & METHODS OF STUDY	49
4.1	Chamber Design	49
4.2	Methods of Study	55
4.2.1	Pressure Fields and Forces	58
4.2.2	Hydrophone Selection	60
4.2.3	Particle Levitation	61

5	STANDING WAVE PRESSURE FIELDS	67
5.1	Method	67
5.2	Results	73
5.3	Discussion	79
6	THE FORCE MODEL	85
6.1	Method	85
6.2	Results	86
6.3	Discussion	97
7	LEVITATION EXPERIMENTS	102
7.1	Method	102
7.2	Results	103
7.3	Discussion	107
8	FUTURE RESEARCH	118
8.1	Prediction of the Pressure Field	118
8.2	Extension of the Force Model	119
8.3	Chamber Redesign	119
8.4	Measurement of Molecular Bonds	122
9	CONCLUSIONS	124

LIST OF FIGURES AND PHOTOGRAPHS

1	Chamber Geometry	19
2	Primary Radiation Force	26
3	Column Formation	36
4	Geometry associated with Secondary Radiation Forces	41
5	Chamber Assembly Schematic	51
6	Water Jet	53
7	Electrical Schematic for Chamber Operation	56
8	Water Height Measurement Electrical Schematic	57
9	Hydrophone Assemblies for Pressure Mapping	59
10	Chamber with Low-Attenuation Phantom	65
11	Traveling Wave Pressure Field	68
12	Standing Wave Pressure Field	70
13	Standing Wave Pressure Beam Contour	71
14	Pressure Mapping Experimental Setups	74
15	Transducer Pressure Characteristics	76
16	Standing Wave Pressure Beam Contour - Far Field	77
17	Standing Wave Pressure Field Axial Profile	78
18	Spectral Density of the Standing Wave Pressure Field	80

19	Standing Wave Pressure Field Lateral Profiles	81
20	Axial Forces Predicted by the Force Model	88
21	Lateral Forces Predicted by the Force Model	89
22	Predicted Isobutane Columns	94
23	Predicted Polystyrene Columns	95
24	Predicted Glycerine Columns	96
25	Predicted Red Blood Cell Columns	97
26	Levitated Air	105
27	Levitated Isobutane	106
28	Levitated Polystyrene	108
29	Levitated Cornstarch	109
30	Levitated Isobutane and Polystyrene	110
31	Levitated Polystyrene Ring	111
32	Levitated Food Coloring	112
33	Levitated Glycerine	113
34	Levitated Glycerine Columns	114

LIST OF TABLES

1	Particle Levitation Examples	14
2	Summary of Major Forces for 3 Particles	48
3	Transducer Design Specifications	52
4	Chamber and Medium Material Properties	54
5	Hydrophone Cross-calibration	62
6	Particle Properties	63
7	Phantom Recipe Ingredients and Proportions	66
8	Phantom Attenuation Measurements	66
9	Standing Wave Model Parameters	72
10	Locations of Maximum Pressure	76
11	Axial Force Predictions	90
12	Lateral Force Predictions	91
13	Force Predictions	92
14	Column Formation Predictions	93
15	Measured verse Predicted Minimum Trap Pressures	115

ABSTRACT

Motivated by current work of biologists towards an understanding of intercellular adhesion processes, development has begun on a novel ultrasonic device for measurement of molecular bond rupture strengths among biologic cells. In contrast to atomic force microscopy and laser tweezers, it is intended that the device can be easily used with large populations of particles to ensure statistical validity of the measurements. The principal components of the device are an acoustic levitation chamber that utilizes a standing wave pressure field to trap cell-sized particles. Also key are pressure and force models developed from acoustic theory and with the aid of the Field II simulation program. The models have been successfully used to predict the pressure field, particle forces and particle column locations and dimensions. These predictions are important because they could be used to design experiments that reveal cellular bonding mechanics and predict molecular bond rupture strengths.

The chamber components are a cylindrical plexiglas tank filled with deionized, degassed water, and a 19 mm, unfocussed piezoelectric immersion transducer operating near 500 kHz. Stable standing wave pressure fields have been generated in the chamber using continuous waves (CW) and CW bursts, and mapped with a calibrated 0.4 mm aperture polymer needle hydrophone. Within the field, particles experience radiation forces that are a function of the particle volume and relative particle acoustic properties, and is proportional to the gradient of the acoustic field intensity. The field intensity in turn depends on the transducer and chamber design parameters and the medium acoustic properties. The radiation force can be controlled to counter-

act other particle forces such as buoyancy, thus allowing capture of the particles at pressure nodes or antinodes within the pressure field.

Experimental demonstration of these principles has been achieved through particle levitation experiments using gas-phase, solid particles and liquids. Based on the knowledge gained, changes to the chamber design and force and pressure models are discussed that will allow measurement of molecular bond rupture strengths among biologic cells.

Keywords: acoustic standing wave chamber, acoustic levitation chamber, particle column formation, particle levitation, radiation force

Andrew Hancock
November, 2001
Biomedical Engineering

Observation of Forces on Microparticles in Acoustic Standing Waves

Abstract

Motivated by current work of biologists towards an understanding of intercellular adhesion processes, development has begun on a novel ultrasonic device for measurement of molecular bond rupture strengths among biologic cells. In contrast to atomic force microscopy and laser tweezers, it is intended that the device can be easily used with large populations of particles to ensure statistical validity of the measurements. The principal components of the device are an acoustic levitation chamber that utilizes a standing wave pressure field to trap cell-sized particles. Also key are pressure and force models developed from acoustic theory and with the aid of the Field II simulation program. The models have been successfully used to predict the pressure field, particle forces and particle column locations and dimensions. These predictions are important because they could be used to design experiments that reveal cellular bonding mechanics and predict molecular bond rupture strengths.

The chamber components are a cylindrical plexiglas tank filled with deionized, degassed water, and a 19 mm, unfocussed piezoelectric immersion transducer operating near 500 kHz. Stable standing wave pressure fields have been generated in the

chamber using continuous waves (CW) and CW bursts, and mapped with a calibrated 0.4 mm aperture polymer needle hydrophone. Within the field, particles experience radiation forces that are a function of the particle volume and relative particle acoustic properties, and is proportional to the gradient of the acoustic field intensity. The field intensity in turn depends on the transducer and chamber design parameters and the medium acoustic properties. The radiation force can be controlled to counteract other particle forces such as buoyancy, thus allowing capture of the particles at pressure nodes or antinodes within the pressure field.

Experimental demonstration of these principles has been achieved through particle levitation experiments using gas-phase, solid particles and liquids. Based on the knowledge gained, changes to the chamber design and force and pressure models are discussed that will allow measurement of molecular bond rupture strengths among biologic cells.

Keywords: acoustic standing wave chamber, acoustic levitation chamber, particle column formation, particle levitation, radiation force

Approval of Committee Chairperson:

Michael F. Insana

1. INTRODUCTION

1.1. Approach

Biomedical research engineers are often responsible for the development of new instrumentation to explore biological processes. A strategy is to develop novel instruments that examine features of biological systems which offer insights into mechanisms of normal function and disease, and aid in understanding the physical basis of biological processes. This thesis describes work in understanding how to generate and control forces in the fN to μN (10^{-15} to 10^{-6} Newtons) range, and designing a first generation ultrasonic device to accomplish this. Through understanding of the physics of acoustic forces, future generations of this device may be used to investigate cellular processes including rheology and adhesion.

The contribution of this thesis is to assemble known mathematical theories of acoustic radiation with simulation software to predict the forces in an experimental particle levitation chamber. The conditions under which the theory is valid are carefully analyzed, and the force predictions are tested with a series of experiments to establish the feasibility of the approach. Consequently, this thesis is an experimental study of acoustic radiation theory, and represents the application of basic physical equations applied to engineering design and development.

1.2. Erythrocyte Sedimentation and Cellular Adhesion

Erythrocyte sedimentation is the process erythrocytes undergo as they settle out of plasma. The erythrocyte sedimentation rate (ESR) is easily measured and is therefore

often used by clinicians as a non-specific indicator of infectious, inflammatory, and malignant disease states.^{1,2} Clinical levels of ESR for healthy men and women under the age of 50 are < 15 and < 20 mm/hr respectively. ESR is deemed significant when elevated above 40 mm/hr, but because it is a non-specific indicator it is not used to screen for disease unless other patient symptoms are present. However, 90% of patients with ESR > 100 mm/hr had a serious underlying disease.^{3,4}

ESR is measured by the Westergren method that involves placing a blood sample within a tube 200 mm high by 2.5 to 3 mm diameter at 22 °C. The tube is set on a vibration-free table for one hour. After that time, the amount of sedimentation is recorded within a 0.5 mm resolution.² There are three phases of sedimentation. During the initial phase (Phase 1) red blood cells in suspension coagulate in a spontaneously ordered fashion forming spheres known as rouleaux. Phase 2 is a decantation phase in which the red blood cells and other particles precipitate out of the suspension. During Phase 3 the red blood cells pack more tightly at the tube base.^{1,2}

The ESR is highly dependent on the ability of erythrocytes to form rouleaux. An increase in hematocrit or plasma osmolality results in a proportional decrease in ESR.⁵ The ESR varies in a logarithmic manner with macromolecule concentrations (e.g. fibrinogen and plasma proteins).¹ There is also evidence that high strength magnetic fields increase ESR, though not proportionally,⁶ and that the viscoelastic properties of red blood cells affect ESR.⁷ For each of the above factors, the mechanism suggested to explain these changes is that each factor affects the ability of red blood

cells to form rouleaux. So why is rouleaux formation important in identifying disease states?

It turns out a key component of rouleaux formation is the adherence capability of erythrocytes. Increases in cell-cell interactions, aided by bridging functions of macromolecules, results in increased rouleaux formation. Similarly, increases in the concentration of macromolecules such as fibrinogen and other plasma proteins will increase rouleaux formation due to an increase in availability of adhesion molecules. Hematocrit over an optimal range lead to the highest rouleaux formation and ESR, because the cells are freer to reorient themselves as needed for the adhesion process.⁶ And any increase in the capability of red blood cells to adhere to one another, due to conformational changes in the molecular bonds, will also lead to larger rouleaux size and higher ESR.⁷

In some cases diseases are associated with a lowered ESR. In sickle cell disease, abnormally shaped red blood cells interfere in rouleaux formation and slow sedimentation.³ High shear rates in parallel plate flow chambers has also been shown to decrease cell-cell interactions and decrease sedimentation,⁸ suggesting shear stresses play an important role as mediators by affecting the morphology and functional phenotype of the cell via regulation of gene expression through 2nd messenger chemical pathways originating at the cell membrane.

All of the factors mentioned influence ESR, and so are correlated with disease. If they are not factors eliciting disease, they may at least be considered a direct consequence of disease. As an example, low perturbation and oscillating shear stresses

have been implicated in atherosclerosis.⁹ The key process in each of these factors is the cell molecular bond interactions, which are also important to other pathologies. Atherosclerosis is partially a consequence of adhesive bond formation between macromolecules and leukocytes with endothelial cells. Conformational changes in the adhesion molecules are thought to contribute to increased binding to endothelial cells.⁸

Clearly, the study of the molecular bonds in the adhesion process is very important. Molecular bonds can take on a number of conformations (shapes). They have multiple degrees of freedom making them difficult to characterize; they can rotate, fold, wind, hook, latch, etc. However, because of their complexity each bond is unique, a fingerprint, and knowledge of the molecular bond properties can help in identification of the molecules involved.

The conformational changes of the molecules make force-extension curves (similar to load-displacement curves used on a macroscale in materials testing) the best means to characterize the bonds. The shape of the curve depends on the number of bonds and the conformational changes undertaken by the molecules. Integration of the curve will determine the mechanical energy applied to the molecular bond, but usually is much higher than the binding energy. Most of the mechanical energy is absorbed and used to work against molecular thermal motions, and only a fraction of the energy is applied to break the bond.¹⁰ The curve also provides information on the molecular extension, deformation, bond strengths (yield and rupture) and lifetime. Interestingly, this information is not fixed. It turns out that variations in the load

rate (or pulling speed) affect molecular stress, and consequently limit the types of conformational changes a molecule can make.^{11,12}

Devices have been developed to characterize these molecular bond properties. And other devices are available to study shear stress, viscosity and motility among biologic cells and subcellular structures. These tools include flow cytometry, atomic force microscopy, laser tweezers, cone plate viscometry, laser scalpels, laser scanning microscopy, and electron scanning probe microscopy. The first three are particularly useful for characterization of molecular bonds.

1.3. Plug Flow Cytometry

Flow cytometry uses a laser beam to count and differentiate among particles suspended in a fluid. Plug flow cytometry is an enhanced cytometry method that uses a bolus of particles to significantly increase the counting accuracy. The bolus is a precisely defined volume that is automatically injected at regular intervals into a particulate-free medium. The medium is continuously fed into a flow-cytometer for differential counting by size or to quantify the fluorescent intensity of reporter molecules.

Plug flow cytometry is accurate enough to show the ratios of particles involved in a given adhesive interaction (e.g. particle types A and B are mixed in suspension such that a particle pair A-B exists at a ratio $2A : B$). Thus the number of bond-pairings achievable between particles may be found in a way that is statistically robust.¹³ From the particle sizes, the surface areas of each particle involved in a given adhesive contact site might also be estimated. In this respect, plug flow cytometry

offers a way to quantitatively assess the effectiveness of a device usable with large particle populations to break interparticle molecular bonds. Knowing the device operating parameters under which a statistically significant quantity of particles are separated allows identification of the molecular bond rupture strength for that particle population at a given load rate.

1.4. Atomic Force Microscopy

Atomic force microscopy (AFM) is a scanning probe technique¹⁴ used to measure local atomic and molecular surface electrostatic forces to a resolution of 1×10^{-11} Newtons (or 10 pN), and to map surface topographies in three dimensions.¹¹ Through measurement of surface forces, force-extension curves are generated leading to insights into the stability, rotation, unfolding, unwinding, deformation and forces of individual molecules such as dextran (600 pN yield strength*) and single-stranded DNA (ssDNA, 480 pN rupture strength),¹⁵ and paired molecular interactions such as streptavidin/biotin (200 pN rupture strength),¹¹ P-selectin glycoprotein ligand/P-selectin (165 pN rupture strength at load rate $\approx 4 \times 10^4$ pN/sec)^{10,16} and ryanodine receptor 1 (RYR1, 42 to 73 pN rupture strengths at load rates 0.2 to 0.4×10^4 pN/sec).¹⁷ Such information is critical not only in understanding disease mechanisms, but also in developing drugs, where the effectiveness of a medication depends on the strength of a bond between a drug ligand and a cell receptor.

*Within this thesis, yield strength is defined as the point beyond which a molecule(s) is permanently deformed. Rupture strength is defined as the point at which the bond between two molecules breaks.

AFM has been used to map surfaces at the resolution of atoms, < 1 nm. Molecular sizes have been measured during molecule conformational changes, indirectly quantifying the level of specific enzyme (lysozyme) activity in biochemical reactions. Molecular binding and unbinding rates k_{on} and k_{off} have also been calculated using data from the force extension curves.^{10,17} And movements of the mechanochemical motor RNA polymerase on single stranded DNA have been observed.¹¹ The temporal resolution of these measurements at individual spatial locations are typically < 0.5 ms. Surface map scan times depend on the servo-motor speeds (40 to 100 nm/s).¹¹

1.5. Laser Tweezers

Laser tweezers, also known as optical tweezers or traps, are used in aqueous media to trap and manipulate small particles at forces up to 10^{-9} Newtons.^{15,18,19} When the laser source is a neodymium yttrium-aluminum-garnet (Nd:YAG) laser, the wavelength $\lambda = 1064$ nm, and there is minimal cellular damage from heating (< 2 °C) or ultraviolet radiation,^{15,20} making this device an excellent tool for work with biologic materials. Based on this wavelength, the diameter of the focal zone is typically 0.5 to 1 μm , so particles of size 10 nm to 100 μm may be captured.^{18,21,22}

With a laser, above the atomic scale there is momentum transfer between light photons and particles resulting in photon scattering and particle acceleration. The force associated with this acceleration is known as the scattered force component, F_{scat} . At the atomic scale, the momentum transfer is due to photon absorption by the individual atoms, followed by subsequent spontaneous photon emission and atom acceleration. F_{scat} is always directed along the laser beam path.

Another force exists, known as the dipole gradient force component F_{dipole} , which is a consequence of the electromagnetic properties of focussed light and the particles. This force is directed towards the laser focal region of the optic trap (pressure maxima) for particles with a high index of refraction, and towards pressure minima (away from the optic trap) for low index of refraction particles.^{18,20} At the atomic scale, the same process occurs but is better explained in terms of the laser frequency. If the laser is red-detuned (frequency lower than the atomic resonance) atoms will be pushed to the pressure maxima, and if the laser is blue-detuned (frequency higher than the atomic resonance), the atoms will be repelled to the pressure minima.²³ In acoustic radiation theory, a similar explanation of the radiation force in terms of resonance frequencies may be found for gas bubbles, but can also be applied for solid and liquid particles.

Applications fall into the categories of measurement of forces and motion, and positioning of particles.¹⁹ Of interest here are force and motion measurement capabilities. The spatial resolution dictated by the focal diameter of the laser tweezers does not prevent force measurement of particles < 10 nm. Following the Nobel-prize winning work of Chu and his associates, $1 \mu\text{m}$ diameter polystyrene beads can be coated with surface groups and attached to individual molecules such as DNA. The beads act as handles for manipulation and measurement of molecules.²⁴

Like AFM, force displacement curves have been made using laser tweezers. For example, it has been shown that bacteriophage λ -DNA will stretch to $16.5 \mu\text{m}$ at a force of 25 pN (a reversible conformational state change), and at 65 pN will overstretch to $20 \mu\text{m}$ (a non-reversible conformational state change).^{15,25,26} Chromatin fiber over-

stretch occurs at 20 pN, and the stretch modulus was measured at ≈ 5 pN.²⁷ Other measurements of myosin-actin interactions are reported in the range 1.8 to 10 pN^{15,28} with a stepping motion of 11 nm.¹⁸ The motility force of Spermatozoa has been measured at 40 to 45 pN and they can swim at up to 50 $\mu\text{m/s}$.^{15,20,29} Isometric forces generated by the mechanochemical enzyme kinesin was measured to be 1.9 ± 0.4 pN³⁰ with a stepping motion of 8 nm.¹⁸ And RNA polymerase motility has been measured at 14 pN.¹⁸ The shear modulus of red blood cell membranes has been reported to be 2.5 ± 0.4 $\mu\text{N/m}$ (micropipette aspiration yields results between 4 and 10 $\mu\text{N/m}$, and the accepted value is 6 $\mu\text{N/m}$).³¹ Bone and cartilage cell intracellular calcium levels have been studied after application of 7 pN forces using laser tweezers.³²

Laser tweezers are installed as part of microscope assemblies, and the laser light is guided using servo-controlled mirrors that determine the positioning resolution (< 200 ms), allowing < 10 nm step motion resolution of mechanochemical motors.^{14,20} The temporal resolution for particle capture within the laser tweezers is typically a few milliseconds.¹⁸

Force resolution depends on several factors. First, the particle size determines the form of the force equations describing the optic trap, as determined by Rayleigh scattering ($R \ll \lambda$), Mie scattering ($R \approx \lambda$) or geometric ray optic ($R \geq 10\lambda$) theories.³³ Second, the particle and medium dielectric properties and the laser power will determine the magnitude of the components of the radiation force, F_{scat} and F_{dipole} . Third, typically $F_{scat} \ll F_{dipole}$ so that $F \approx F_{dipole}$. A simplifying approximation is

often used of the form

$$F = PQn/c \quad (1)$$

where P is the laser power, n is the particle index of refraction, c is the light speed and Q is the trapping efficiency.^{15,19} Q is an unknown determined by calibrating the laser tweezers using one of two methods. The first method involves levitation of a particle of known properties, and performing a force balance of the radiation force against the buoyancy force.¹⁸ The second method involves catching particles of known properties within a well-defined flow stream, so that the radiation force may be balanced against a viscous drag force.³¹ Both of these techniques require finesse to use within microscopic assemblies, and may even be considered an art-form. Lasers are typically attenuated to a resolution of 0.1 mWatts. Using the viscous drag force as a means of calibration, force resolutions down to 0.1 to 0.6 pN/mWatt can be expected.^{29,31} Maximum laser powers of 1 Watt are typical, allowing a maximum force between 100 to 600 pN. Authors have reported maximum forces of $F_{scat} = 150$ to 500 pN and $F_{dipole} = 1000$ pN for the same laser power.¹⁵

It is clear there are discrepancies in the force capabilities of the laser tweezers, and that the protocols for calibration are not well-established enough. There is a broad range of measurements reported for the same molecular bonds, with up to 20% error in some of those measurements. Also, depending on the calibration method there are discrepancies in the maximum force capabilities reported for a 1 Watt laser tweezer unit.

1.6. Ultrasound

Atomic force microscopy and laser tweezers have spatial resolutions of 1 nm and $\approx 1 \mu\text{m}$ respectively, and temporal resolutions on the order of milliseconds, making them perfect devices for force-extension analysis of discrete particles and molecules. With maximum forces of 1000 pN and force resolution of 10 pN, AFM is best used with strong covalently bonded molecularly interactions, whereas laser tweezers can be used with most molecular interactions because of its force generation capabilities between 150 and 1000 pN (value dependent on experimental setup) and resolutions < 0.6 pN. In contrast, acoustic devices are a non-ionizing radiation so there will be no cellular damage from ultraviolet excitations (a possibility with laser tweezers). At operating frequencies of ≈ 500 kHz these devices support a temporal resolution on the order of μs and spatial resolution around 0.5 mm axially and 4 mm laterally. And the acoustic radiation forces can be developed up in the range fN to μN at resolutions of 0.1 pN.

For measurement of intercellular bond forces, ultrasound is capable of some of the force measurements performed by AFM and laser tweezers. First, using polystyrene beads ($> 2 \mu\text{m}$) as handles, similar to the methods employed with laser tweezers, the spatial resolution of ultrasound should not prevent separation of particles and subsequent estimation of interparticle adhesion forces.

Second, particle concentration and sorting can be performed using ultrasonic energy, and may be predicted from the radiation force equations. Columns of inorganic and organic particles (including biologic cells and DNA) have been formed based on their acoustic properties.³⁴⁻³⁸ Using the principle of particle column formation,

Flow chambers have been developed to concentrate and fractionate particulates from dilute suspensions.³⁹⁻⁴⁶ Other flow chambers have been developed specifically for sorting; rather than forming particle columns, flow streams of particles of known acoustic properties are generated allowing for accurate sorting.³⁹ Currently, particulate concentration techniques are being applied on a microscale.⁴⁷ If an acoustic device were developed similar to these chambers, the forces within the device can be determined for attached and unattached particles. Unlike the force equations used with laser tweezers, the force equations associated with acoustic radiation are well-defined and accurate. Complicated and error-prone calibration methods similar to those used in laser tweezers are not required.

Third, depending on the magnitude of forces on the particles and strength and number of molecular bonds, the forces required to break the bonds are achievable. Ultrasound spans the range of forces seen in laser tweezers and AFM: between 10^{-15} and 10^{-6} Newtons depending on the magnitude of the acoustic pressure field, particle size and particle and medium properties. Protein-protein interactions have been measured between 74 to 3300 pN rupture strengths, depending on the bond type, molecules involved, load rate, etc. so under the right conditions they may be broken.

There are some disadvantages to ultrasound methods. In some cases the forces required to break the molecular bonds between attached particles may be high, requiring high acoustic pressures. Such pressures are achievable, as witnessed by results of column formation experiments (see Table 1). And although the primary acoustic forces are well-defined, other forces are generated as a consequence of processes asso-

ciated with the acoustic radiation. Processes like acoustic streaming, cavitation, and secondary radiation forces cannot easily be separated from the primary radiation, and are not easily described.

From a temporal resolution standpoint, at an operating frequency of ≈ 500 kHz, time averaged radiation forces will affect particles within in $20 \mu\text{s}$. Force extension curves might possibly be generated if complementary ultrasonic or laser positioning methods are developed to measure interparticle distances on the scale of nms. Load rate adjustment to achieve a set of force-extension curves will require variance of the operating frequency of the device.

Another issue is the ability to observe discrete cellular events in an experiment. The wavelengths and focal diameter associated with laser tweezers ($\lambda \approx 1 \mu\text{m}$) allow individual cells to be manipulated, and the interparticle molecular bond forces measured by utilizing paired tweezer units on polystyrene beads attached to the molecules and calculating the net forces generated between these units. For ultrasound, although spatial resolution does not affect our ability to estimate interparticle molecular bond strengths, it does determine the quantity of particles that may be studied in our experimental setup. Acoustic radiation near 300 MHz is required to achieve a comparable spatial resolution to allow observation of discrete particles, and currently, only acoustic tweezers operating at 11 MHz have been developed to trap sub-micron particles.⁵² Use of GHz range transducers coupled to sapphire lenses has been proposed to make this achievable, but the negatives outweigh the advantages of current laser tweezer systems.

Table 1. Particle Levitation Examples

Particle	Diameter (μm)	Pressure (MPa)	Frequency (MHz)	Researcher
unencap. gas bubbles	$> 50 \mu\text{m}$	1.000	0.042	Crum ⁴⁸
alumina	3-12	0.700	0.073	Tolt ³⁷
polystyrene	9	0.400	3.120	Whitworth ⁴⁹
red blood cells	4	0.400	3.120	Whitworth ⁴⁹
red blood cells	4	0.162 and 0.246	0.300	Weiser ⁵⁰
red blood cells (in-vivo)	4	0.045	11.000	Harr ⁵¹
red blood cells (in-vivo)	4	0.175	3.000	Harr ⁵¹

Consequently, laser tweezers and AFM are appropriate for studying individual particle pairs at temporal resolutions of a few milliseconds, and acoustic fields are more appropriate for studying populations of particle pairs at temporal resolutions and load rates dependent on the device operating frequency.

If particle forces are identical within the population and can be individually isolated for study, optical methods and AFM can provide the required force information. However, it is likely that statistical variations in the forces exist, so that a study of cell mechanics would involve an ensemble of force mechanisms. Ultrasound, because of its spatial resolution, can make statistically significant and accurate force measurements for large sample populations, but is limited by its temporal resolution. When the task is to measure statistically molecular bond force strengths, acoustic methods and flow cytometry are appropriate tools.

1.7. Research Goals

The long term goal of this research is to develop tools that provide insight into the mechanics of biological cell interactions; specifically, to accurately measure molecular bond strengths at rupture. Measurement of the molecular bond rupture strength requires the use of acoustic radiation to break the bonds and a knowledge of the local forces and force gradients. One approach is to measure particle size distributions before and after subjecting them to acoustic fields of known strength, allowing determination of a threshold acoustic pressure above which a statistically significant number of molecular bonds are broken. By knowing the threshold pressure, the molecular bond force strength at rupture may be calculated. Another approach is to scale

chambers down to 10's of μl ,⁴⁷ where microscopic observation of particle interactions is feasible (a microsystems approach).

We focus on the first approach in this study. The short term goals, within the bounds of this thesis, will be to assemble a system to apply acoustic energy at approximately 500 kHz with duty factor ≥ 0.4 to particles with radii 1 to 50 μm . The first steps will be taken towards estimation of the molecular bond rupture strength between attached particles, by addressing the hypotheses listed below.

1.7.1. Hypotheses and Objectives

1. Our first objective is to design and build an ultrasonic device capable of particle column formation, and intend to demonstrate force generation in forming columns of gas-phase, solid particles and liquids. From the information learned, we will arrive at specifications of a chamber capable of manipulating red blood cells. The work of the first hypothesis is the last discussed in Sections 7 and 8.
2. We hypothesize that we will be able to accurately predict the pressure fields generated within the chamber. We wish to determine chamber design parameters which will allow particle column formation and will best match the chamber's acoustic pressure field to model predictions. We also wish to establish if the transducer crystal properties can be used to predict the pressure magnitudes in the field. The work of this hypothesis is discussed in Sections 4 and 5.
3. We hypothesize that using the acoustic radiation force equations and the pressure field we will be able to accurately predict the forces in the chamber, and

predict the locations of column formation. We wish to determine the parameters of the force equations which will allow us to make predictions for a wide variety of particles and acoustic pressures.

2. RADIATION FORCE: ANALYSIS AND REVIEW

Within this section, pressure and force equations valid for standing wave pressure fields will be reviewed and analyzed. As will be seen in later sections, the equations discussed here will prove essential to the development of models of the standing wave pressure field within the acoustic levitation chamber and forces on particles interacting with this field.

2.1. 1D Analysis of the Radiation Field

2.1.1. Pressure

Using the notation of the chamber geometry (see Figure 1), the general solution to the 1D homogeneous wave equation

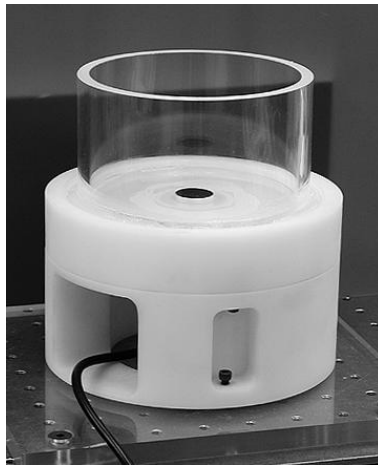
$$\frac{\partial^2 p(r', t)}{\partial r'^2} - \frac{1}{c^2} \frac{\partial^2 p(r', t)}{\partial t^2} = 0 \quad (2)$$

is

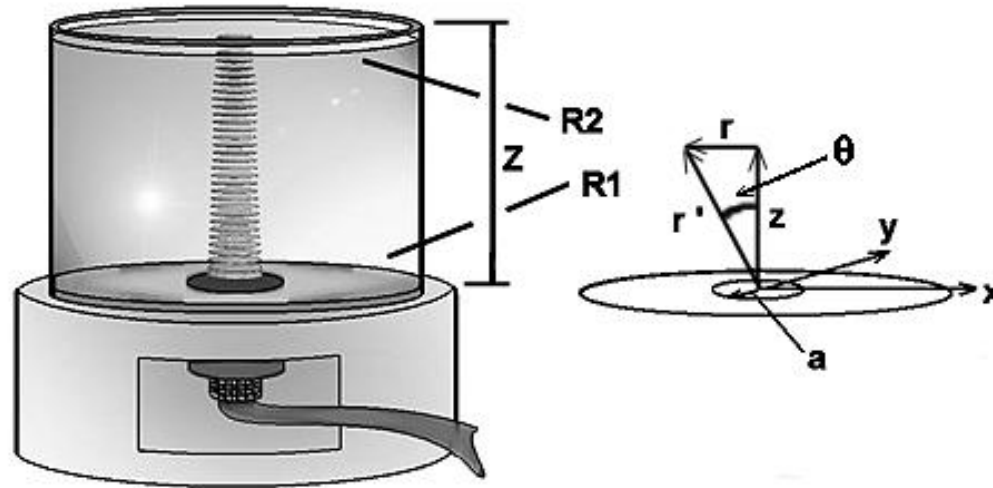
$$p(r', t) = p_1 (t - r'/c) + p_2 (t + r'/c) \quad (3)$$

for arbitrary pressures p_1 and p_2 , where c is the speed of sound in the medium (the magnitude of the longitudinal phase velocity). Standing waves will form between the base and water/air surfaces of the experimental chamber (see Figure 1) if p_1 and p_2 are longitudinal plane waves traveling along the z axis (viz. $r' = z$) in opposite directions. In that situation, the specific solution is

$$p(z, t) = \text{Re}\{P_1(z) \exp[i\omega(t - z/c)] + P_2(z) \exp[i\omega(t + z/c)]\}. \quad (4)$$



(a)



(b)

Figure 1. Above left (a) is the acoustic levitation chamber used for this research. Above center and right (b) is a schematic of the acoustic levitation chamber of height Z . A transducer of radius a is flush-mounted at the base, and the reflection coefficients at the base and water/air surfaces are designated $R1$ and $R2$. The standing wave field is illustrated by the column that extends from the base to the water/air surface. Above right is shown the geometry of the field assuming cylindrical symmetry.

Re is the real part of the complex quantity and ω is the angular temporal frequency. P_1 and P_2 take into consideration multiple reflections at the surfaces and are defined for lossy media as

$$P_1(z) = P \sum_{n=0}^{\infty} R_1^n R_2^n \exp \left[-\alpha_w (2nZ + z) \right], \quad (5)$$

$$P_2(z) = P \sum_{n=0}^{\infty} R_1^n R_2^{n+1} \exp \left[-\alpha_w (2(n+1)Z - z) \right], \quad (6)$$

where $-1 \leq R_1, R_2 \leq 1$ are reflection coefficients at the base and water/air surfaces, P is the source pressure amplitude, α_w is the attenuation coefficient of the medium, and n is an integer denoting the reflection number. The summations can only converge if R_1 and R_2 are not both unity, or if $\alpha_w > 0$.

The reflection coefficient of the water/air surface, R_2 , is approximately -1. However, R_1 of the water/plexiglas surface is 0.389 (Table 4 of Section 4). Using $\alpha_w = (3.733\mu\omega^2)/(2\rho c^3)$,⁴² at a temperature of 20° C, $\rho = 0.998$ g/cm³, $\mu = 0.010$ g/cm-s,⁵³ and $c = 1.483 \times 10^5$ cm/s,⁵⁴ we calculate $\alpha_w = 22.6 \times 10^{-5}$ Np/cm-MHz² or 19.6×10^{-4} dB/cm-MHz². So the wavenumber $k = \omega/c$ is essentially real, and wave propagation at 500 kHz in degassed water is essentially lossless if distortion is not present (see Section 3 for Oseen forces).

A simple situation in which standing waves are formed is found by setting Equation (4) to zero, $R_1 = 0$, $R_2 = -1$, and adjusting the water height to define a pressure node at Z , i.e. $p(Z, t) = 0$. Solving for z , there are other pressure nodes distributed in planes normal to the z axis and separated by half-wavelengths, viz., at $z = m\lambda/2$, where m is an integer. For this situation, Equation (4) reduces to the well known result⁵⁵

Plane Standing Wave Relative Pressure Model

$$\begin{aligned}
 p_s(z, t) &= \operatorname{Re}\left\{-iP_s \sin(kz) \exp(i\omega t)\right\} \\
 &= P_s \sin(kz) \sin(\omega t),
 \end{aligned} \tag{7}$$

where $P_s = 2P$ is the standing wave pressure amplitude, and the box is present to highlight its significance. Equation (7) describes the pressure in the ideal plane-wave experiment. However, in practice $|P_1| > |P_2|$ and $P_s < 2P$ due to propagational losses and beam divergence. If the water height is not exactly an integer multiple of $\lambda/2$, then $|p(Z, t)| > 0$ and a pressure gradient across the water/air surface will exist, giving rise to a force which will displace the water/air surface locally. If this displacement does not exceed limits imposed by surface tension, the water/air surface will shift until the condition $p(Z + \delta z, t) = 0$ exists (δz is an incremental shift in the water height) and the gradient across the surface is minimized. At 500 kHz, the maximum displacement of the water/air surface is $\lambda/2 \approx 1.5$ mm, which will be achievable at the chamber design pressures. To our pleasant surprise, this effect was observed. Careful adjustment of the water height to obtain standing waves was expected, but instead it was found standing waves occurred regardless of the water height.

2.1.2. Forces

Particles within a standing wave pressure field experience a radiation force that varies along the direction of sound wave propagation. This primary radiation force is a vector (boldface) defined as⁵⁶

$$\mathbf{F}_p = \left\langle \int_{S_o} (\mathbf{\Pi}_{ij} - \rho v_i v_j) dS_j \right\rangle = - \int_{S_r} \langle \mathbf{\Pi}_{ij} \rangle dS_j, \quad (8)$$

where $\langle \cdot \rangle$ denotes time-averaging, $\mathbf{\Pi}_{ij}$ is the acoustic radiation stress tensor, i and j indicate the axial and lateral direction components, ρ and v are the fluid medium density and particle velocity magnitude, S_o is the surface of the particle at time t and S_r is a surface far from but bounding the particle. For an Eulerian fluid,[†] the stress tensor is given by⁵⁷

$$\mathbf{\Pi}_{ij} = p\delta_{ij} + \rho v_i v_j \quad (9)$$

where the Kronecker delta δ_{ij} is unity for $i = j$ and zero otherwise.^{58(ch.2, p.60)} The pressure p may be described in terms of the fluid medium particle velocity potential ϕ and magnitude $v = |\nabla(\phi)|$ ⁵⁶ as follows:

$$p = -\rho \frac{\partial \phi}{\partial t} - \rho \frac{v^2}{2} + \frac{\rho}{2c^2} \left(\frac{\partial \phi}{\partial t} \right)^2. \quad (10)$$

[†]In the Eulerian description of fluid flow, individual fluid particles are not identified, as is the case for the Lagrangian description. Instead, a control volume is defined, such that pressure, velocity, acceleration, and all other flow properties are described as fields within the control volume. Since fluid flow is a continuum phenomenon the Eulerian description is preferable in fluid mechanics.

Combining Equations (8), (9) and (10), and noting $\langle \rho \partial \phi / \partial t \rangle = 0$, the acoustic radiation force is written as

$$\mathbf{F}_{\mathbf{p}} = \int_{S_r} \left\{ \left[\frac{\rho \langle v^2 \rangle}{2} - \frac{\rho}{2c^2} \left\langle \left(\frac{\partial \phi}{\partial t} \right)^2 \right\rangle \right] \delta_{ij} - \rho \langle v_i v_j \rangle \right\} dS_j. \quad (11)$$

Several authors have solved Equation (11) for the ideal standing wave pressure field described by Equation (7).⁵⁹⁻⁶¹ First, the traveling wave velocity potential ϕ (and therefore v) in Equation (11) is rewritten as the sum of incident (ϕ_{inc}), scattered (ϕ_{scat}) and particle (ϕ_o) velocity potentials in spherical coordinates:

$$\phi = \phi_{inc} + \phi_{scat} + \phi_o. \quad (12)$$

Applying the boundary conditions implicit at the particle surface we can solve for ϕ and v :

$$\begin{aligned} \frac{\partial \phi}{\partial r} \Big|_{r=a} &= \frac{\partial \phi_o}{\partial r} \Big|_{r=a} \\ \rho \phi(a) &= \rho_o \phi_o(a) \\ \rho \frac{\partial \phi}{\partial \theta} \Big|_{r=a} &= \rho \frac{\partial \phi_o}{\partial \theta} \Big|_{r=a}. \end{aligned} \quad (13)$$

Equation (11) for traveling wave pressure fields may then be solved. For standing wave pressure fields, a spatial dependence term

$$\xi_n = (-1)^n \exp(ikz) + \exp(-ikz) \quad (14)$$

is introduced, which in the case of $n = \text{even}$ leads to $\xi_n = 2 \cos(kz)$ and $n = \text{odd}$ leads to $\xi_n = -i2 \sin(kz)$. Physically, $2 \cos kz$ will occur if the reflector is a rigid pressure boundary such as a solid plate (i.e. $R_2 = 1$), and $-i2 \sin kz$ occurs for a pressure

relief boundary such as the water/air surface (i.e. $R_2 = -1$ as is the case for the current chamber design). Hence, the primary radiation force is directed along the z axis:

Plane Standing Wave Force Model

$$\mathbf{F}_p = -\pi R_o^3 \frac{P_s^2}{\rho c^2} X k \sin(2kz) \hat{\mathbf{e}}_z, \quad (15)$$

where $\hat{\mathbf{e}}_z$ is a unit vector (see Figure 1) and X includes properties of the particle and medium. In the small-wavelength limit, $k_o R_o \ll 1$ and $k R_o \ll 1$, for particles in a gas-phase,

$$X = - \left[\frac{(c/c_o)^2 (3\rho_o/\rho - (k_o R_o)^2)}{(c_o/c)^2 (k_o R_o)^6 + (3\rho_o/\rho - (k_o R_o)^2)^2} \right], \quad (16)$$

and for solid or liquid particles,

$$X = \left[\frac{\rho_o/\rho + \frac{2}{3}(\rho_o/\rho - 1)}{1 + 2\rho_o/\rho} \right] - \left[\frac{1}{3(\rho_o/\rho)(c_o/c)^2} \right], \quad (17)$$

where R_o is the particle diameter, ρ_o is the particle density, c_o is the speed of sound in the particle, and k_o is the particle wavenumber. Equations (15), (16), and (17) describe the primary radiation force if ρ/ρ_o is of order one for solid or liquid particles, of order $(kR_o)^2$ for gas-phase particles, and thermal and viscous effects are negligible. It is assumed that the particles are spherical, and much smaller than the wavelength of sound, specifically $k_o R_o \ll 1$ and $k R_o \ll 1$. For $kR_o < 0.1$ at 500 kHz, "small" may be defined as any particle less than 0.1 mm in diameter.

When particle acoustic properties are such that $X < 0$, as for small diameter gas-phase particles, the primary radiation force will be directed towards pressure

antinodes (Figure 2). When $X > 0$, as is the case for most small diameter solid and liquid particles, the force is directed towards pressure nodes.

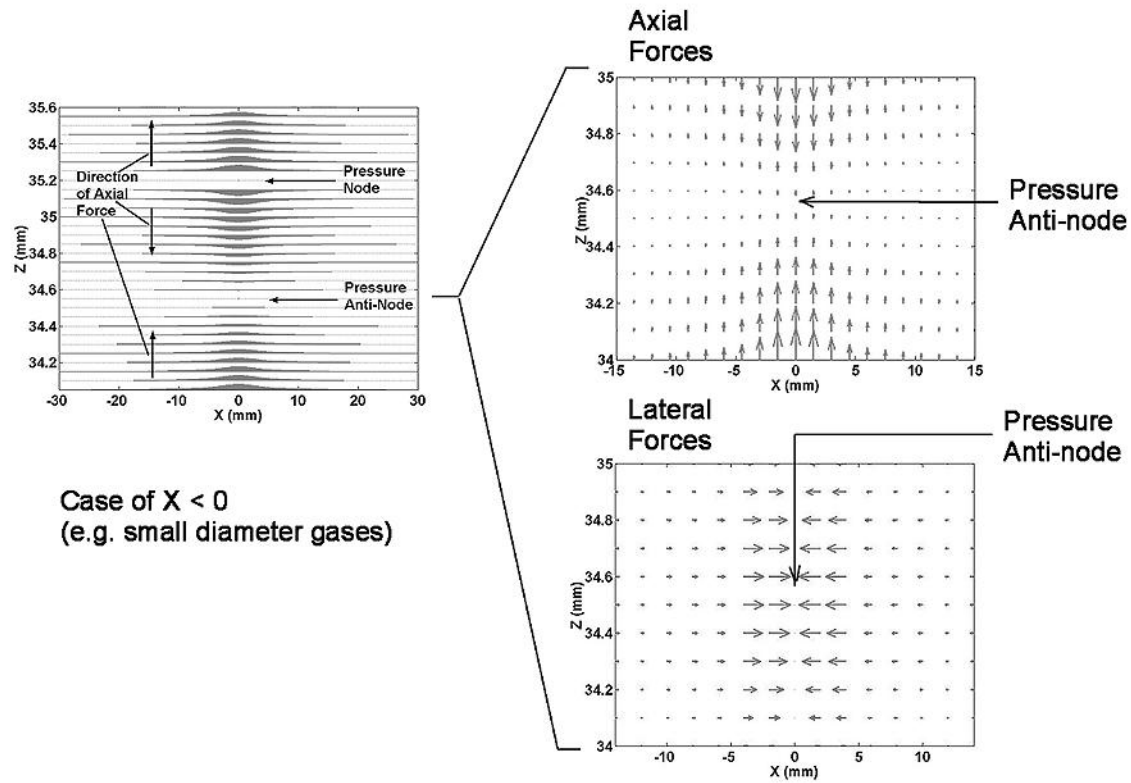
Using $\partial \langle p^2(z, t) \rangle / \partial z = P_s^2 k \sin(2kz)/2$, Equation (15) can also be rewritten in the form

$$\mathbf{F}_p = -2\pi R_o^3 \frac{1}{\rho c^2} X \frac{\partial}{\partial z} \langle p^2(z, t) \rangle \hat{\mathbf{e}}_z \quad (18)$$

Physically, these equations show that within a standing wave pressure field, particles experience a radiation force which is proportional to the gradient of the time-averaged acoustic field intensity, the particle volume, and particle and medium acoustic properties. This force can be controlled to counteract other particle forces such as buoyancy, thus allowing capture of the particles at pressure nodes or antinodes within the field. This force might also be used to offset and thus study other interparticle forces.

In the case where radiation, thermal and viscous damping effects are not negligible, Crum and Prosperetti⁶² have developed variations of this equation for gas bubbles. Doinikov⁶³⁻⁶⁶ has also provided solutions for gas bubbles and solid/liquid particles in planar and spherical waves where viscous terms are not negligible. We would also refer the reader to a paper by Asaki and Marston,⁶⁷ which offers a review of some of the various forms of the primary radiation force equation available in the literature.

Following a derivation by Prosperetti,^{68,69} a simpler equation for the primary radiation force for a gas bubble can be derived. As before, for an Eulerian fluid, combining the radiation stress tensor⁵⁷ of Equation (9) with the general form of the



Case of $X < 0$
(e.g. small diameter gases)

Figure 2. Shown above are the relative axial and lateral components of the primary radiation force for particles centered around a pressure antinode region. The net force experienced by the particles is primarily the sum of the radiation and particle buoyant forces. Particle column formation will occur at positions in the standing wave pressure field where the net force is zero.

primary radiation force,⁵⁶ Equation (8), we obtain

$$\mathbf{F}_p = - \int_{S_r} \langle p\delta_{ij} + \rho v_i v_j \rangle dS_j. \quad (19)$$

For a spherical bubble the second term in the integral is zero. Pressure p has both an incident and a scattered component,

$$p = p_{inc} + p_{scat}. \quad (20)$$

For the case $k_o R_o \ll 1$ and $1/\rho_o c_o^2 \gg 1/\rho c^2$, i.e. small compressible bubbles, $p_{inc} \gg p_{scat}$. Expanding $p = p_{inc}$ as a Taylor series, we find

$$p = p(z_o, t) + (z - z_o)\nabla p(z, t) + \text{higher order terms}. \quad (21)$$

$p(z_o, t)$ is a constant, ∇ is the gradient operator, and the higher order terms are negligible since they involve powers of $k_o R_o \ll 1$. Hence, Equation (19) reduces to

$$\mathbf{F}_p = - \langle V(t)\nabla p(t) \rangle. \quad (22)$$

This solution presumes the contribution of the scattered pressure field is negligible, whereas the derivation of Equation (15) makes no such assumption.

Following a method similar to that introduced by Eller⁵⁵ for a gas-phase particle, the pressure $p(z, t)$ is defined by Equation (7), and

$$V(t) = V_o (1 + \gamma \sin(\omega t)) \quad (23)$$

where V_o is the particle volume prior to insonication. The instantaneous particle volume can be described in terms of the local pressure ratio between the medium and the particle. Since the particle compressibility $1/\rho_o c_o^2$ has units of Pa^{-1} , we can define

$$\gamma = -P_s \frac{\sin(kz)}{\rho_o c_o^2}. \quad (24)$$

Using Equations (7), (22), (23), and (24), we find

$$F_{pz} = -\pi R_o^3 \frac{P_s^2}{\rho c^2} k \sin(2kz) \left[\frac{-1}{3(\rho_o/\rho)(c_o/c)^2} \right]. \quad (25)$$

This equation is a special case of Equation (15). The expression in the right-hand brackets is X of Equation (17) when the condition $\rho \gg \rho_o$ is applied. It is a valid approximation for small spherical gas-phase particles where $k_o R_o \ll 1$, $k R_o \ll 1$, ρ/ρ_o is of the order $(k R_o)^2$ and thermal and viscous effects are negligible. Under these conditions $1/\rho_o c_o^2 \gg 1/\rho c^2$ so that $p_{inc} \gg p_{scat}$, and the monopole contributions to the primary radiation force dominate over the dipole contributions. This solution does not take into consideration the dependence of γ on the particle size R_o , so it cannot be expected that this solution will be in full agreement with the X for gas-phase particles defined by Equation (16), which takes into account the affect of particle size on the monopole and dipole terms.

Particles also experience other forces including buoyancy, Brownian motion, acoustic streaming, viscous drag, and a force arising from the gradient of the hydrostatic pressure. For the current experimental situation, the buoyant force is the largest (refer to Section 3 for an order-of-magnitude analysis):

$$\mathbf{F}_b = \frac{4}{3}\pi R_o^3 (\rho - \rho_o) g \hat{\mathbf{e}}_z \quad (26)$$

where g is the gravitational acceleration.

Particles are at equilibrium in the pressure field when the net force acting on them is zero. Equating Equation (15) with Equation (26), we solve for P_s at positions

$z = (2m + 1)\lambda/8$ where the acoustic force is maximized:

$$P_{mtp} = P_s \Big|_{equil.} = \left| \left(\frac{4g\rho(\rho - \rho_o)c^3}{3X\omega} \right)^{\frac{1}{2}} \right|. \quad (27)$$

P_{mtp} is the minimum trap pressure in the standing wave field required to hold a particle in an equilibrium position. Achieving this amplitude is the goal of particle levitation.⁴⁸

2.2. 2D Analysis of the Radiation Field

2.2.1. Pressure

Thus far a 1D analysis of the standing wave pressure field has been considered. Using plane-piston theory^{58(ch.7, pp.175-189)}, which assumes no attenuation and lateral symmetry, a more accurate 2D solution has been postulated to allow for pressure variations in both the axial and lateral directions. Given $r'^2 = z^2 + r^2$ (Figure 1), the traveling wave from a plane piston radiator in the far field is given by

$$p(z, r, t) = Re \left\{ P \exp [i\omega (t - r'/c)] \left[\frac{2J_1(kar/r')}{kar} \right] \right\}. \quad (28)$$

Combining Equations (4), (5), (6) and (28), the corresponding 2D standing wave equation is

Beam Standing Wave Relative Pressure Model

$$\begin{aligned}
 p_s(z, r, t) = & \operatorname{Re} \left\{ \left(P \sum_{n=0}^{\infty} R_1^n R_2^n \exp [i\omega (t - r'_n/c)] \left[\frac{2J_1(kar/r'_n)}{kar} \right] \right. \right. \\
 & \times \exp [-\alpha_w (2nZ + z)] \\
 & + \left. \left(P \sum_{n=0}^{\infty} R_1^n R_2^{n+1} \exp [i\omega (t + s'_n/c)] \left[\frac{2J_1(kar/s'_n)}{kar} \right] \right. \right. \\
 & \left. \left. \times \exp [-\alpha_w (2(n+1)Z - z)] \right) \right\}, \tag{29}
 \end{aligned}$$

where $r_n'^2 = (2nZ + z)^2 + r^2$, $s_n'^2 = (2(n+1)Z - z)^2 + r^2$, and a is the source aperture radius. This equation is the heart of the pressure model discussed in Section 5.

2.2.2. Forces

Using the same method as the one dimensional derivations,⁵⁹⁻⁶¹ the plane piston pressure field equation has also been expressed in terms of a velocity potential and solved for the acoustic radiation force for traveling wave pressure fields.^{70,71} However, to our knowledge, the derivation has not been extended for standing waves. Such a derivation would have to include a non-trivial lateral spatial dependence term that takes into account spherical divergence and multiple reflections, and it can be expected the final solution will be quite complex in form.

Analyzing each lateral position in the 2D field topography independently, in the axial direction Equations (15) through (18) from the 1D analysis may be a valid approximation despite phase variations between a plane and beam standing wave pressure fields. As will later be seen in Section 6, deviations between results from

force equations derived for each pressure field type are less than 1%.

For the lateral direction an equation similar in form to Equation (18) may be derived. It has been suggested by Hertz⁵² for solid and liquid particles in a pressure field of the form

$$\begin{aligned} p(z, r, t) &= P_s(z, r) \sin(\omega t) \\ &= P_s(z) \left[\frac{2J_1(Cr)}{Cr} \right] \sin(\omega t) \end{aligned} \quad (30)$$

that in analogy to the axial solution of the primary radiation force, in the lateral direction the primary radiation force may be written as

$$F_{pr} = -\pi R_o^3 \frac{P_s^2(z)}{\rho c^2} X \frac{\partial}{\partial r} \left[\frac{2J_1(Cr)}{Cr} \right]^2. \quad (31)$$

Using our terminology, Hertz's solution may be rewritten as

$$F_{pr} = -2\pi R_o^3 \frac{1}{\rho c^2} X \frac{\partial}{\partial r} \langle p^2(z, r, t) \rangle. \quad (32)$$

Comparing Equations (18) and (32), the acoustic radiation force in two dimensions is

Beam Force Model

$$\mathbf{F}_p = -2\pi R_o^3 \frac{1}{\rho c^2} X \nabla (\langle p^2(z, r, t) \rangle). \quad (33)$$

As shall be seen, Equation (33) using X as defined in Equations (16) and (17), is the essential equation used to predict the radiation force in the force model of Section 6.

Gor'kov⁷² also derived a solution for the radiation force which holds for solid and liquid particles in any arbitrary pressure field other than a plane traveling wave field.

He defined the primary radiation force in terms of a field potential U :

$$\mathbf{F}_p = -\nabla U \quad (34)$$

The field potential U is

$$U = V_o \left[\frac{\langle p^2(z, r, t) \rangle}{2\rho c^2} f_1 - \frac{3\rho \langle v^2(z, r, t) \rangle}{4} f_2 \right] \quad (35)$$

where f_1 , f_2 are the monopole and dipole contributions of the particle, defined by

$$f_1 = 1 - \frac{\rho c^2}{\rho_o c_o^2} \quad (36)$$

and

$$f_2 = \frac{2(\rho_o - \rho)}{2\rho_o + \rho}. \quad (37)$$

v is the fluid medium particle velocity and is related to the entrained particle velocity by

$$\mathbf{v} = \frac{2\rho_o + \rho}{3\rho} \mathbf{u}. \quad (38)$$

The time-averaged potential energy and kinetic energy densities are defined as^{36,45,46,49}

$$\langle \text{PE} \rangle = \frac{\langle p^2(z, r, t) \rangle}{2\rho c^2} \quad (39)$$

and

$$\langle \text{KE} \rangle = \frac{\rho \langle v^2(z, r, t) \rangle}{2}. \quad (40)$$

Hence Equation (35) may be rewritten as

$$U = V_o \left[\langle \text{PE} \rangle f_1 - \frac{3 \langle \text{KE} \rangle}{2} f_2 \right]. \quad (41)$$

For small oscillating particles in a lossless medium, $\langle \text{PE} \rangle = - \langle \text{KE} \rangle$ so that

$$U = V_o \langle \text{PE} \rangle \left[f_1 + \frac{3}{2} f_2 \right]. \quad (42)$$

For solid and liquid particles, a comparison of Equations (34) and (42) with Equations (15) and (17) shows $X = f_1/3 + f_2/2$. Gor'kov's solution may also be extended for gas-phase particles. Comparing Equations (34) and (42) with Equations (15) and (16) shows $3X = f_1 - 1$ under the assumption of $k_o R_o \ll 1$. For $f_1 \gg 1$ then $X = f_1/3$, and when $f_1 \gg f_2$ Equation (42) becomes

$$U = 3V_o < \text{PE} > X. \quad (43)$$

When the potential energy density definition^{36,46,49} is applied, Equations (34) and (42) are identical to Equation (33), which is the heart of the force model of Section 6. These equations are valid for small spherical particles where $k_o R_o \ll 1$, $k R_o \ll 1$ and thermal and viscous effects are negligible. For solid and liquid particles ρ/ρ_o is of the order one. For gas-phase particles ρ/ρ_o is of the order $(k R_o)^2$, and the monopole contributions to the primary radiation force dominate over the dipole contributions ($f_1 \gg 1$, $f_1 \gg f_2$).

In two dimensions, the buoyant force is still described by Equation (26), since it is only dependent on the particle and medium properties and may be considered a constant throughout the chamber, except near the water/air surface where the particle may be incompletely enveloped by the medium. Also, since the form of the acoustic radiation force equation has remained unchanged in the axial direction, P_{mtp} may still be described by Equation (27).

In a 2D analysis populations of particles are levitated, and columns will form due to the primary radiation force. For a lateral pressure beam profile, P_{mtp} is seen to occur at the margins of the sound beam. So along the axial centerline the pressure

may be described by

$$P_{center} = P_{mtp} \times 10^{-(W/20)} \quad (44)$$

where $W \leq 0$ dB is the pressure drop-off at the margins of the sound beam referenced to the axial centerline, and is related physically to the edge-to-edge lateral width of the particle columns. The edges of the column formation will be located where the primary radiation force is maximized, $\lambda/8$ from the pressure nodes or antinodes. Depending on the direction of the buoyant force, there will be a curvature to the particle columns up or down, corresponding to the lateral pressure beam profile (see Figure 3). Column curvature occurs along those pressure contour lines which are equal to the minimum trap pressure.

The region of column formation may be thought of as a “trapping zone”. While particles remain in this region they will be trapped and levitated. However, the lateral pressure beam profile also gives rise to a lateral component of the primary radiation force, which over time acts to push particles towards pressure minima ($X > 0$) or maxima ($X < 0$). In a 2D analysis, the pressure antinodes and nodes are located in the same axial positions as in the 1D analysis. However, laterally the pressure antinodes are still located at the axial centerline but the pressure nodes are located at locations of absolute minimum pressure (i.e. the chamber walls).

Columns of particles for $X < 0$ (small gas bubbles) will form at the pressure antinodes along the axial centerline, as in the 1D case. Because the lateral force is an order of magnitude smaller than the axial primary radiation force (see Sections 3 and 6), columns of particles with $X > 0$ (e.g. many solid and liquid particles)

will in the short term form at pressure minima along the axial centerline, but will eventually dissipate. Over time these particles will be pushed from the axial centerline towards the pressure minima in the chamber. For the current chamber geometry, particle concentrations at the pressure minima never actually occur because the lateral radiation force weakens considerably away from the axial centerline and is dominated by other forces present in the chamber.

2.3. Prediction of Medium Pressure from Piston Radiators

It is convenient to have an expression that relates experimentally controlled parameters, e.g. voltage, to essential physical parameters, e.g. pressure. The following section relates these two qualities.

For a given source aperture the pressure in the medium at the crystal surface, T , can be related to the transducer crystal field strength E :⁷³

$$\begin{aligned} T &= E\sqrt{2M_o} \\ &= \frac{V}{t_c}\sqrt{2M_o}, \end{aligned} \tag{45}$$

where V is the RMS transducer drive voltage and t_c is the transducer crystal thickness. $M_o = (d_{33}/SE_{33})^2$ is the crystal material figure of merit that describes the amount of transducer surface movement, d_{33} is the piezoelectric coefficient and SE_{33} is the elastic compliance.

The pressure T can be related to the displacement of the medium at the crystal surface U_o by^{58(ch.5, p.127-130)}

$$U_o = \frac{T}{\rho c}. \tag{46}$$

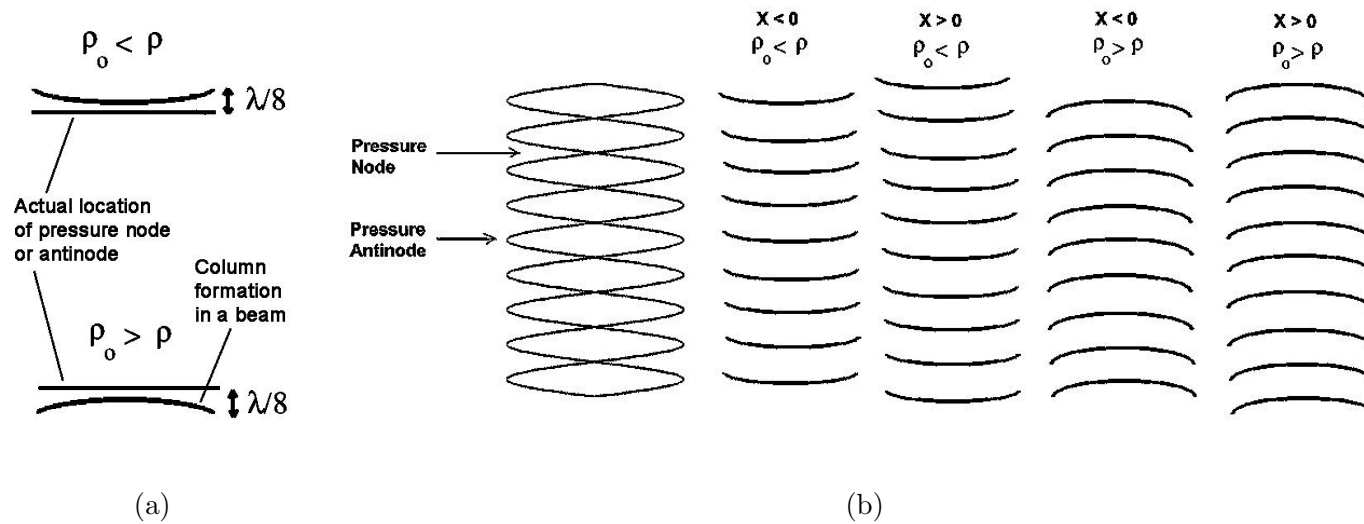


Figure 3. (a) The shape of column formation is dictated by the relationship between the density of the particle and the medium and the topography of the pressure field. (b) Location of column formation near the pressure nodes or antinodes is dictated by the value of X .

By summing the contributions of individual sub-areas dS over the surface area of an unbaffled circular plane piston (i.e. a transducer with a low impedance backing layer), we obtain the field pressure amplitude along the axial centerline,

$$P_{center}(z) = \left| 2\rho c U_o \sin \left[\frac{1}{2} k z \left(\sqrt{1 + (a/z)^2} - 1 \right) \right] \right|. \quad (47)$$

Combining Equations (45), (46) and (47) we can relate the transducer drive voltage to the traveling wave pressure field amplitude along the axial centerline:

Beam Absolute Pressure Amplitude

$$P_{center}(z) = \left| \frac{V}{t_c} \sqrt{2M_o} \sin \left[\frac{1}{2} k z \left(\sqrt{1 + (a/z)^2} - 1 \right) \right] \right|. \quad (48)$$

Combining Equation (44) with (48) we obtain:

$$W = -20 \log \left| \frac{V}{t_c P_{mtp}} \sqrt{2M_o} \sin \left[\frac{1}{2} k z \left(\sqrt{1 + (a/z)^2} - 1 \right) \right] \right|. \quad (49)$$

$P(z)$ is a maximum at the near field/far field transition region, near a^2/λ , so we find W and the column width will be a maximum in this region. Equation (49) shows that W and the particle column widths may be controlled through variation of the transducer drive voltage. The physical column width will depend on the axial location, the transducer crystal properties, aperture size, operating frequency, the particle and medium properties, and the particle size.

Equation (29) is essential to the pressure model of Section 5 because it describes the field topography, but cannot quantify the pressure magnitudes because the magnitude of P is unknown. Equation (48) provides the means to quantify the pressure

magnitude at any point in the field topography, and links the transducer properties to that pressure field. These two equations, together with Equation (33), will allow the prediction of particle forces and the locations and widths of particle columns within the chamber.

3. ORDER-OF-MAGNITUDE ANALYSIS OF FORCES

Within this section, we look more closely at the assumption of viscous and thermal dissipation, and other forces present. At the end of this section, a summary of forces is found in Table 2.

3.1. Viscous and Thermal Dissipation

The primary radiation force, Equation (33), is valid under the assumption that viscous and thermal dissipation are negligible.

At 500 kHz, the particle viscous boundary layer $\delta_v = \sqrt{2\mu/\omega\rho}$ is 6.390 nm at 20 °C. For all particle sizes considered in this research, viscous damping effects are negligible since $R_o \gg \delta_v$.^{42,45,74}

If particle motion is not a reversible process, there will also be temperature gradients and a thermal penetration layer will envelope the particle. The layer thickness $\delta_t = \sqrt{2\chi/\omega}$ is typically 0.100 μm , where χ the thermal diffusivity constant. For $R_o \gg \delta_t$ (i.e. $R_o > 1 \mu\text{m}$), losses due to thermal damping are negligible.³⁶

The above analysis is valid for spherical particles consisting of a single phase. However, biologic cells are of mixed (liquid and solid) phase, so that viscous dissipation occurs not only at the interface between the particle and the medium but also within the cell interior. The current research does not address this issue.

3.2. Secondary Radiation Forces

The primary radiation forces arise from particle interaction with the standing wave pressure field. There are also secondary radiation forces generated between particles

from their scattered pressure fields. These forces are also known as Bernoulli or Koenig forces.⁴⁵

Using derivations of the secondary radiation force between gas bubbles⁷⁵ and rigid spheres,⁵¹ the magnitude of the secondary radiation force between particles of similar size and acoustic properties is^{42,50}

$$\mathbf{F}_s = 4\pi R_o^6 \left[\frac{(\rho_o - \rho)^2 (3\cos^2 \theta - 1)}{6\rho d^4} \langle v^2(z, r, t) \rangle - \frac{\omega^2 \rho (1/\rho_o c_o^2 - 1/\rho c^2)^2}{9d^2} \langle p^2(z, r, t) \rangle \right] \hat{\mathbf{e}}_\theta \quad (50)$$

where θ is the angle between the centerline of the two particles and the direction of acoustic wave propagation, d is the interparticle distance, and $\hat{\mathbf{e}}_\theta$ is a unit vector from particle 1 to particle 2, where particle 1 is the radiator and particle 2 experiences the secondary radiation force. Negative values of \mathbf{F}_s represent an attractive force on particle 2, and positive values represent a repulsive force on particle 2. The geometry associated with the secondary radiation forces is shown in Figure 4.

The first term in brackets in Equation (50) is the dipole contribution dependent on the particles' orientation, and vanishes at the pressure antinodes (which are also velocity nodes). The second term in brackets is the monopole contribution independent of the particle orientation, and vanishes at the pressure nodes. The primary radiation force pushes and aligns solid and liquid particles in a lateral plane within $\lambda/8$ from the pressure nodes. At this location, the dipole contribution dominates over the monopole contribution, and for $\theta = 90^\circ$ the force is attractive because it is negative. For $\theta = 0^\circ$ the force depends on the interparticle distance: for small distances it is repulsive and for larger distances it is attractive. For gas-phase particles aligned in a

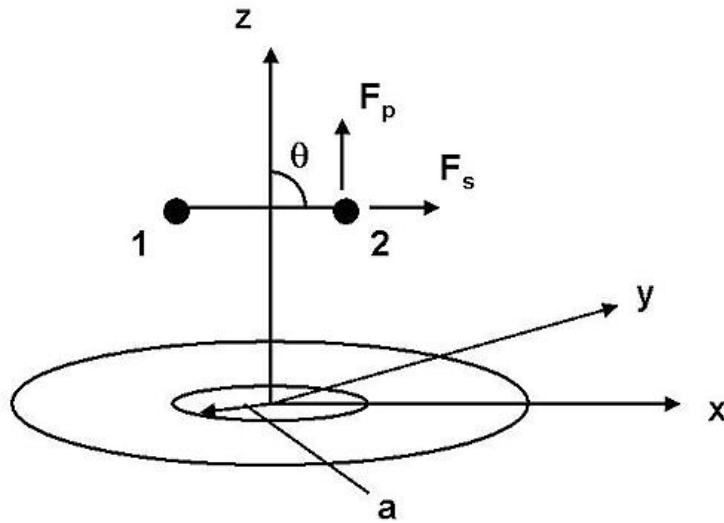


Figure 4. Above is shown the geometry between two particles in a cylindrically axisymmetric pressure field generated by a plane piston radiator of radius a . Particle 2 experiences a primary radiation force F_p from this pressure field, and a secondary radiation force F_s due to the scattered radiation pressure field of particle 1.

plane within $\lambda/8$ from the pressure antinodes, the monopole contribution dominates over the dipole contribution, and the force is attractive for all θ and interparticle distances. Thus the secondary radiation force helps to minimize the effects of the lateral component of the primary radiation force, and aids in particle alignment and aggregation within columns at the pressure nodes and antinodes.⁴²

Near to the pressure nodes, for highly dispersed solid or liquid particles of diameter $5 \mu\text{m}$ and interparticle distance $d = 100 \mu\text{m}$, the secondary radiation force will be $\approx 10^{-10}$ smaller than the axial component of the primary radiation force. Where particle aggregation occurs, it can be assumed particles are touching so that $d = 5 \mu\text{m}$ and under these conditions the secondary radiation force will be $\approx 10^{-5}$ smaller than the axial component of the primary radiation force.

Near to the pressure antinodes, for highly dispersed gas particles of diameter 5

μm and interparticle distance $d = 100 \mu\text{m}$, the secondary radiation force is on the same order as the axial component of the primary radiation force. Where particle aggregation occurs, it can be assumed $d = 5 \mu\text{m}$ and under these conditions the secondary radiation force will be $\approx 10^3$ larger than the axial component of the primary radiation force. In later levitation experiments (Section 7), it was witnessed that the gas-phase particle pairs sometimes performed rhythmic lateral motions that were probably due to the secondary radiation force. This “dancing” did not interfere with column formation, but did introduce blurring of individual particles during photography, noticeable as white streaks.

The secondary radiation forces are important because they will dictate interparticle spacing in the pressure field, and can represent a significant contribution to the force model in all areas of the pressure field. For solid and liquid particles, at the regions of column formation the secondary radiation forces will have little effect on the geometry of the particle columns and the force model predictions are not affected. For gas-phase particles, at the regions of column formation the secondary radiation forces will affect the geometry of the particle columns and the force predictions. Strong particle aggregation can be expected because the force is attractive for gas-phase particles in this region. In other regions of the pressure field the secondary radiation forces may influence force model predictions.

At this stage secondary radiation forces will not be introduced into the force model. The secondary radiation forces may cause secondary particle aggregations within the columns, and are not of material interest in the current research (except

to say that secondary aggregates may form). The long term goal of this research will be to predict forces associated with biologic cells at all regions of the pressure field, but for solid and liquid particles these forces are small compared to the axial component of the primary radiation force.

3.3. Acoustic Streaming

Acoustic streaming may be divided into large-scale displacement and small-scale displacement types. Small-scale acoustic streaming has been further classified as Schlichting (displacements $\ll \lambda$) and Rayleigh (displacements on the order of λ) streaming. At this time, not much is known or understood about small-scale streaming effects; they are under current investigation by other authors.⁷⁶ Large-scale streaming is known as Quartz wind or Eckart streaming and is due to absorption of acoustic energy in the bulk medium. For spherical particles $< 50 \mu\text{m}$ radius in a water medium, streaming velocities up to 2 cm/s have been experienced for Reynold's number < 1 (i.e. within the Stoke's flow region).

These velocities are unacceptable within the current experimental design. Since Quartz wind is a bulk medium process, it can be minimized if the acoustic pressure field does not have a net traveling wave component (i.e. the pressure field is a perfect standing wave).⁴⁹ Unfortunately, the standing wave pressure field is not ideal due to beam divergence, attenuation, etc.

It has been shown that the speed of acoustically driven bulk streaming is directly proportional to the fluid medium particle mean free path length (for the current design, the chamber water height).⁷⁶ Hence, use of acoustically transparent films

(ATFs) and/or low-attenuation phantoms may substantially reduce the streaming effects. In either case care must be taken to minimally disturb the sound field, so that the ATF thickness $\ll \lambda$ and/or phantom attenuation is small. Also the acoustic impedances of the ATF and phantoms should match the acoustic impedance of the fluid medium. Experimentally, low-attenuation agar cylinders were used effectively to minimize streaming effects present in the chamber (see Section 4).

3.4. Thermal Convection

In addition to acoustic streaming, absorption of acoustic energy in the bulk medium can lead to heating and thermal convection. In this case, temperature gradients will be manifested in the fluid medium as local variations in viscosity, so that the viscous drag forces will be affected. For the current experimental design, by measurement of the medium temperature at various locations within the chamber, no significant temperature gradients were found during operation of the transducers.

3.5. Viscous Drag Forces

Within the region of viscid flow known as the Stoke's region, neglecting particle inertia, the viscous drag force on the particles is

$$\mathbf{F}_d = -6\pi\mu R_o u \hat{\mathbf{e}}_{\mathbf{u}}, \quad (51)$$

where u is the particle speed and $\hat{\mathbf{e}}_{\mathbf{u}}$ is a unit vector in the direction of the particle displacement. Thermal convection is assumed to be minimal so that the fluid viscosity is relatively constant, and that acoustic streaming effects are minimal so that u is

dependent only on the primary radiation force. For 10 μm diameter polystyrene particles $u = 1 \text{ mm/s}$, corresponding to a viscous drag force of 189 pN.⁴⁵ Referring to Table 2, for the current chamber design, smaller radiation forces (and smaller particle speeds that are a consequence of the radiation force alone) can be expected. For any temporal analysis of particle movements within the chamber, steady-state viscous drag forces as well as unsteady drag forces must be considered; the time intervals for particle column formation to occur will be heavily dependent on the viscosity within the medium as well as the pressure field. But after particles have reached equilibrium positions, the viscous drag force will be minimized since $u \approx 0 \text{ mm/s}$.

3.6. Pressure Field Distortion

Oseen drag forces arise from distortions in harmonic pressure fields, and take into account particle inertial effects in the far field. They are defined as

$$\mathbf{F}_{\text{Os}} = -6\pi\mu R_o \hat{\mathbf{u}}(1 + D|u|) \quad (52)$$

where D is a constant specifying the extent of the distortion.⁵¹ Following the calculations for the minimum trap pressures of the particles in Section 6, the largest required trap pressure for current experiments is 118 kPa and for future experiments with red blood cells is 105 kPa. It is expected the maximum pressures within the chamber will not exceed 150 kPa (intensity 0.76 W/cm^2 at 500 kHz). For a shock number of 1, and field intensity 2 W/cm^2 , distortion will not occur until the pressure wave has travelled more than 100 cm from the transducer.⁷⁷ Therefore for the current chamber geometry, Oseen forces arising from distortion will be negligible.

3.7. Brownian Motion and Diffusion

The force arising from Brownian diffusion is

$$F = -K_B T \nabla(\ln \psi) \quad (53)$$

where K_B is the Boltzmann constant, T is the temperature, and ψ is the probability density for finding particles at a given location in the medium. Generally, this force is negligible until $R_o \leq 1 \mu\text{m}$,³⁵ which except for the case of $0.5 \mu\text{m}$ diameter polystyrene microspheres did not occur in the study.

3.8. Influence of Hydrostatic Pressure Gradients

The maximum hydrostatic pressure in the chamber is $P_{hyd} = \rho g Z = 490 \text{ Pa}$ for $Z = 5 \text{ cm}$. The hydrostatic pressure gradient is therefore $29 \text{ Pa}/\lambda$ at 500 kHz . Since except for very small-diameter gas bubbles the acoustic pressures are much greater than the hydrostatic pressure, the forces arising from the hydrostatic pressure gradient are negligible.

3.9. Cavitation and Rectified Diffusion

Cavitation is the process whereby gas-phase cavities (bubbles) are generated from gases dissolved in a liquid medium. For acoustic waves, the negative phase of the cycle produces regions of low pressure where cavitation might occur. Initially bubbles formed are tiny, on the order of 10 to 100 nm. But they are spherical radiators and will oscillate with and amplify the acoustic pressure field, inducing further cavity formation. Consequently, cavities grow in size - a process known as rectified diffusion because dissolved gases are preferentially pumped into the cavities.

Cavitation and rectified diffusion are problematic. They have been implicated in the development of localized turbulence and acoustic microstreaming, and induce generation of secondary radiation forces which are unpredictable because the bubble diameters are not fixed in size. The best means to control cavitation and rectified diffusion is to use a degassed medium, under pressure.

Table 2. Summary of Major Forces for 3 Particles

Particle Force	Particle		
	Gas	Solid	Solid/liquid biologic
	Isobutane 9.0 μm diameter	Polystyrene 19.0 μm diameter	Red Blood Cells 4.0 μm diameter
Primary Radiation Force - Axial (N)	1.059×10^{-12}	1.163×10^{-14}	3.263×10^{-17}
Primary Radiation Force - Lateral (N)	3.026×10^{-13}	3.323×10^{-15}	9.323×10^{-18}
Secondary Radiation Force $\theta = 90^\circ, d = 2R_o$ (N)	4.526×10^{-9}	3.472×10^{-20}	1.634×10^{-21}
Secondary Radiation Force $\theta = 90^\circ, d = 100 \mu\text{m}$ (N)	3.658×10^{-11}	2.210×10^{-22}	5.085×10^{-27}
Drag Force (N) ^b for particle speed $u = 20 \times 10^{-3}$ m/s	3.393×10^{-9}	7.163×10^{-9}	1.508×10^{-9}
Maximum particle speed u (m/s) ^c	0.012×10^{-3}	0.065×10^{-6}	86.5×10^{-9}

a - all forces calculated at a peak pressure of 150 kPa at 500 kHz using a 19 mm plane piston radiator.

b - case for maximum acoustic streaming velocity reported.

c - maximum u developed to achieve a viscous drag force equal to the axial primary radiation force. Secondary radiation forces are not considered in the calculation.

4. ENGINEERING DESIGN & METHODS OF STUDY

4.1. Chamber Design

The basic concept of the acoustic levitation chamber follows the work of Asaki,⁷⁸ Crum,⁴⁸ Tolt³⁶ and Whitworth.⁴⁹ In these designs the purpose was to generate concentrated particle columns, and utilized narrow-width chambers and direct coupling between the transducer and the chamber. Within this thesis, the particle column geometry and dimensions are of interest, and avoid any mechanical coupling between the field and the chamber.

Our chamber is a 110 mm diameter cylindrical plexiglas water tank that is mounted on a nylon support base (Figure 5). Depending on the particles to be levitated, one of three narrowband, piezoelectric transducers are used: I) Valpey Fisher ILO506HR (lithium niobate), II) Etalon LIHP-40-5019-SCB1, and III) Valpey Fisher E0107 (PZT-4). Specification data for the transducers may be found in Table 3. Transducer I has a low power rating and low electro-mechanical coupling, making it suitable for use with small gas-phase particles. Transducer II has a high power rating and high electro-mechanical coupling, so it is capable of levitating all particles used in this study (Figure 6). Transducer III has a low power rating but high electro-mechanical coupling, making it suitable for the full range of particles within the limitations of its power rating. A chamber-transducer system exhibits a resonant behavior different from the resonant behavior of the chamber or transducer alone. It is necessary to minimize these chamber resonances, contrary to the work of the aforementioned researchers, so that the chamber-transducer system may be characterized

by the transducer resonances alone.^{58(ch.10, pp.280-282)} In this manner, the pressure field in the chamber will accurately match the pressure model, described by Equation (29). To prevent chamber resonances in the axial and lateral directions, direct mechanical coupling of the chamber and transducer is avoided in the design by using a specially designed silicon rubber O-ring, which also serves as a water seal. Indirect coupling via the developed pressure field may occur if energy is transmitted from the field into the plexiglas. This causes the chamber to act as a resonant cavity with its normal modes given by solutions of the Helmholtz equation, a time-invariant form of the 2D homogeneous wave equation. The reflection and transmission coefficients are found using $R = (\rho_2 c_2 - \rho_1 c_1) / (\rho_2 c_2 + \rho_1 c_1)$ and $T = 1 + R$. Based on Table 4 the transmission coefficient for the water/plexiglas surface is 0.611, so some acoustic energy will be transmitted into the plexiglas. This energy might be retransmitted into the medium at axial resonance frequencies of the chamber. Because the chamber includes a base reflector to enhance standing wave generation at the transducer fundamental operating frequency and since plexiglas is not a perfect reflector, chamber axial resonances cannot be avoided with the current design.

However, perturbation of the pressure field by the chamber walls can be minimized, preventing the occurrence of possible lateral resonant modes. Rather than narrow water columns similar to previous researcher's work,^{36,48,49,78} wide-walled chambers can be used to help minimize lateral resonances. Setting pressures at the chamber walls to be < -20 dB referenced to the axial centerline, the chamber diameter may be found using $(ka l_r) / (l_z - l_N) \geq ka \sin(\theta) = 7.02$, where l_r is the chamber radius, l_z

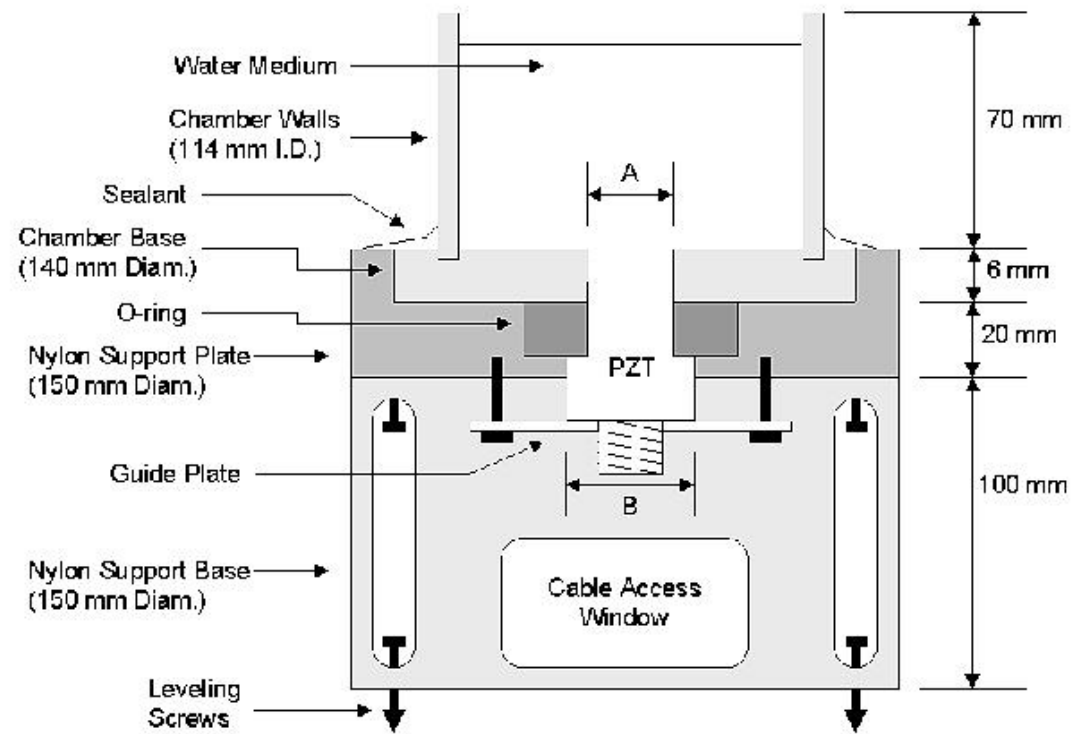


Figure 5. Above is an assembly schematic of the acoustic levitation chamber. A and B are dimensions unique to transducers I, II and III.

Table 3. Transducer Design Specifications

Transducer	I	II	III
Manufacturer	Valpey Fisher	Etalon	Valpey Fisher
Model	ILO506HR	LIHP-40-.5019-SCB1	E0107
Navy Type	II Immersion	I Immersion	I Immersion
Crystal	Lithium Niobate	Proprietary	PZT-4
Crystal d_{33}^a ($\times 10^{-12}$ m/V)	6	330	295
Crystal SE_{33}^b ($\times 10^{-12}$ m ² /N)	5.0	15.5	15.5
Crystal M_o^d (N ² /V ² m ²)	1.4	453.3	362.2
Crystal k_{33}^c	0.485	0.700	0.490
Crystal Sound Speed (m/s)	7340	3831	3960
Diameter (mm)	19.05	19.00	17.78
Thickness (mm)	6.50	3.50	3.90
Frequency (kHz)	568	544	505
Bandwidth (%)	59.9	36.8	14.5
Backing Type	High Res	High Power	Air-backed
Backing Imped.	Medium	Medium	Low
Matching Layer	Pink Alumina Oxide	Pink Alumina Oxide	None
Focusing	None	None	None
Near/ Far Field Transition (mm)	33.9	32.3	26.1
Power Rating (Watts)	0.125	60	10 ^e
Duty Cycle (%)	100	100	100
Tuning Electronics	Internal	External	Internal
Electrical Imped. (Ohms)	50	53	50
Phase Angle (°)	0	-14	0
Max. Intensity (Watts/cm ²)	48.7 μ	32.8	3.2
Max. Pressure (kPa)	1.2	985	309

a - displacement coefficient d_{33}

b - elastic compliance coefficient SE_{33}

c - electrical/mechanical coupling coefficient k_{33}

d - material figure of merit $M_o = (d_{33}/SE_{33})^2$

e - 0.125 Watts according to manufacturer

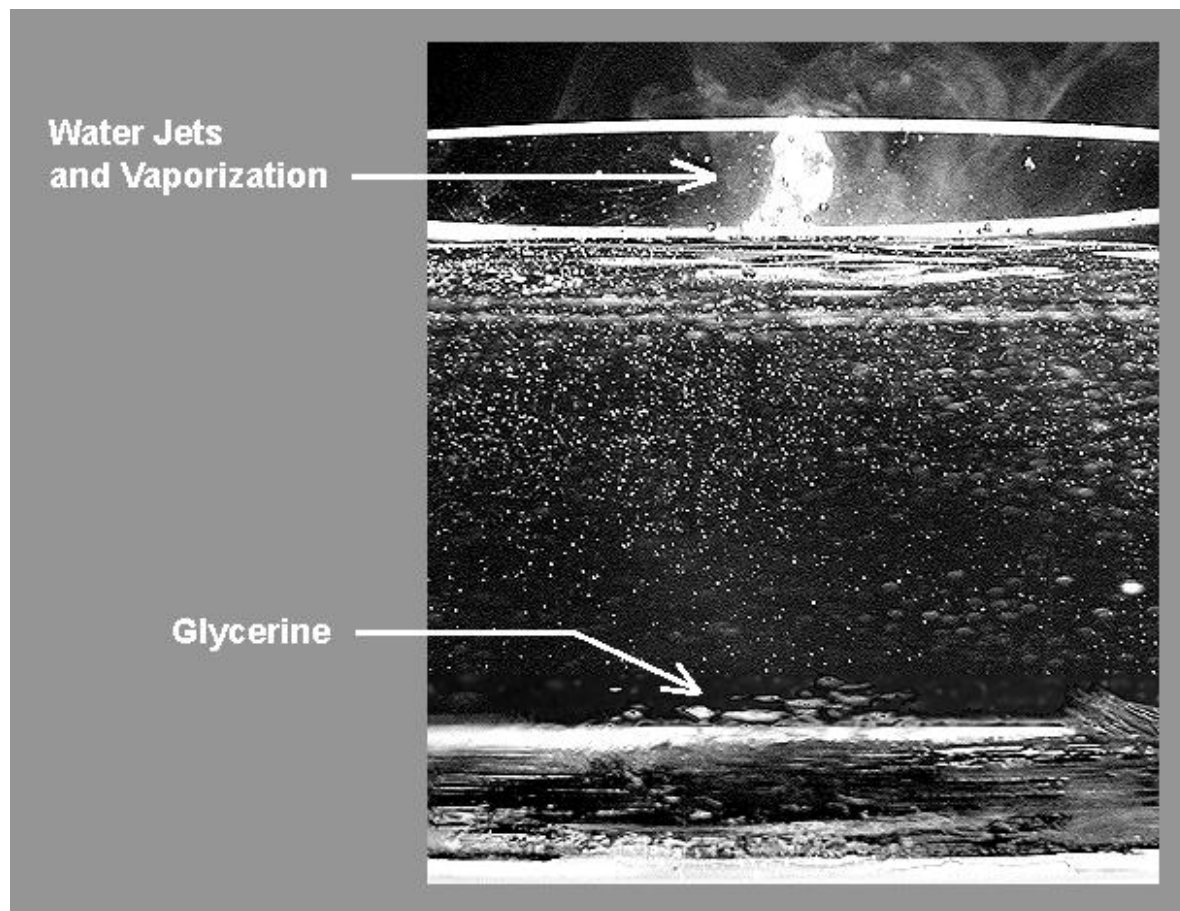


Figure 6. Transducer II is unfocussed, yet has sufficient power to cavitate, generate water jets and vaporization, and lift glycerine from the base and begin to form it into columns. Drive voltage is 123.6 volts peak-peak.

Table 4. Chamber and Medium Material Properties

Material	Density (g/cm ³)	Sound Speed (m/s)
Plexiglas	1.150	2700
Nylon	1.120	2600
Silicon Foam Rubber ^a	1.180	1050
Air	1.290x10 ⁻³	344
Water ^b	0.998 ^c	1489 ^d
Plasma ^e	1.030 ^f	1540 ^g

a - used to minimize chamber resonances in Section 5

b - at temperature of 22 °

c - data obtained from Kaye and Laby⁵³

d - data obtained from Greenspan⁵⁴

e - at physiologic temperature of 37 °C

f - data obtained from Wladimiroff⁷⁹

g - data obtained from Dintenfass⁸⁰

h - all other values obtained from Specialty Engineering Associates⁸¹

is the distance from the transducer surface to the water/air surface, l_N is the distance from the transducer surface to the near/far field transition region, k is the magnitude of the wavenumber, a is the transducer radius, θ is the transducer beam half angle (see Figure 1), and $j_{1n} = 7.02$ is the solution for the second zero ($n = 2$) of the directivity function $2J_1(j_{1n})/j_{1n}$ (which is greater than a 50% (-20 dB) pressure drop). For a 19.0 mm diameter transducer operating at 505 kHz in a water medium of temperature 22 °C, $l_N = 29.9$ mm and $k = 2.13$ mm⁻¹. Thus for a water height $l_z = 70$ mm, the chamber radius $l_r \geq 13.9$ mm. Due to material availability, a chamber radius of 57.1 mm was used.

To maximize the generation of standing waves, the transducer sound beam should be normal to both the water/air surface and chamber base. To achieve this, the transducer insertion hole in the chamber base is machined normal within 50 μ m

tolerance, and a transducer guide plate is installed. Sound beam alignment normal to the water/air surface is performed using three leveling screws in a tripod arrangement built into the chamber support base. This alignment system can correct for less-than-ideal conditions in the chamber, but it cannot correct for crystal misalignment within the transducer housing. To minimize vibration, all experiments are performed on a laboratory vibration damping table (Technical Manufacturing Corporation 63-553).

Sound waves within the chamber are generated by driving the transducers with a continuous wave sinusoidal voltage or CW burst (see Figure 7). To ensure that input power is within the specified power ratings, the transducers are driven at resonance with CW bursts at duty factor ≤ 1.0 (experimentally, standing waves sufficient for particle levitation were formed at duty factor ≥ 0.4).

Standing waves are formed within the chamber when the distance between the transducer surface and the water/air surface is an integer number of half-wavelengths. This distance is dependent on the transducer operating frequency and the water temperature. For the experiments, the water height was chosen to be between 16 and 20 wavelengths, 41.7 to 54.6 mm, and the chamber height is 70 mm. Water heights were measured via the roundtrip pulse-echo time and the equation $Z = ct/2$ (see Figure 8).

4.2. Methods of Study

Consistent with the hypotheses of Section 1, there are three areas of research: measurement and prediction of the pressure field, prediction of the forces on particles within the pressure field, and measurement of particle levitation within the chamber.

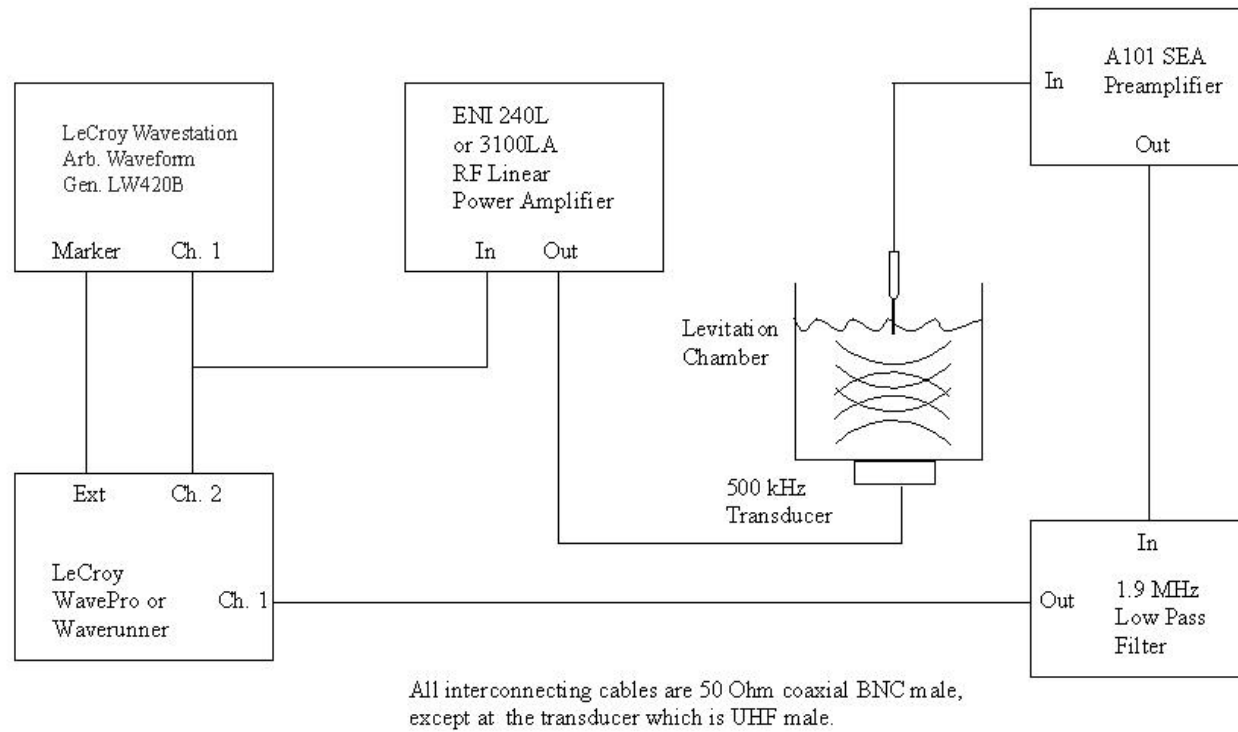


Figure 7. Electrical schematic for chamber operation. The Specialty Engineering Associates 0.4 mm diameter polymer (PVDF) needle hydrophone was used for manual and automatic pressure mapping of the chamber.

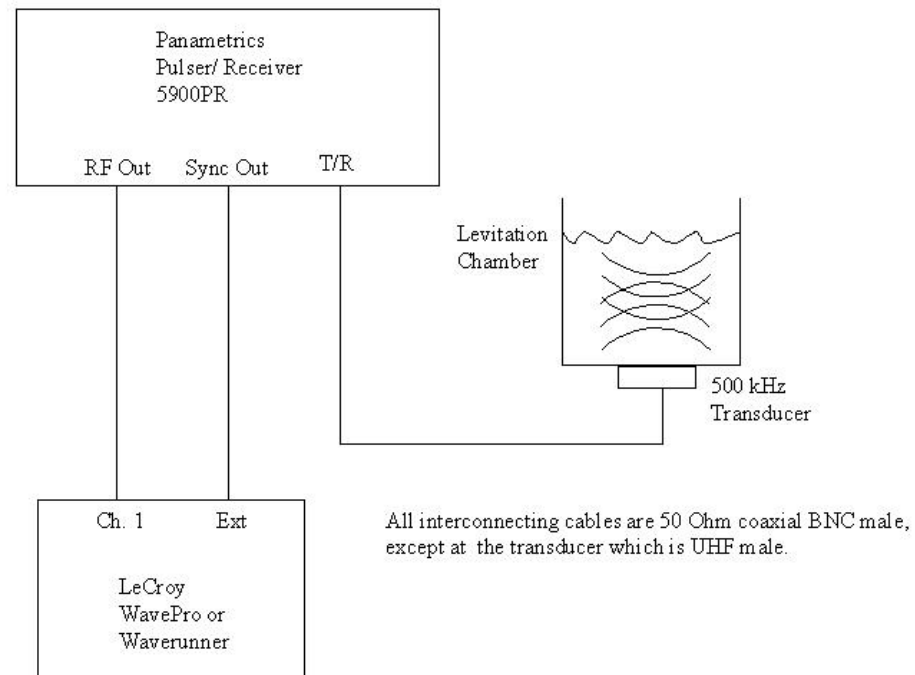


Figure 8. Electrical schematic for measurement of the levitation chamber water height using the Panametrics 5900PR pulser/receiver.

4.2.1. Pressure Fields and Forces

Measurements and prediction of the chamber pressure field are discussed in Section 5. Prediction of the forces on particles within the pressure field is discussed in Section 6.

A model of the standing wave pressure field topography consistent with Equation (29) was developed with the aid of the Field II program⁸² and Matlab. However, Equation (29) is a relative pressure amplitude model. Using Equation (48), the model was re-scaled to establish absolute pressure magnitudes at any point in the field topography. The model was then tested with manual and automatic pressure mapping of the chamber using a cross-calibrated Specialty Engineering Associates 0.4 mm diameter polymer (PVDF) needle hydrophone (see Figure 14). For manual pressure measurements, the hydrophone was attached to a Velmex A4012Q1-S4 XYZ graduated knob Unislide assembly which allowed accurate positioning within 0.1 mm. For automatic pressure measurements, a Parker Daedal XYZ positioner with Galil motion controller was used, which allowed accurate positioning within 100 nm (see Figure 9). For signal acquisition, the hydrophone was connected to a Specialty Engineering 20 dB Gain A101 preamplifier and a LeCroy WavePro 940 oscilloscope that digitized waveforms at 20 MSamples/sec and 8 bit amplitude resolution (see Figure 7). High frequency noise was minimized by using a 1.9 MHz low pass filter. Data signal transfer from the LeCroy Wavepro to the PC was performed with custom VIs developed with Labview.

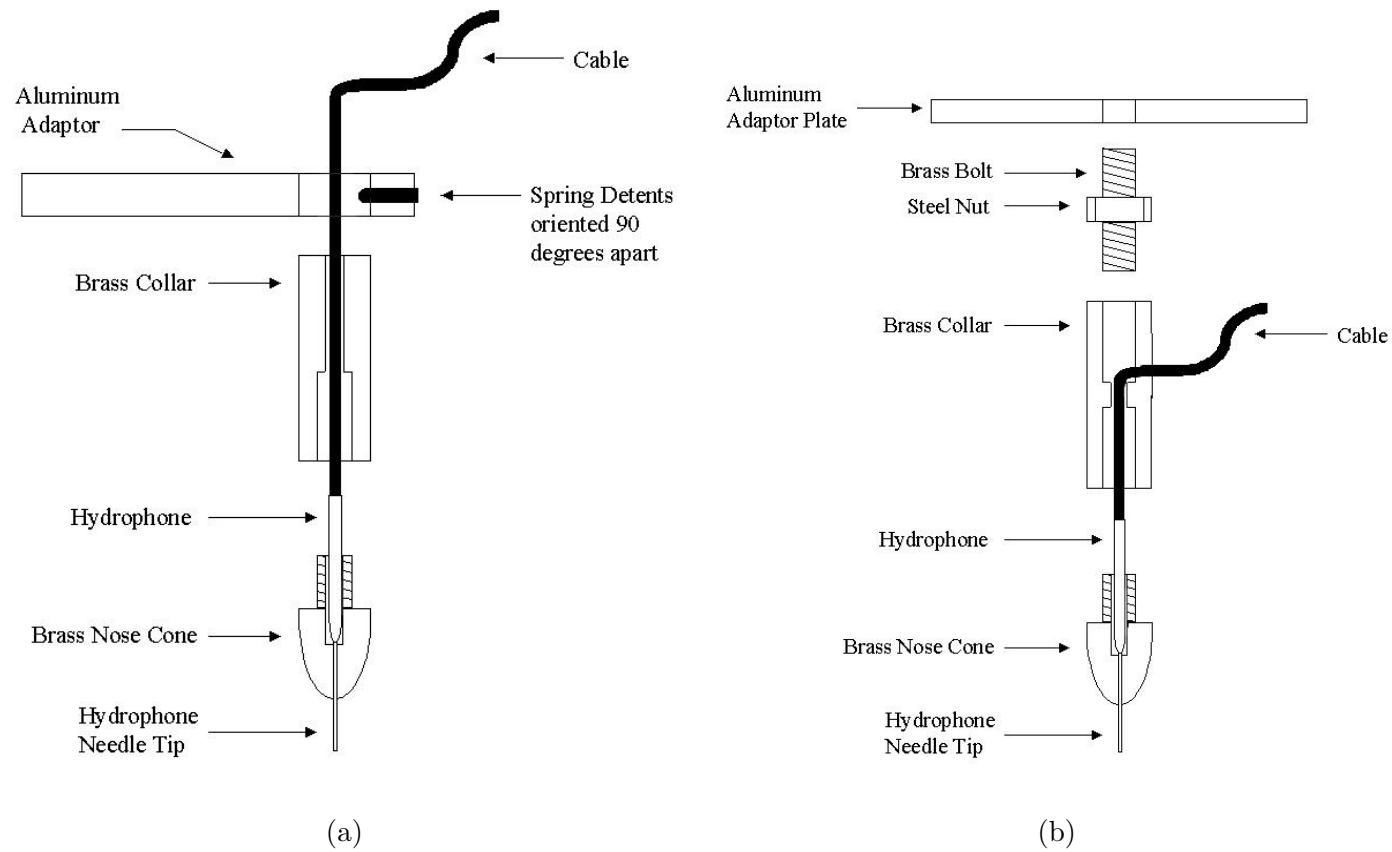


Figure 9. Hydrophone assembly schematic for (a) manual and (b) automatic pressure mapping with the Specialty Engineering Associates 0.4 mm diameter polymer (PVDF) needle hydrophone. The aluminum adaptors were mounted to (a) a Velmex A4012Q1-S4 XYZ graduated knob Unislide assembly and (b) a Parker Daedal XYZ positioner with Galil motion controller.

4.2.2. Hydrophone Selection

The polymer needle hydrophone is used for pressure mapping and measurement of minimum trap pressures during the particle levitation experiments. It has a small physical profile and broad frequency response, is ideally suited for close-quarter pressure mapping, and with a 0.4 mm diameter aperture will allow mapping at a lateral resolution of > 0.4 mm (0.5 mm used) without spatial oversampling. The hydrophone was cross-calibrated to two other calibrated needle hydrophones (Specialty Engineering Associates No. 589 and No. 610, 0.2 mm diameter).

Using a LeCroy LW420B Wavestation arbitrary waveform generator together with a ENI 240L 40 Watt radio frequency linear power amplifier, transducer I was driven with a pulsed 20 cycle sinusoidal voltage at 0.025 (1/40) duty factor and 95 Volts peak-peak amplitude. The frequency of the signal was varied from 500 kHz to 3.5 MHz, in 250 kHz increments, and voltage signals were measured for the three hydrophones. At any frequency for a fixed pressure amplitude the following formula was applied:

$$\frac{G_{v1}}{V_1} = \frac{G_{v2}}{V_2} = \frac{G_{v3}}{V_3}, \quad (54)$$

where the subscript refers to one of the three hydrophones, G_v is the voltage gain and V is the voltage signal. By knowing the voltage gain of the calibrated hydrophone, G_{v1} (or G_{v2}), and measuring the voltage signals V_1 (or V_2) and V_3 , the voltage gain G_{v3} of the uncalibrated hydrophone can be found.

The No. 589 and 610 hydrophones were previously calibrated by Specialty Engineering Associates in the frequency range 1 MHz to 20 MHz, so that baseline voltage gains G_{v1} and G_{v2} at each frequency above 1 MHz were available for the cross-

calibrations. Polymer needle hydrophones typically are non-linear below 2 MHz and highly non-linear below 1 MHz. For our purposes, a linear extrapolation method was chosen to predict the voltage gains G_{v1} and G_{v2} at 500 kHz. In so doing, an error of ± 1 dB can be expected in the results. From an analysis of the frequency response and subsequent measurements it appeared the No. 589 hydrophone may have been poorly calibrated (or drifted from its calibration), so it was not used. Results of the cross-calibration are shown in Table 5.

Polymer needle hydrophones do not always have similar response characteristics due to the manufacturing process. Inaccuracies in the cross-calibration will occur if hydrophones with similar response characteristics are not used. None of the polymer needle hydrophones used had similar response characteristics, so additional small errors in the calibration may be present. Overall the pressure measurements in subsequent sections can be considered to be calibrated within ± 2 dB.

4.2.3. Particle Levitation

After demonstration of the pressure and force models, for completeness, levitation of gas-phase, solid particles and liquids within the chamber will be performed. First, it will be qualitatively demonstrated that the chamber can levitate particles. Then, quantitative testing will be performed through comparison of measured minimum trap pressures to predictions from the validated force model. Table 6 summarizes the particles to be used in these experiments, and represents all particle types.

Cavitation and acoustic streaming require careful management during particle levitation. Cavitation was minimized by using deionized, degassed water since most

Table 5. Hydrophone Cross-calibration

Frequency (MHz)	Gain (dB ref. 1 Volt/ μ Pa)	
	Model No. 610	
	0.2 mm Calibrated	0.4 mm Cross-calibrated
0.50	-258.55	-247.31
0.75	-258.06	-249.66
1.00	-257.60	-251.36
1.25	-258.82	-254.27
1.50	-256.52	-252.03
1.75	-256.37	-252.73
2.00	-255.90	-254.19
2.25	-255.10	-255.28
2.50	-254.63	-256.00
2.75	-254.02	-257.16
3.00	-253.32	-259.21
3.25	-253.02	-261.16
3.50	-252.67	-262.75

of the experiment sets in the current research required pressures up to 80 kPa. Above this value, static pressurization of the chamber would be beneficial to prevent rectified diffusion and subsequent cavitation effects, but the same pressurization would severely limit spatial mapping of the pressure field, and so was not used. Based on the discussion in Section 3, acoustic streaming was managed utilizing low-attenuation phantoms inserted within the acoustic levitation chamber (Figure 10). The phantoms were simple to insert and remove from the chamber, allowing easy cleaning of the chamber between experiments. The phantom recipe in Table 7 is a modification of tissue-mimicking phantom recipes used in this laboratory. Attenuation measurements and sound speed calculations for the phantoms were performed using

Table 6. Particle Properties

Particle	Type	Diameter R_o (μm)	Density ρ_o (g/cm^3)	Sound Speed c_o (m/s)
decafluorobutane ^a	encap. gas	3.0	11.2×10^{-3}	100
air	unencap. gas	35.0 ^b	1.3×10^{-3} ^c	344 ^c
isobutane ^a	encap. gas	9.0	130.0×10^{-3} ^d	120 ^d
isobutane ^a	encap. gas	40.0	130.0×10^{-3}	120
isopentane ^a	encap. gas	30.0	135.0×10^{-3}	100
polystyrene	solid	0.5	1.050	2500 ^c
polystyrene	solid	15.5	1.065	2500 ^c
polystyrene	solid	19.0	1.064	2500 ^c
cornstarch	solid	N/A	N/A	N/A
glycerine	liquid	N/A	1.260 ^c	1920 ^c
food coloring dye	liquid	N/A	N/A	N/A
red blood cells ^e in isotonic sol. (I)	biologic	4.0	1.099 ^f	1646 ± 7 ^f
red blood cells ^e in isotonic sol. (II)	biologic	4.0	1.100 ^g	1600 ^h
red blood cells ^e in plasma (I)	biologic	4.0	1.099 ^f	1631 ^f
red blood cells ^e in plasma (II)	biologic	4.0	1.100 ^g	1600 ^h
red blood cells ^e in hypotonic sol.	biologic	4.0	1.056 ^f	1577 ± 5 ^f

a - for encapsulated gases, density and sound speed are based on the shell/gas composite

b - estimated, via syringe injection

c - values obtained from Specialty Engineering Associates⁸¹

d - used values from Pierce & Stevens (manufacturer of 40 μm diameter isobutane)

e - not used in current experiments, shown for comparison only

f - values obtained from Weiser⁸³

g - values obtained from Dintenaus⁸⁰

h - values obtained from Wladimoff and Talbert⁷⁹

i - all other values obtained from manufacturers

a through-transmission method with a 5 MHz broadband transmit/receive transducer pair operating at 2.5 MHz.^{84,85} Results of these measurements are summarized in Table 8.

Particle illumination was accomplished with a Dolan-Jenner Industries Inc. Fiber Lite 181 high intensity fiber optic illuminator, and an Opti-Quip 1200 mercury arc lamp. To reduce thermal gradients, extended hot mirrors (Edmund Industrial Optics, 425-675 nm transmission/ 750-1150 nm reflection) were used to remove infra-red and to limit light within the medium to the visible and ultraviolet spectrums. Photographs of the particle levitation experiments were made with an Olympus Camedia C3030 digital zoom camera. Since the chamber wall diameter necessitates a large water volume, achieving particle concentrations within the chamber was problematic. During photography, smaller diameter thin-walled clear plastic tubes were inserted within the chamber to improve particle concentration and aid in discerning column formation through the camera's depth-of-field.

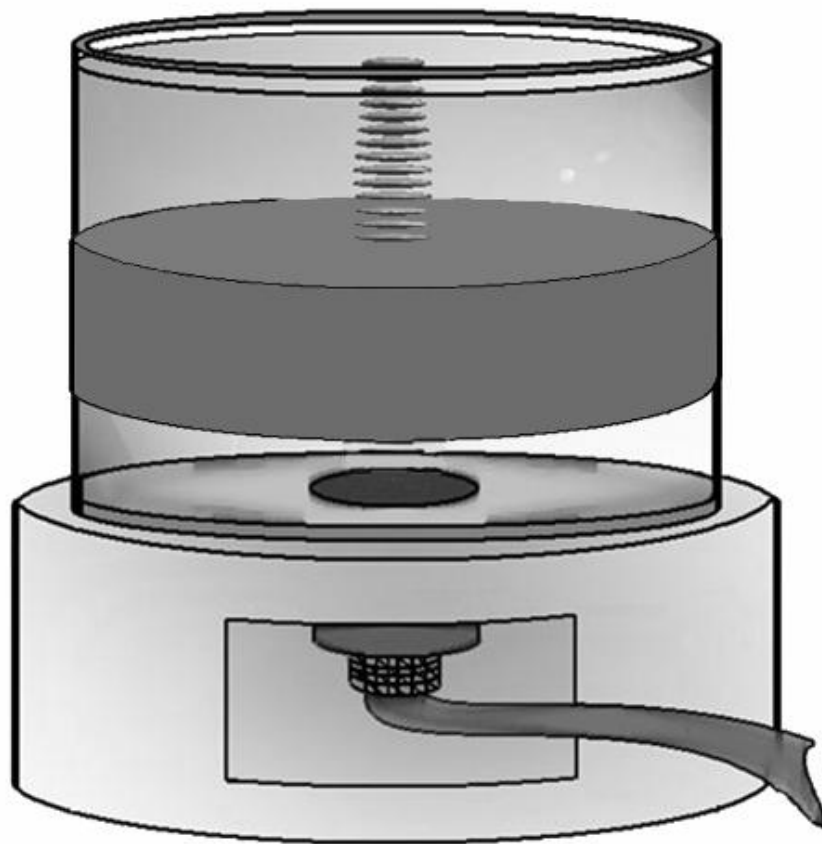


Figure 10. Above is a drawing of the acoustic levitation chamber with a low-attenuation phantom inserted to minimize acoustic streaming effects.

Table 7. Phantom Recipe Ingredients and Proportions

Ingredient	Deionized Water	1-Propanol	Formaldehyde (37%)	Agar	India Ink
Percentage by Weight	89.61	8.24	0.18	1.97	5 drops

Table 8. Phantom Attenuation Measurements

Test Sample	Temperature (° Celsius)	Density (g/cm ³)	Sound speed (m/s)	Error (%)	Attenuation (dB/cm)	Error (%)
Water medium	21.1	0.998 ^a	1486 ^f	–	–	–
Saran wrap	21.1	1.710 ^b	2504 ^b	–	–	–
TPX	21.1	0.830 ^c	2170 ^c	–	–	–
Expected castor oil	21.1	0.959 ^d	1487 ^d	–	3.667 ^f	–
Measured castor oil	21.1	0.959 ^d	1484 ^f	±0.4 ^f	3.299 ^f	±10.1 ^f
Agar phantom	21.1	$\rho = 1.015^e$	1486 ^f	±0.4 ^f	0.087 ^f	±10.1 ^f

a - density for water at temperature of 22 ° C⁵³

b - density and sound speed for saran wrap obtained from Dr. E. L. Madsen⁸⁶

c - density and sound speed for TPX obtained from Specialty Engineering Associates⁸¹

d - density and sound speed for castor oil obtained from Dunn⁸⁷

e - measured value

f - attenuation and sound speed calculations for castor oil and agar phantom performed using a through-transmission method at 2.5 MHz^{84,85}

5. STANDING WAVE PRESSURE FIELDS

5.1. Method

The traveling wave pressure fields were modelled using Field II⁸² for three unfocussed, 500 kHz transducers, previously labelled I, II and III in Section 4. The Field II program applies Fourier optics theory to plane piston theory to calculate the radio frequency (RF) signal at each axial and lateral resolution. At a minimum there are approximately 500,000 locations for which calculations are performed. To save computation time and to reduce the size of the data set, the envelope is calculated from this data. Later the original traveling wave field can be reconstructed by mixing the envelope with the carrier frequency.

The pressure fields were generated for two areas: 10 cm by 6 cm and 100 cm by 6 cm in the z - x plane. Whereas the former area was generated at an axial resolution of 50 μm and lateral resolution of 250 μm , to reduce Field II computation time, the latter area was generated at a lower initial axial resolution of 500 μm and lateral resolution of 250 μm . Using Matlab the axial resolution of the second area was increased to 50 μm , and the two pressure fields were merged into one field. The pressure field envelope for the first area is shown in Figure 11 for transducer I.

Simulations of standing wave pressure fields, shown in Figure 12, were generated. As previously stated, the traveling wave pressure signal was reconstructed from the envelope by mixing with the carrier frequency (568, 544 or 505 kHz). Then the signal was reflected at the water/air surface, located an integer number of half-wavelengths from the transducer surface, similar to the experimental chamber. To further save

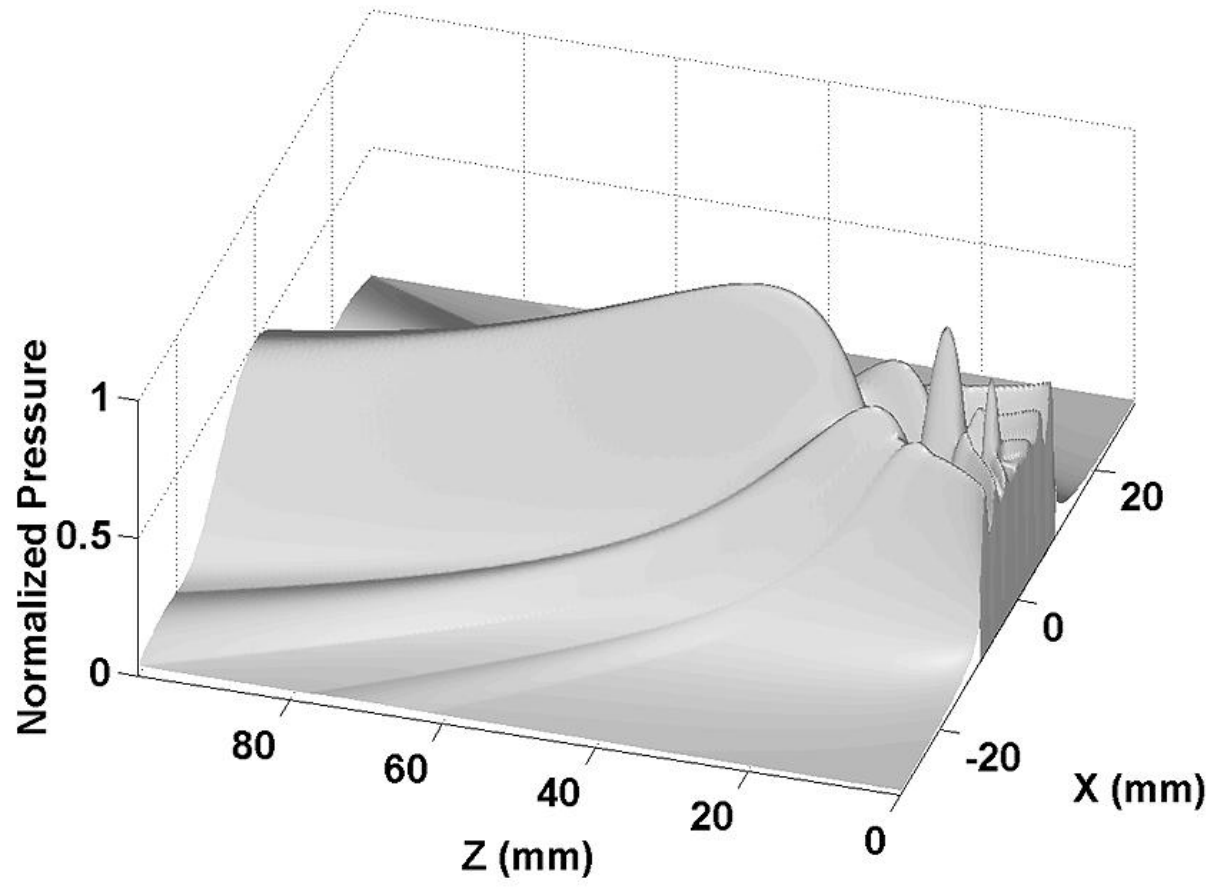


Figure 11. Envelope of the traveling wave pressure field is shown for transducer I. Data for this pressure field was generated from Field II for an area 10 cm by 6 cm.

computation time, after reflection the standing wave pressure field axial resolution was decreased to $250\ \mu\text{m}$ to match the lateral resolution. Parameters for modelling of the standing wave pressure field are shown in Table 9.

The pressure model of the standing wave accounts for multiple partial reflections at both the base and the water/air surface, so that it is accurately described by Equation (29). For the current chamber design, a reflection coefficient of $R_1 = -0.999$ was chosen for the water/air surface, and $R_2 = -0.389$ was chosen for reflections at the plexiglas base, using the chamber and material properties from Section 4. The influence of the chamber sidewalls is not considered in the model because the field intensity near the sidewalls is negligible.

The model of the standing wave pressure field topography is consistent with Equation (29). It is a relative pressure amplitude model. Using Equation (48), the model is re-scaled to establish absolute pressure magnitudes at any point in the field topography.

The standing wave pressure field topography consists of a series of pressure peaks known as antinodes, and pressure valleys known as nodes, and appear as stripes in Figure 12. To better visualize the 3D pressure distribution, the data for transducer I was replotted as a -10 dB beam contour in Figure 13.

Field II generates an accurate *relative* pressure field spatial topography but does not take into consideration the absolute magnitude, which is determined from the properties of the transducer crystal and drive voltage. From Equation (48) in Section 2, the pressure magnitude can be predicted from these parameters, and the

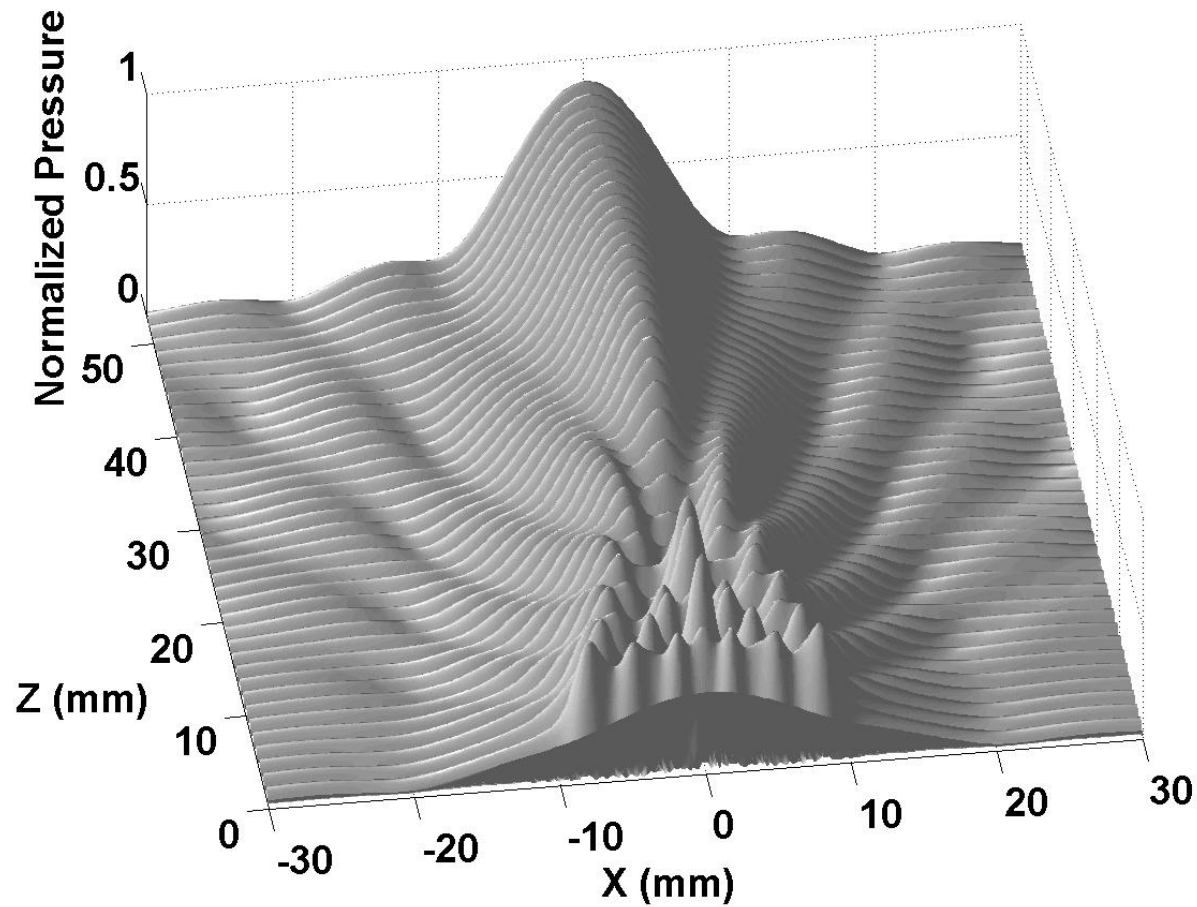


Figure 12. Envelope of the standing wave pressure field for a 19 mm unfocussed plane piston radiator operating at 505 kHz (transducer III in Table 9). Using Equation (29), pressure fields for all three transducers were constructed from their corresponding traveling wave pressure fields using the parameters in Table 9; an example of the traveling wave envelope for transducer I is shown in Figure 11.

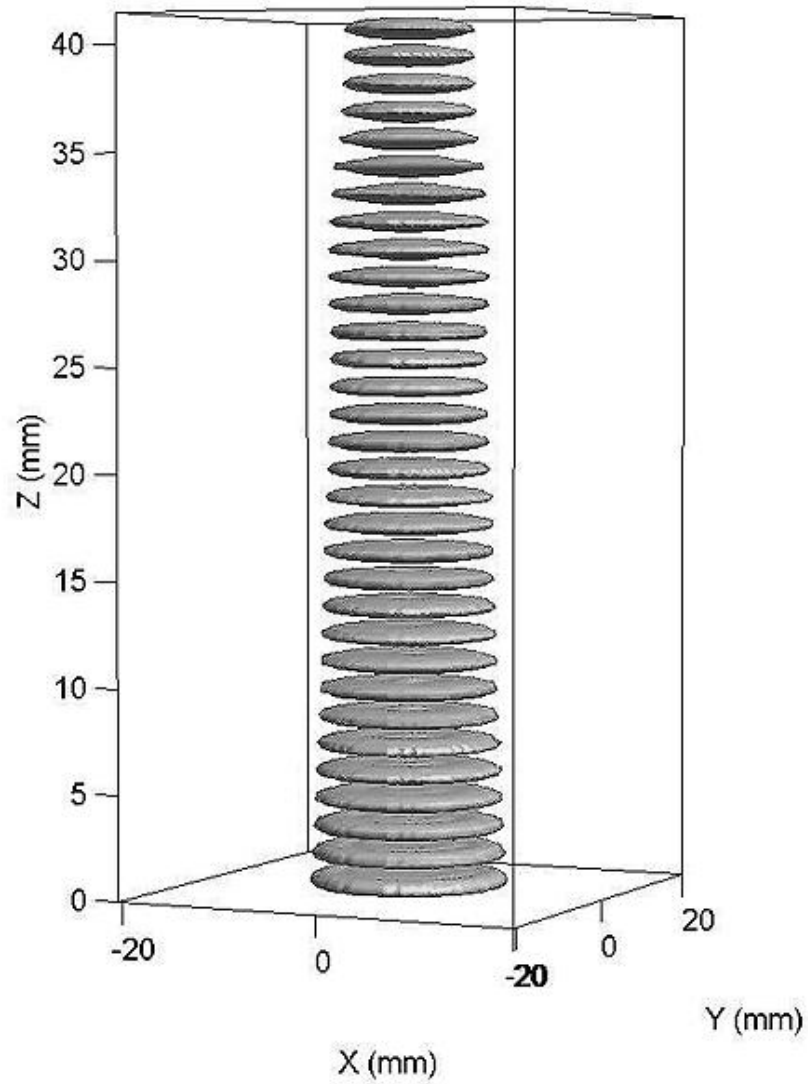


Figure 13. Shown above is a -10 dB standing wave beam contour of the modeled standing wave pressure field for transducer I, which is located at the $z = 0$ plane. The contour of each "saucer" corresponds to pressures 10 dB lower than the peak (axial centerline) pressure values.

Table 9. Standing Wave Model Parameters

Transducer	Frequency (kHz)	Sound Speed (m/s) ^a	Temperature (°C)	Distance between Reflectors (mm)	Multiples of $\lambda/2$
I	568	1481	19.5	41.7	32
II	544	1489	22.0	54.6	40
III	505	1489	22.0	53.0	36

a - sound speed calculated using formula provided by M. Greenspan⁵⁴

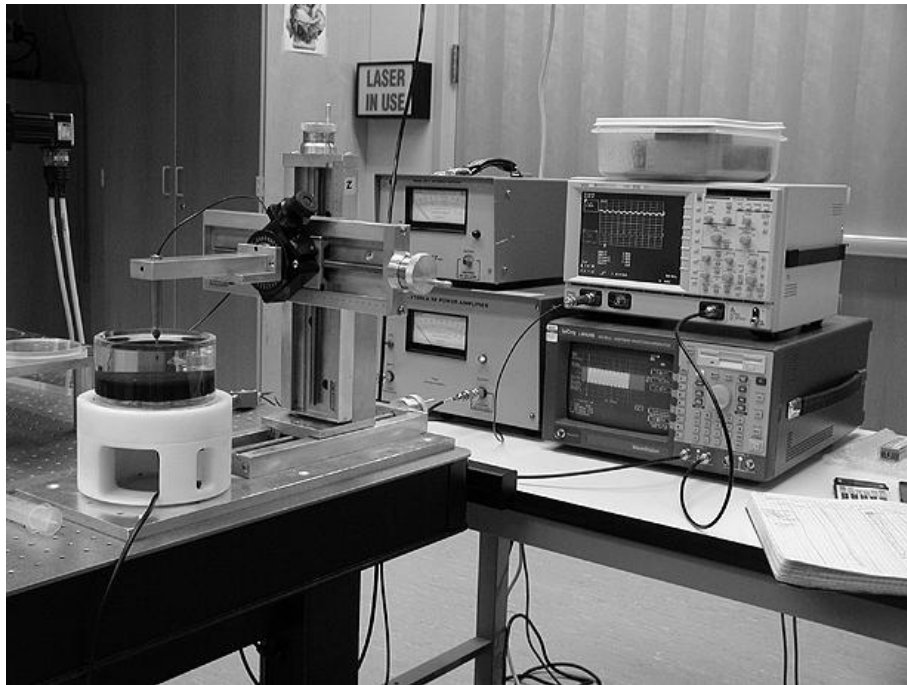
pressure field topography can be re-scaled accordingly. Predicted maxima within the chamber are shown in Figure 15 in Section 5.2.

To test how well the standing wave pressure field model predicts the pressure field developed in the chamber, manual and automatic pressure mapping of the chamber was performed with the cross-calibrated 0.4 mm diameter polymer needle hydrophone (photographs shown in Figure 14). Details of the equipment used in the pressure mapping have already been discussed in Section 4. Manual pressure mapping consisted of manually positioning the hydrophone at the locations of interest and running the Labview Hydra data capture VIs. Automatic pressure mapping consisted of a series of rectilinear plane scans also run under Labview at a 50 micron axial by 500 micron lateral resolution. The time to map any region in the field was considerable; map times varied between 5 and 47 hours depending on the volume measured.

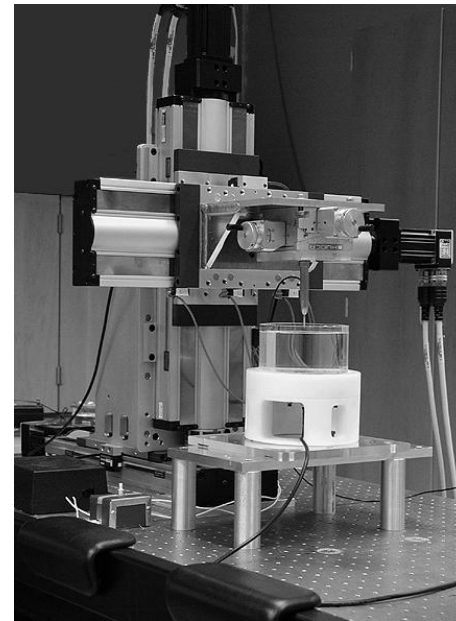
5.2. Results

Stable acoustic standing wave pressure fields sufficient for subsequent particle levitation experiments were generated CW bursts using a duty factor ≥ 0.4 .

Measured pressures at the near/far field transition region in the chamber were compared to the predicted pressures for a range of transducer drive voltages, as shown in Figure 15. Between 13 and 47 measured data samples were collected for each curve. According to the pressure model, Equation (29), the standing wave near/far field transition regions are locations of maximum pressure in the field. However, experimentally it was found the locations of maximum pressure did not correspond to this region (see Table 10). Even so, the peak pressure magnitudes predicted by



(a)



(b)

Figure 14. A photograph of the experimental setups for (a) manual and (b) automatic pressure mapping.

the model and measured in the chamber appeared to be in agreement (i.e. they just do not occur at the same pressure location).

Special mention for the data collection for transducer I is required. This data set was obtained when the transducer was driven above its power rating of 0.125 Watts up to 30 Watts during an experiment to ascertain its performance capabilities (a "burn" test). In contrast, the other two transducers were driven below their power ratings, 60 Watts for transducer II, and 0.125 Watts for transducer III. It was found despite the introduction of some small non-linear effects, transducer I could be driven up to 10 Watts for short time intervals less than 30 minutes without compromising the performance of the transducer.

Beam contour plots of measured and modeled standing wave pressure fields are compared in Figure 16 for transducer I in the near/far field transition region, 4.6 mm from the water/air boundary, and show good agreement.

Line plots along the axial centerline of the measured and modeled standing wave pressure fields were made; as an example the axial line plot of transducer III is shown in Figure 17. The measured peak pressures were 5.7, 11.6 and 16.2 kPa for transducers I, II, and III respectively. It is apparent some correlation between the measured and predicted data exists. However, there are significant disagreements.

In attempting to isolate the source of the differences, a Fourier spectral analysis of the pressure field along the axial centerline was performed for each transducer; as an example the spectral density corresponding to transducer III is shown in Figure 18. From this analysis it was discovered in addition to the fundamental and third

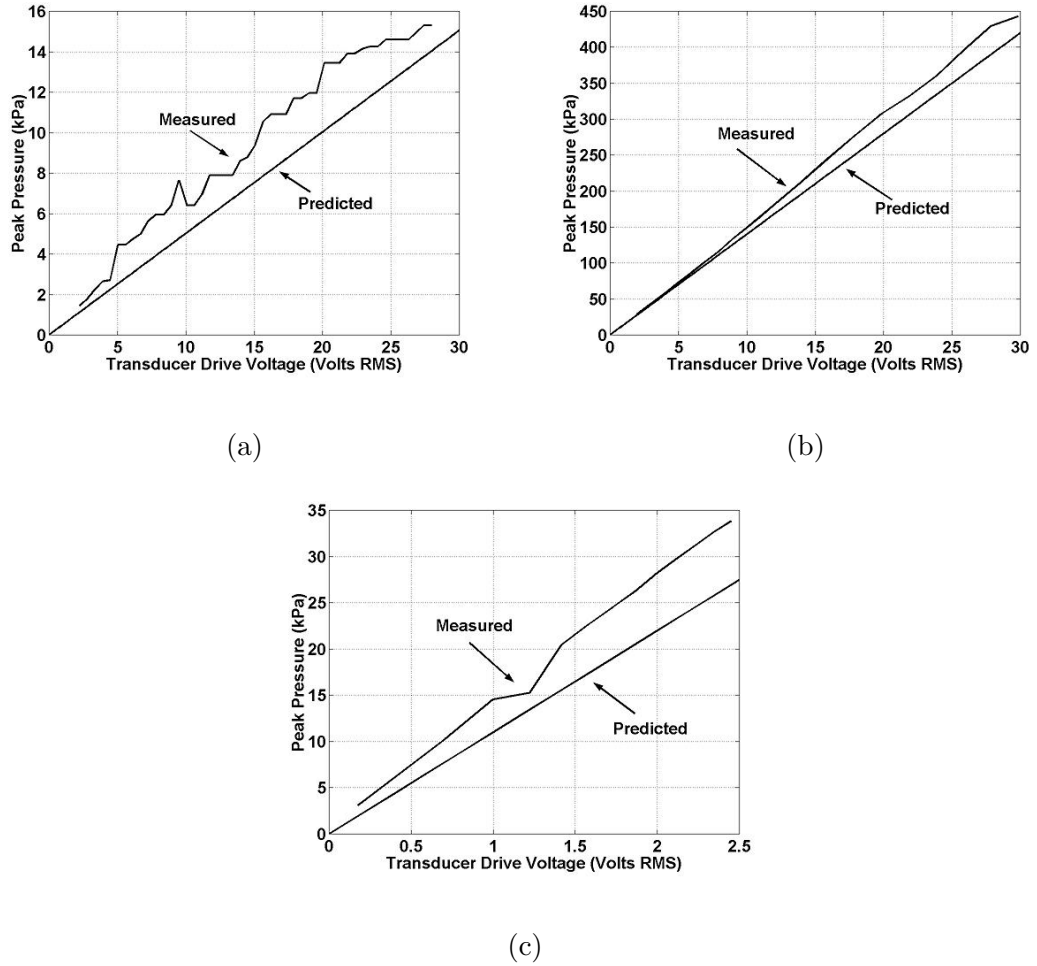
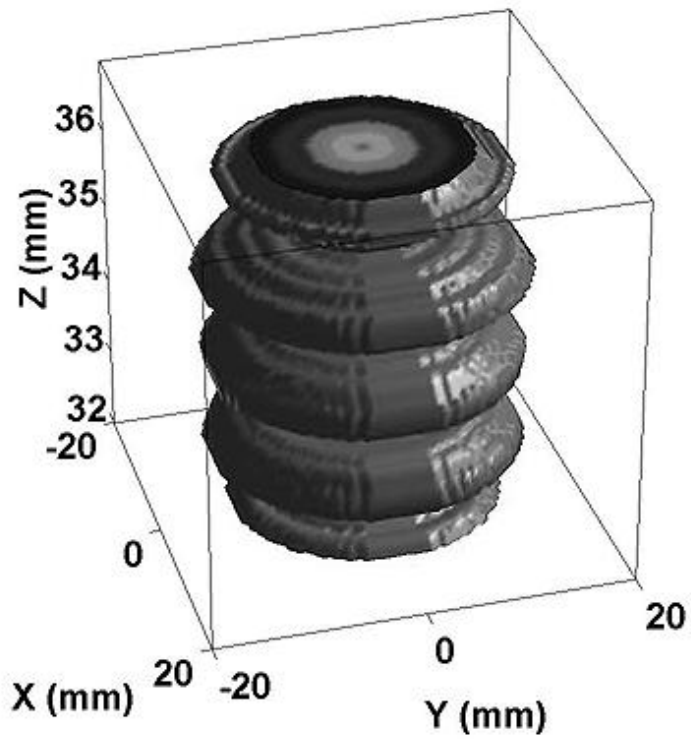


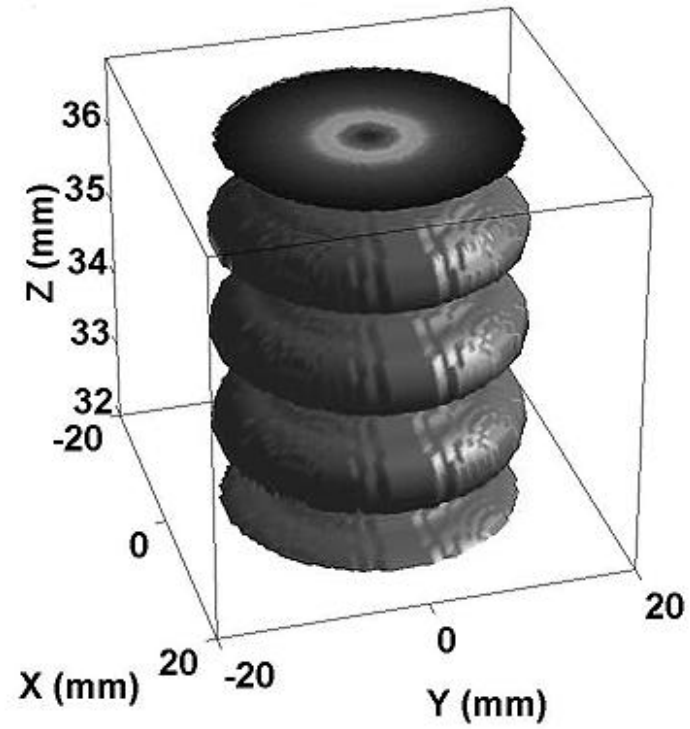
Figure 15. Magnitude of maximum measured and predicted pressures verse voltage for transducers (a) I, (b) II, and (c) III in the chamber. Manufacturer power ratings for the transducers correspond to (a) 2.5, (b) 56.4, and (c) 2.5 volts RMS at a duty factor of 1.0. Corresponding maximum pressures at these voltages are (a) 1.2, (b) 985, and (c) 309 kPa.

Table 10. Locations of Maximum Pressure

Transducer	Frequency (kHz)	Predicted Location (mm)	Measured Location (mm)
I	568	35	21
II	544	33	44
III	505	27	31



(a)



(b)

Figure 16. Shown above are -20 dB standing wave beam contours within the near field/far field transition region of measured (a) and modeled (b) standing wave pressure fields for transducer I. Cross-sections at the top show the pressure distribution near the antinodes.

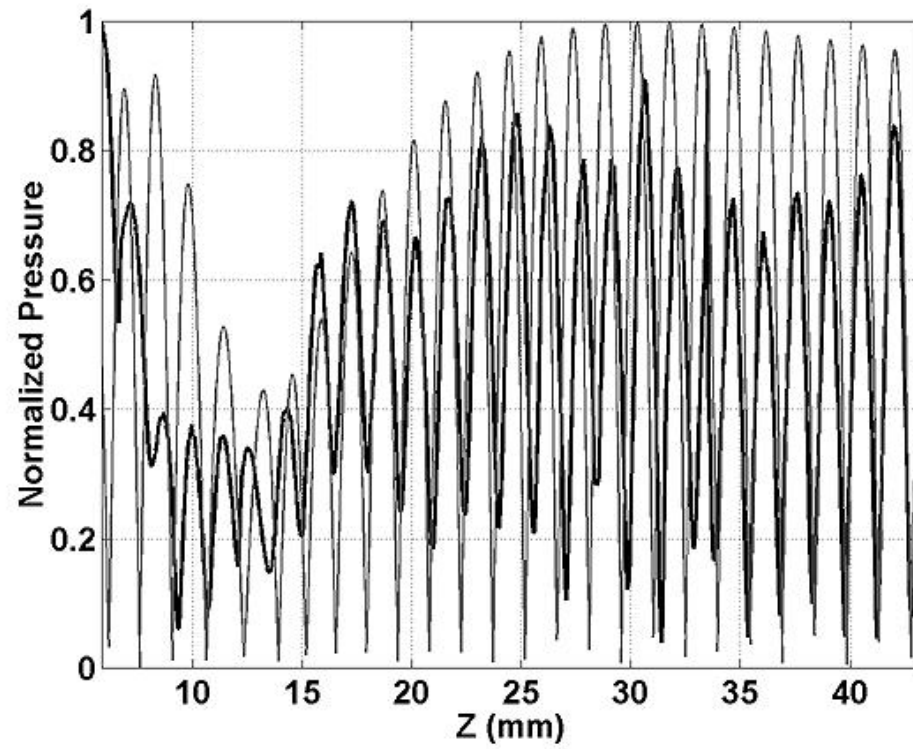


Figure 17. Axial centerline profiles of experimentally measured (thick solid line) and modeled (thin solid line) standing wave pressure fields for transducer III driven at its resonant frequency. Each plot was normalized to its own pressure maximum.

harmonic resonances of the transducer, a non-linear second harmonic resonance occurs. Also, subharmonics (chamber fundamental and third harmonics) exist which are significantly stronger than the transducer second harmonic resonance. The subharmonics clearly correspond to the axial distance between the transducer surface and the water/air surface.

To verify that the transducer beam was axisymmetric and to see if the presence of the chamber walls perturbs the pressure field, surface plots of the lateral planes of the measured pressure fields for transducers I and II are shown in Figure 19. The peak pressures were 5.7 kPa and 57.9 kPa, respectively. At the lower pressure produced by transducer I, the measured pressure field has good agreement with the pressure model. However, at the higher pressures produced by transducer II, the measured pressure field does not agree with that predicted, suggesting the field may be perturbed by the chamber wall.

5.3. Discussion

The questions of interest regarding the pressure field are 1) can one accurately predict the standing wave pressure field in the chamber using Equation (29) and Field II, and 2) can one measure this field without perturbing it?

Referring to Figure 15, an approximately linear relation exists between pressure and drive voltage. Hence it appears the pressure may be predicted if the transducer crystal properties are known (i.e. the material figure of merit M_o and crystal thickness t_c). The deviations seen in the figure are attributable to inaccuracies in the slope $\sqrt{2M_o}/t_c$ of Equation (48), and a 5.7% error attributable to a hydrophone calibration

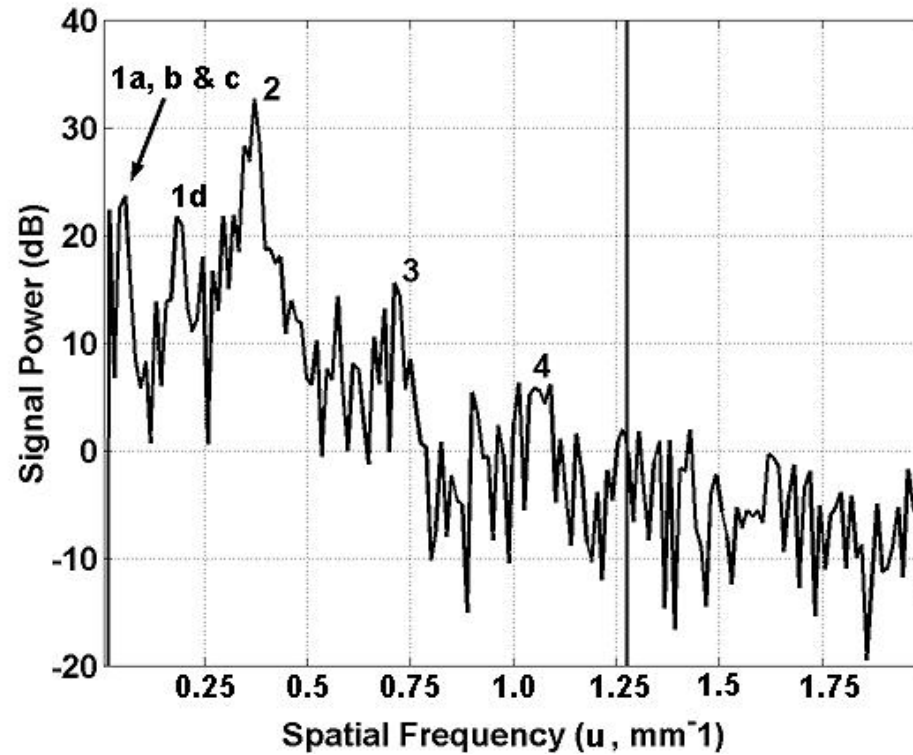
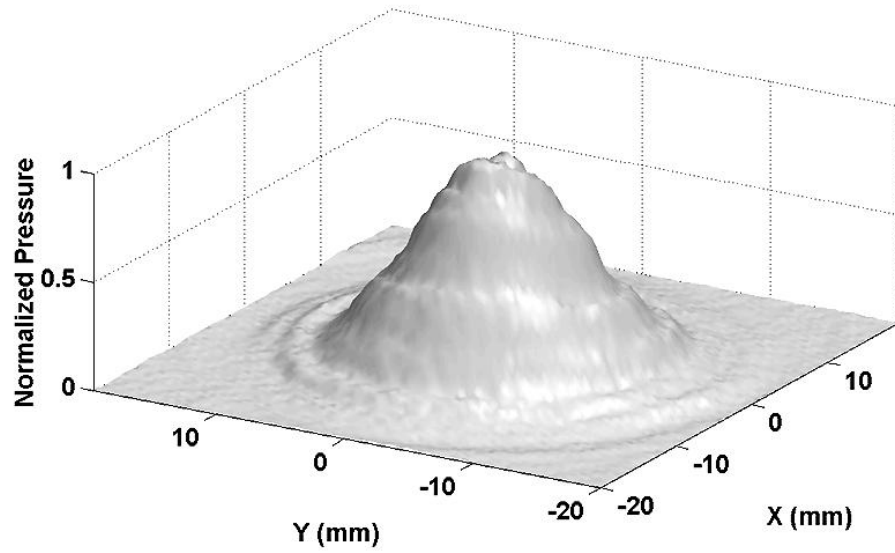
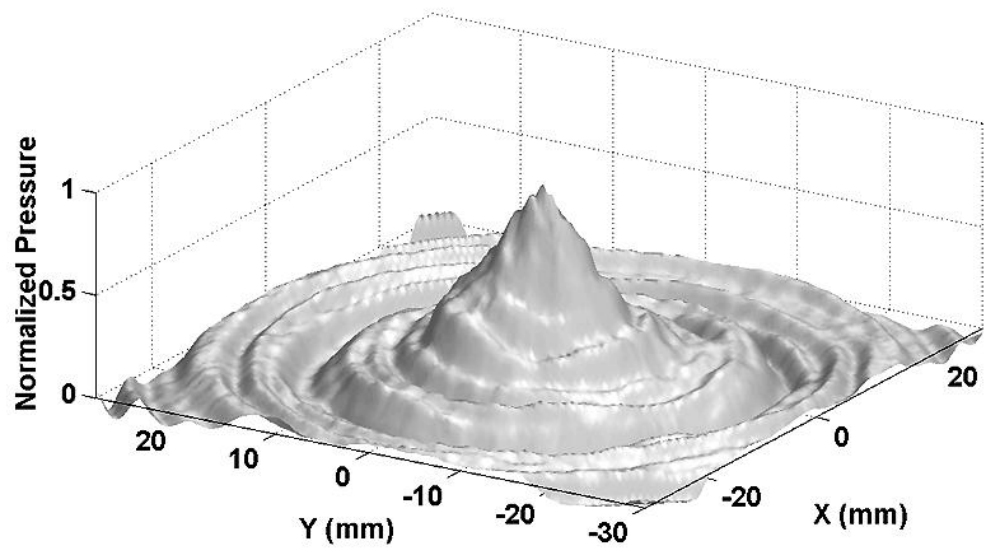


Figure 18. Spectral density of the experimentally measured standing wave pressure field of transducer II is shown for signals along the recorded axial centerline. Spatial frequency is defined in terms of $u = 1/\lambda$. The peaks labelled (1) are a consequence of chamber harmonic axial resonances associated with the distance between the transducer surface and the water/air surface. Peaks (2) and (4) correspond to transducer fundamental and third harmonic resonances. Peak (3) corresponds to a nonlinear second harmonic resonance. The vertical line seen at $u = 1.28$ denotes the -3 dB corner frequency of the 1.9 MHz low pass filter.



(a)



(b)

Figure 19. Lateral profile of the experimentally measured standing wave pressure field for transducers (a) I and (b) II. Profiles were taken (a) 36.9 mm and (b) 45.2 mm above the radiators.

within ± 2 dB. These predictions appear valid within the limits of accuracy of the hydrophone calibration and measurements of the crystal properties. The non-linearities seen in Figure 15(a) might be expected considering that the transducer power rating was exceeded.

Referring to Figure 17 and Table 10, it is clear this is not the case. Spectral analysis of the three chamber-transducer systems clearly shows the existence of interference by chamber resonance waves, as seen as higher and sub-harmonic components in the spectrum (Figure 18). Nevertheless, high drive voltages were necessary to achieve pressures required to levitate most particles. Noting in Figure 19 the significant change in the lateral topography, it is conceivable lateral resonances in the chamber also exist. The axial and lateral resonances present likely also contributed to the deviations seen in Figure 17, since second harmonic peaks indicate finite-amplitude propagation and suggest linearity is violated.

Direct coupling of the transducer to the chamber was minimized by the chamber design (see Section 4). Since chamber resonances were found some coupling must still be present, either directly between the transducer and the chamber or indirectly through the water medium. Indirect coupling may occur because although plexiglas is a good material for the application, its reflection coefficient is 0.389.⁵³ Hence acoustic energy is transmitted into the plexiglas and re-emitted at the resonant frequencies of the chamber. In the axial direction, there is strong energy re-emission from the plexiglas base at frequencies corresponding to standing wave generation at the fundamental, third and higher order harmonics ($n\lambda_c/2 = \text{water height}$ where λ_c

is the chamber fundamental mode wavelength and $n = 1, 3, 5, 7, \dots$). Solutions of the Helmholtz equation, $\nabla^2 p(z, r) + k^2 p(z, r) = 0$, for the current chamber geometry (i.e. $k^2 = k_z^2 + k_r^2$) are normal modes of the chamber.^{88,89,58(ch.4, p.93)} As an example, for transducer II at a water height of 54.6 mm, the three lowest order axial resonances exist at 13.6, 40.9 and 68.2 kHz (or 0.01, 0.03 and 0.05 mm⁻¹ spatial frequencies, visually seen in Figure 18 as peaks 1a, b and c).

Qualitative testing of the existence of the chamber resonances was achieved by lining the chamber walls and base with silicon foam rubber. From hydrophone measurements, addition of the lining lowered the chamber resonances by approximately 10 dB. If Equation (29) is to accurately predict the measured chamber pressure field, multiple reflections need to be eliminated from the chamber by using a highly attenuating medium and by lining the chamber with a high-scattering surface and absorbing material.

It was also observed that measurement of the pressure field using a 0.4 mm polymer needle hydrophone appears to only minimally disturb the field. Referring to Figures 16 and 17, the predicted and measured pressure fields were in phase. The slight phase differences detected are likely due to volume displacement of the water as the hydrophone and hydrophone holder are submerged in the medium. Significant planar distortion within two wavelengths from the water/air surface was also observed, and for this reason the pressure field mapping was performed at least 5 mm from the water/air surface. Other artifacts exist (in Figure 17, the spike at $z = 33$ mm and the notch at $z = 5$ mm), are attributable to the hydrophone holder,

and can be remedied by using more stealthy hydrophone holder designs.

Finally, the “burn” test of transducer I demonstrated that the manufacturer ratings are conservative, and with care performance specifications may be exceeded for short durations. The power rating is a consequence of heating that can depole the crystal and is mainly due to heating of the tuning electronics which are typically housed internally as part of the transducer assembly. Transducer II avoided this problem: its housing is designed for maximal heat transfer away from the crystal, and utilizes a tuning electronics box external from the transducer housing.

Putting this section into context, the chamber-transducer system can be modelled using Equation (29). But the pressure model will only be accurate as long as non-linear effects and chamber resonances are negligible. Unfortunately, in order to levitate most particles of interest, the pressures are high enough that these other resonances are significant, and will require the use of sound-absorbing materials and attenuating medium to correct.

6. THE FORCE MODEL

6.1. Method

Recalling Equation (33), the primary radiation force is a function of the gradient of the time-averaged, squared standing wave pressure field. Using this equation a comprehensive force model was developed to predict the axial and lateral primary radiation, buoyancy and net forces, and the minimum trap pressures, and was then extended to visually predict the locations of particle column formation. Input variables for the model are the particle size and acoustic properties, medium acoustic properties, transducer crystal properties and drive voltage, and a predicted or experimentally measured pressure field. The model is valid under all of the assumptions for Equation (33) in Section 2. Specifically, it can be used with small spherical gas-phase, solid and liquid particles where thermal and viscous effects are negligible, and is valid for many standing wave pressure fields that can be predicted with Field II or experimentally measured.

Equation (33) was demonstrated to be analytically equivalent to other forms of the primary radiation force equation, namely Equation (15) in the 1D case, and Equations (34), (41), and (42) in the 2D case. These equations were independently developed during the Cold War years; Equation (15) was developed in the Western world,⁵⁹ and Equations (34) and (41) were developed in Russia.⁷² Because of their independent development, and because many researchers have experimentally validated these equations they are considered gold standards which can be used to test the force model against.

In this section the intent is to demonstrate numerical equivalence for solid, liquid, and gas-phase particles, and red blood cells using four pressure field topographies: A) a plane standing wave, B) a non-diverging plane standing wave with a lateral beam profile corresponding to the fundamental lateral mode of a cylinder, C) a non-diverging plane piston standing wave, and D) a diverging plane piston standing wave (developed from Field II and represented mathematically by Equations (29) and (48). For all pressure fields, the operating frequency was 568 kHz, the crystal properties of transducer II were used, and a medium of deionized, degassed water at 22.5 °C was assumed.

6.2. Results

The simulation data was used to qualitatively test the force model, Equation (33), against

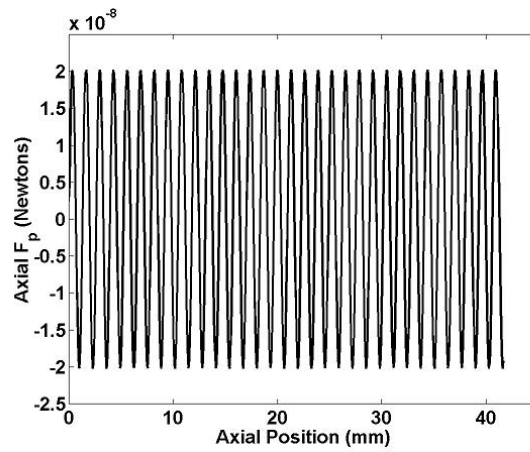
Yosioka and Kawasima's solution, Equation (15), and against Gor'kov's solution, Equations (34) and (41), using pressure fields A through D for small diameter gas-phase particles (9.0 μm diameter isobutane encapsulated microbubbles), solid particles (19.0 μm diameter polystyrene), liquids (glycerine) and red blood cells.

The axial profiles for the forces for pressure field A and D using 9.0 μm diameter isobutane encapsulated microbubbles are shown in Figure 20. It was found the axial profiles for the forces for pressure field B and C were similar to A and D respectively. The lateral profiles of the forces for pressure field B, C and D using 9.0 μm diameter isobutane encapsulated microbubbles are shown in Figure 21. Pressure field A was not used in calculating the lateral profiles since it represents a plane standing wave

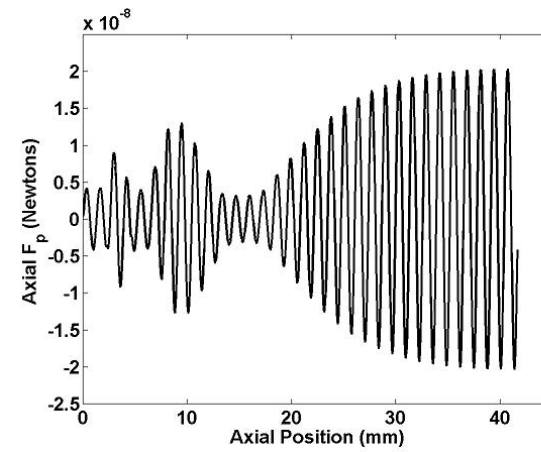
with constant pressure amplitude laterally. These results were typical for all particles tested, except for differences in the force magnitudes, which depend on the particle size and acoustic properties.

Upon testing of the force model for liquids (glycerine) and red blood cells, calculations based on the Gor'kov formula, Equation (41), results in the axial direction in a large sinusoidal impulse response at the zero crossings of the radiation force. In the lateral direction, the radiation force predicted by Equation (41) is similar in form to the model but smaller in magnitude. Analysis of the terms in Equation (41) revealed the difference was associated with the kinetic energy density term $\langle \text{KE} \rangle = 3\rho \langle v^2(z, r, t) \rangle / 4$. By setting $\langle \text{KE} \rangle = - \langle \text{PE} \rangle$, valid for small oscillating particles, we obtained Equation (42), and the difference was eliminated.

After qualitative verification of the topography of the force model, Equation (33), with the Yosioka and Kawasima and Gor'kov formulas, Equations (15), (34), (41) and (42), the predicted force magnitudes were compared for all four particle types at the location of the maximum pressure within pressure fields A, B, C and D (see Tables 11 and 12). Using Equations (15), (33), (34) and (42), and the properties of transducers I, II, and III, the maximum magnitude of the axial and lateral primary radiation forces and the buoyancy force was calculated for some of the particles listed in Table 6 in Section 4. Equation (41) was not used for quantitative comparison because it is defined in terms of the kinetic energy density. Results of these calculations are shown in Table 13. The minimum trap pressure, location of particle trapping and particle column widths was also predicted, as shown in Table 14.



(a)



(b)

Figure 20. Plot of predicted axial forces on 9.0 micron diameter isobutane encapsulated microbubbles in pressure fields (a) A and (b) D. Predictions are along the axial centerline. Axial position in the figure is relative to the transducer surface.

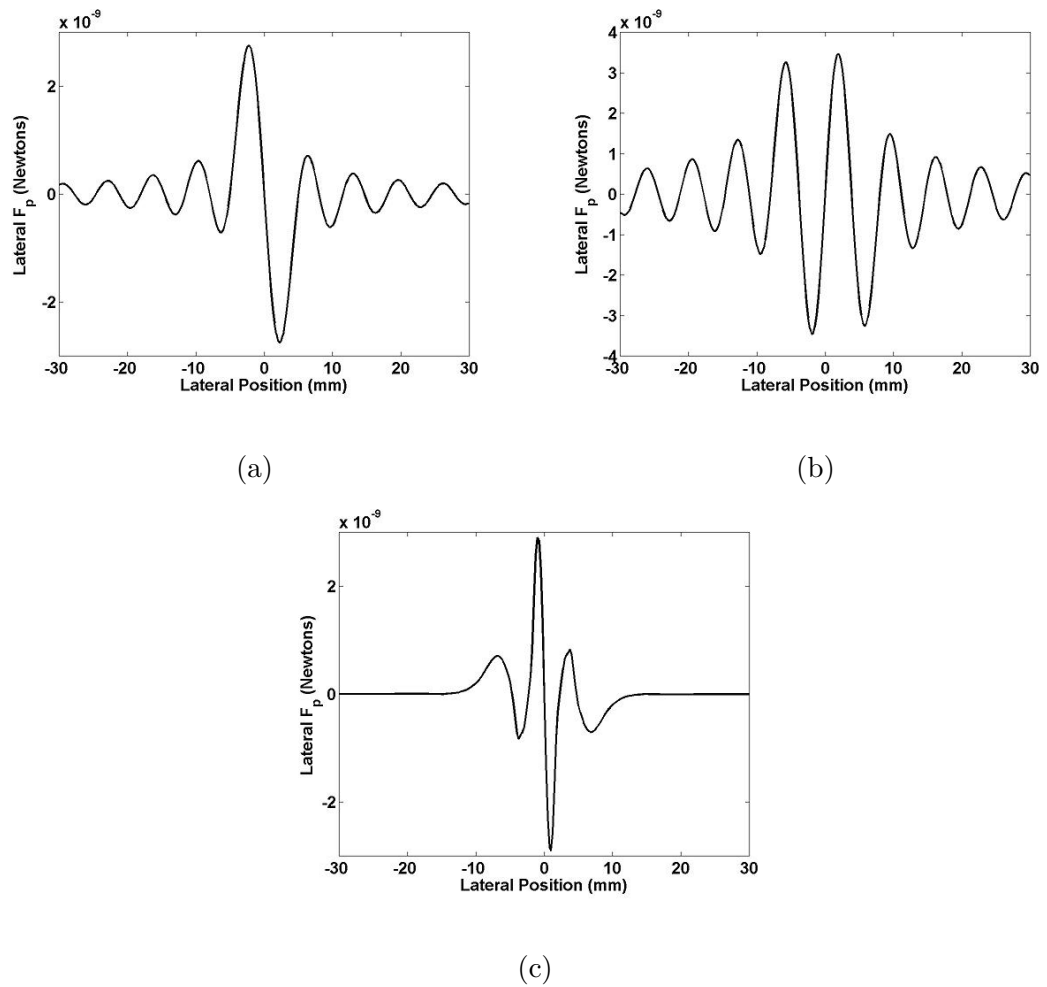


Figure 21. Plot of predicted lateral forces on 9.0 micron diameter isobutane microbubbles in pressure fields (a) B, (b) C and (c) D. Predictions are at an axial position corresponding to the peak pressure in the chamber. Lateral position in the figure is relative to the axial centerline.

Table 11. Axial Force Predictions

Particle	Pressure Field ^a	Axial Force ^a				
		Model (N)	Yosioka/Kawasima (N)	Deviation (%)	Gor'kov (N)	Deviation (%)
isobutane		$\times 10^{-8}$	$\times 10^{-8}$		$\times 10^{-8}$	
	A	2.022	2.037	0.74	2.026	0.19
	B	2.022	2.037	0.74	2.026	0.19
	C	2.022	2.037	0.74	2.026	0.19
	D	2.034	2.041	0.34	2.038	0.20
polystyrene		$\times 10^{-10}$	$\times 10^{-10}$		$\times 10^{-10}$	
	A	1.098	1.106	0.70	1.098	0.00
	B	1.098	1.106	0.70	1.098	0.00
	C	1.098	1.106	0.70	1.098	0.00
	D	1.105	1.108	0.34	1.105	0.00
glycerine		$\times 10^{-9}$	$\times 10^{-9}$		$\times 10^{-9}$	
	B	2.196	2.213	0.73	2.196	0.00
	D	2.185	2.193	0.34	2.185	0.00
red blood cells		$\times 10^{-13}$	$\times 10^{-13}$		$\times 10^{-13}$	
	B	3.081	3.104	0.72	3.081	0.00
	D	3.100	3.110	0.32	3.100	0.00

a - forces calculated at regions of maximum pressure in the field

Table 12. Lateral Force Predictions

Particle	Pressure Field ^a	Lateral Force ^a		
		Model (N)	Gor'kov (N)	Deviation (%)
isobutane		$\times 10^{-9}$	$\times 10^{-9}$	
	A	0.000	0.000	0.00
	B	2.756	2.760	0.14
	C	3.460	3.466	0.17
	D	2.905	2.910	0.17
polystyrene		$\times 10^{-11}$	$\times 10^{-11}$	
	A	0.000	0.000	0.00
	B	1.496	1.496	0.00
	C	1.879	1.879	0.00
	D	1.578	1.578	0.00
glycerine		$\times 10^{-10}$	$\times 10^{-10}$	
	B	2.993	2.993	0.00
	D	3.120	3.120	0.00
red blood cells		$\times 10^{-14}$	$\times 10^{-14}$	
	B	4.199	4.199	0.00
	D	4.426	4.426	0.00

a - forces calculated at regions of maximum pressure in the field

Table 13. Force Predictions

Particle	Diameter (μm)	Transducer	Axial Force (N) ^a	Lateral Force (N) ^a	Buoyancy Force (N)
decafluorobutane	3.0	II	1.125×10^{-11}	1.606×10^{-12}	1.368×10^{-13}
air	35.0	I	1.884×10^{-6}	2.691×10^{-7}	2.194×10^{-10}
isobutane	9.0	II	1.859×10^{-8}	2.654×10^{-9}	3.248×10^{-12}
isobutane	40.0	II	8.757×10^{-6}	1.250×10^{-6}	2.852×10^{-10}
isopentane	30.0	II	2.469×10^{-6}	5.171×10^{-7}	1.196×10^{-10}
polystyrene	0.5	II	1.768×10^{-15}	3.695×10^{-16}	-3.371×10^{-17}
polystyrene	15.5	II	4.763×10^{-11}	9.978×10^{-12}	-9.101×10^{-13}
polystyrene	19.0	II	9.680×10^{-11}	2.028×10^{-12}	-1.850×10^{-12}
glycerine	50.0	II	1.915×10^{-9}	4.013×10^{-10}	-1.846×10^{-8}
red blood cells	4.0	III	1.630×10^{-13}	4.659×10^{-14}	-1.923×10^{-14}

a - forces calculated at regions of maximum pressure in the field

Table 14. Column Formation Predictions

Particle	Diameter (μm)	X	Minimum Trap Pressure (kPa)	Location of Trapping	Column Width ^a , $W =$ (W dB to W dB wide)
decafluorobutane	3.0	-7190	1.3	antinode	-22.2
air	35.0	-709	4.2	antinode	-42.2
isobutane	9.0	-411	5.2	antinode	-40.4
isobutane	40.0	-2205	2.2	antinode	-47.7
isopentane	30.0	-1542	2.7	antinode	-46.2
polystyrene	0.5	0.238	52.7	node	-20.2
polystyrene	15.5	0.238	52.7	node	-20.2
polystyrene	19.0	0.238	52.7	node	-20.2
glycerine	50.0	0.258	118.4	node	-13.2
red blood cells	4.0	0.072	105.3	node	-12.3

a - column width calculated at plane corresponding to region of maximum pressure in the field

For all the calculations in the tables, the drive voltage was arbitrarily chosen to be 31.62 volts peak, corresponding to a power dissipation of 10 Watts. This value in practice is beyond the manufacturer power ratings of transducers I and III, but is achievable for short durations according to the experimental data obtained in Section 5.

In Figures 22, 23, 24, and 25 the predicted column formations are shown for gas-phase, solid particles, liquids, and red blood cells using pressure field D.

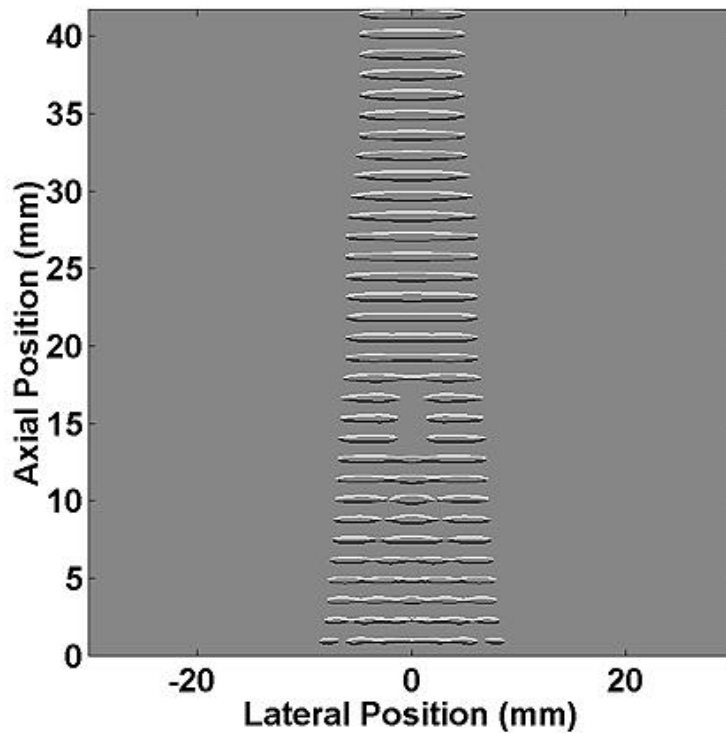
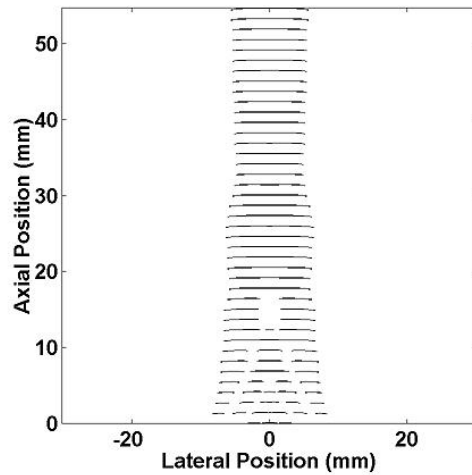
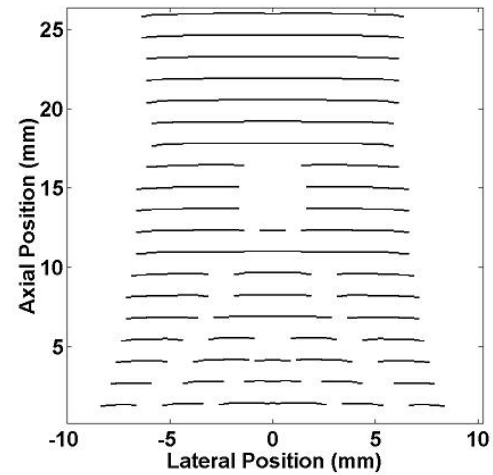


Figure 22. Column formation of 9.0 micron isobutane microbubbles predicted by the force model using transducer I. If prior to activation of the pressure field particles are located at positions denoted by the white lines, after activation of the field these particles will not change position. All other particles in the chamber will be pushed towards positions denoted by the black lines. Note the ring formation predicted 15 mm above the transducer surface. Drive voltage is 31.6 volts peak. Predicted particle minimum trap pressure is 5.2 kPa peak.

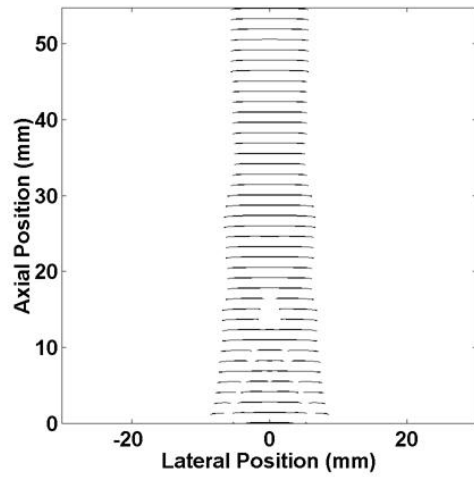


(a)

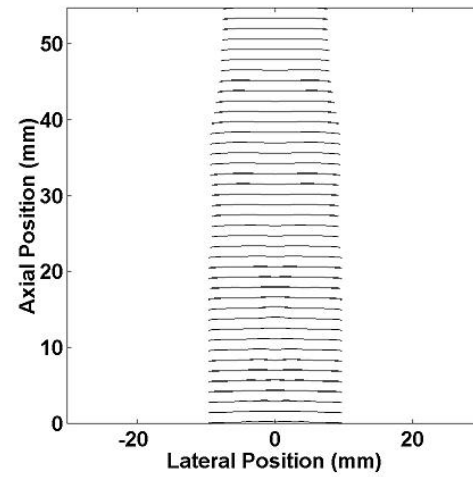


(b)

Figure 23. (a) Column formation of 19.0 micron polystyrene microspheres predicted by the force model using transducer II. Note the ring formation predicted 15 mm above the transducer surface. The ring formation is experimentally demonstrated in Section 7. Drive voltage is 16.9 volts peak-peak. Predicted minimum trap pressure is 52.7 kPa peak. (b) Zoom-in of the near field region. For clarity, in both images, the background has been changed to white and regions of low particle concentration (denoted by the white lines in Figure 22) are not shown. Only regions of high particle concentration (denoted by the black lines in Figure 22) are shown.



(a)



(b)

Figure 24. Column formation of glycerine predicted by the force model using transducer II. Drive voltages are (a) 19.7 and (b) 33.7 volts peak. Predicted minimum trap pressure is 118.4 kPa peak. Note by increasing the drive voltage the ring formation 15 mm above the transducer surface becomes column formation.

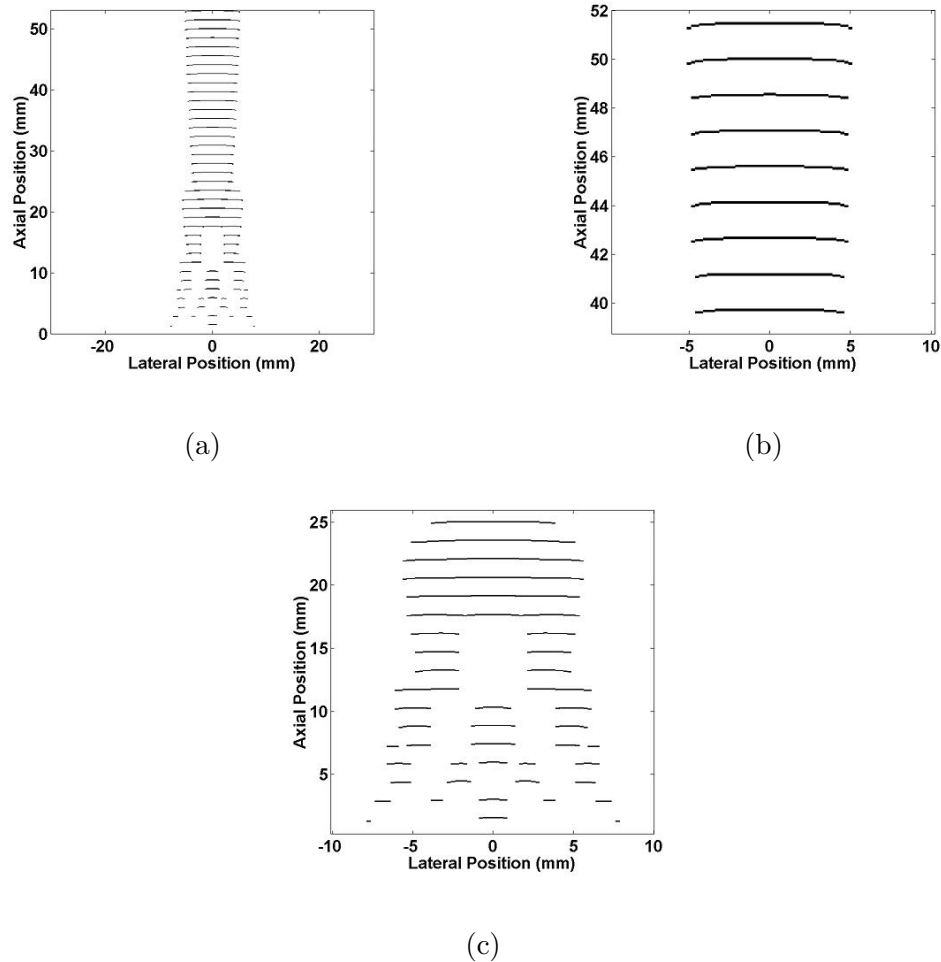


Figure 25. Column formation of red blood cells predicted by the force model using transducer III. Drive voltage is 18.7 volts peak. Predicted minimum trap pressure is 105.3 kPa peak. (b) Zoom-in of the far field region. (c) Zoom-in of the near field region. Notice the concentric ring formations in this region at $z < 15$ mm.

6.3. Discussion

Qualitative analysis has indicated the force model topography using a plane standing wave pressure field fully agrees with the topography calculated using the Yosioka and Kawasima formula. When non-planar standing wave pressure fields were used, qualitatively the force model topography fully agreed with the topography calculated using the Gor'kov formula, and also nearly matches the topography calculated using

the Yosioka and Kawasima formula. In the case of Gor'kov, when the kinetic energy density term $\langle KE \rangle$ is used, Equation (41), deviations in the force model topography will exist. Analysis of the kinetic energy density term in the Gor'kov formula shows these deviations are numerical errors introduced from second-derivative computations within the Matlab environment. The error is corrected by replacing the kinetic energy density term with the potential energy density term, Equation (42).

Analysis of Tables 11 and 12 shows that quantitative deviations between the force model and the Yosioka and Kawasima and Gor'kov formulas is acceptable ($< 1\%$). It turns out deviations between the model and the Yosioka and Kawasima formula are due to axial shifting in the plots. The Gor'kov formula and the model rely on the standing wave pressure field topography developed from a traveling wave folding operation, and are sensitive to changes in the axial resolution. In contrast, the Yosioka and Kawasima formula predefines the topography of the pressure field via a $\sin(2kz)$ term, so it is independent of the axial resolution. Contrary to expectations, the deviations between the force model and the Yosioka and Kawasima formula were smaller for pressure field D, the plane piston model. We would have expected the smallest deviations would have occurred for pressure field A, which is the pressure field model used to derive the Yosioka and Kawasima formula. We have no explanation for this except it may be due to the phase-shifting previously mentioned. A small deviation of 0.20% exists between the model and the Gor'kov formula for small diameter gas-phase particles, but for all other cases the model is in complete agreement with Gor'kov. Comparing Equation (33) with Equations (34) and (41), the

deviation represents inaccuracies in the Gor'kov formula because the particle size is not considered in f_1 and f_2 calculations. The accuracy of the model is only as good as the accuracy of the input variables, such as the particle and medium properties and transducer crystal properties. Determination of the accuracy of these values is beyond the scope of this research.

Analysis of Table 13 shows that for a given transducer, drive voltage and pressure field topography, the forces generated can vary from 10^{-15} to 10^{-6} Newtons. The lateral forces were typically 7, 4.7, and 3.5 times smaller than the axial forces for transducers I, II and III respectively. The differences in the lateral force: axial force ratio are mainly due to differences in the chamber water heights and transducer operating frequencies, leading to variations in the lateral beam profiles of the pressure field.

Analysis of Table 14 shows that gas-phase particles are most sensitive to the generated pressure field ($X > 100$), followed by liquid and solid particles ($X \approx 0.238$ to 0.258), with red blood cells the least sensitive ($X \approx 0.072$). In other words, X is an indicator of the acoustic transparency of a given particle. More transparent particles have lower values of X , and the radiation force will be weaker for the same pressure field. For a given transducer, drive voltage and pressure field topography that the radiation forces will be largest for the gas-phase particles and smallest for the red blood cells. It was also observed that gas-phase particles are relatively easy to trap, followed by solid and liquid particles, with red blood cells the most difficult to trap, and with consideration for the particle size is reasonably consistent with the minimum

trap pressures listed in the table. Finally, from the column width values listed in the table, it is seen that column formation for the gas-phase particles is easily visualized, and red blood cell column formation is more difficult to see. It is possible that the visual study of biological cells may be challenging without significant magnification, or higher particle concentrations, which in turn requires smaller volume chambers and sufficient depth-of-field for magnifying and photographing the levitating cells.

Analysis of the column formation pictures predicted by the force model shows that the topography of the pressure field does strongly influence the column structure. Observe that the model predicts the formation of rings, concentric rings and columns in the near field of the transducer, where the pressure topography is quite complex. The principle of ring formation is experimentally demonstrated in Section 7.

Referring to Figure 25 and Table 14, red blood cell column formation appears possible. Using transducer III at 3.5 Watts power dissipation (above the manufacturer rating of 0.125 Watts), the minimum trap pressure of 105.7 kPa peak can be met. However, the column will only be -7.6 dB to -7.6 dB wide relative to the axial centerline pressure so that visualization of these columns will be extremely difficult. Column formation is further complicated by the limited amount of time available it has to form the columns due to the transducer crystal heating. Also, acoustic streaming, rectified diffusion and cavitation effects will be significant at this pressure. For the glycerine experiments, where the minimum trap pressure was 118.4 kPa peak, the viscosity of glycerine substantially reduced the effects of these phenomena, but for red blood cells in normal saline no such mitigation exists. In other words, although the

operating principle of the current chamber design is sound, it will not work effectively for red blood cells. Modifications to the existing chamber design to allow camera visualization of the column formation, and to better combat acoustic streaming and cavitation, are discussed in Section 8. Alternatives to the standard chamber design are also mentioned discussed in Section 8.

7. LEVITATION EXPERIMENTS

7.1. Method

Within this section, physical evidence of the chamber operation is provided via levitation of gas-phase, solid particles and liquids listed in Table 6 of Section 4. The acoustic properties of most of these particles are known, so that using the force model, based on Equation (33), it was possible to predict the minimum trap pressures and compare these predictions to experimental measurements.

Details of the photography equipment and lighting used during the particle levitations has already been discussed in Section 4. Minimum trap pressure measurements were performed in the following manner. First, for each particle levitation drive voltage was set to a pressure value approximately 30% higher than the minimum trap pressure predicted by the force model (Table 14 in Section 6). Particle injection was performed using a syringe or micropipettor positioned 5 to 10 mm from the water/air surface. After column formation occurred, the drive voltage was lowered until the columns dissipated. Then the process was reversed, starting with lower voltages and slowly increasing until column formation re-occurred. The entire process was repeated 5 times to determine the minimum trap voltage, V_{mtp} . At this voltage, the column width was as close to a point as visually observable (note in all cases for the photographs the drive voltage $> V_{mtp}$). Once V_{mtp} was established, the chamber was cleaned and refilled. Without changing the electronic settings, the 0.4 mm diameter needle hydrophone was introduced into the chamber using the Velmex XYZ Unislide positioner at the center of the column formation, and the pressure was measured.

Because P_{mtp} from V_{mtp} could not be calculated using Equation (48), the minimum trap pressure P_{mtp} was determined from this pressure measurement.

P_{mtp} could not be established in the chamber during particle actual levitation because the particles tended to migrate and obscure the hydrophone tip, reducing signal. The particle migration was due to secondary radiation forces generated between the hydrophone and the particles. Because the pressure measurement is performed in a particulate-free medium, it is expected the measurements will be higher than actual pressures when particles are present. However, at the low particle concentrations, the error introduced is minimal.

7.2. Results

Visual confirmation of the standing wave pressure field was first achieved with transducer I utilizing 3 micron diameter decafluorobutane encapsulated microbubbles. Although achievable, the column formations were not clear enough for photographic presentation. Hence, all subsequent levitation experiments were performed using transducer II.

The first levitation experiment using transducer II utilized unencapsulated air bubbles introduced into the standing wave pressure field via micropipettor cavitation (Figure 26). Based on predictions from the force model, the average size of the air bubbles in this photograph appear to be approximately $35 \mu\text{m}$ in diameter. In this figure, it appears the bubbles are forming aggregates within each column. Bubbles also tended to rapidly jump within the columns in rhythmic patterns. This was predicted by secondary radiation force theory (Section 3). It was quick enough that

at fast camera shutter speeds blurring of individual particles occurred, so each bubble photographs as a small horizontal white line (streak).

Levitation of 30.0 μm diameter isopentane encapsulated microbubbles was also achieved but the photographs were not clear enough for presentation. The isopentane is dry-packaged and contains a high concentration of calcium particulate. Separation of the calcium from the isopentane microparticles using centrifugation was less than ideal, so that introduction of isopentane into the chamber also clouded the chamber milky-white. The final gas-phase particle levitations involved 9 μm diameter isobutane encapsulated microbubbles in the presence of unencapsulated air bubbles using transducers I and II (Figure 27).

For solid particles, 19.0 μm diameter polystyrene microspheres (Figure 28) were levitated. Polystyrene microspheres of 0.5 μm diameter could not be levitated. These particles are of a size such that acoustic streaming, thermal convection and Brownian motion/diffusion forces are no longer negligible. Polystyrene microspheres (15.5 μm diameter) were levitated but the columns were not clear enough to be photographed, due to photobleaching of the fluorescent particles. Cornstarch was also levitated and the column formation was very similar to polystyrene (Figure 29). To verify if mixed phase particulate suspensions could be levitated simultaneously and separated, 19.0 μm diameter polystyrene and 9.0 μm diameter isobutane microbubbles were injected into the field, shown in Figure 30. As seen, separation occurs as predicted based on the particle acoustic properties. Force model predictions of ring formation in the near field region (predicted in Section 6) were confirmed in a spectacular

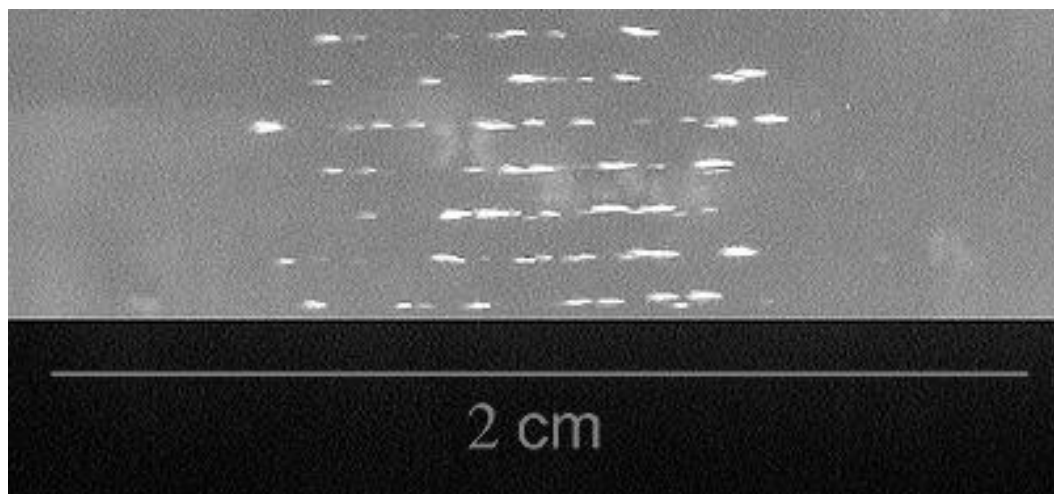


Figure 26. Column formation of 35 micron diameter unencapsulated air bubbles using transducer II. Drive voltage was at 19.7 volts peak-peak.

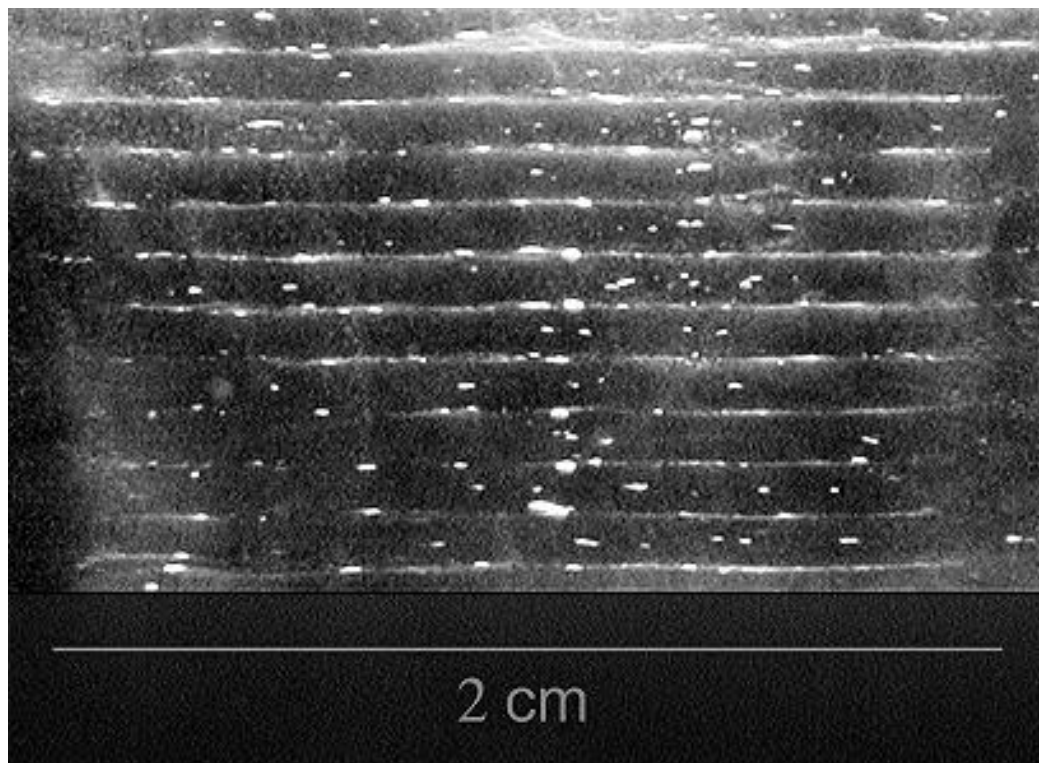


Figure 27. Column formation of 9.0 micron diameter isobutane encapsulated microbubbles using transducer II. Drive voltage was at 16.9 volts peak-peak. Bright spots are unencapsulated air bubbles.

manner via injection of $19.0\ \mu\text{m}$ polystyrene microspheres into this region, as shown in Figure 31. The ring formation demonstrate in a novel way the complexity of the pressure field in the near field region.

Levitation of liquids was examined using food coloring dye and glycerine contrasted with a few drops of food coloring dye (Figures 32 and 33). Food coloring levitation is particularly tricky to photograph, since it is highly miscible in water and disperses within seconds after column formation. On the other hand, although glycerine is miscible it is also quite viscous, so that columns formed were stable for 1 to 2 minutes. Further experiments using glycerine were performed to test column width predictions by the force model (Figure 34). As expected, column dimensions conform to the lateral profile of the pressure field down to the threshold pressure P_{mtp} .

In all cases, location of column formation for these particles was confirmed to occur in accordance with predictions from the force model. Particles levitated within a few seconds of applying the drive voltage to the transducer.

Minimum trap pressure measurements for all of these particles are compared to force model predictions in Table 15.

7.3. Discussion

Column formation was achievable for all particles except the $0.5\ \mu\text{m}$ diameter polystyrene microspheres. For these particles, acoustic streaming and thermal convection were substantial enough to prevent column formation. Also, Brownian diffusion forces and thermal damping effects can no longer be neglected since $R_o < 1\ \mu\text{m}$.

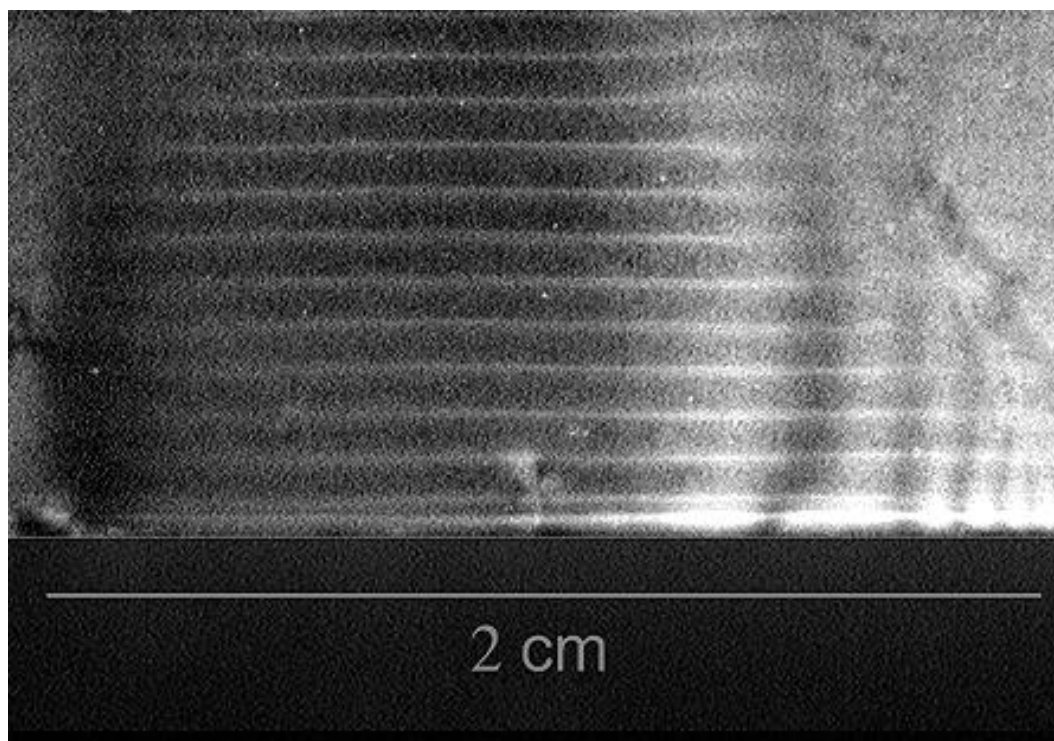


Figure 28. Column formation of 19.0 micron polystyrene microspheres using transducer II. Drive voltage was at 14.1 volts peak-peak.

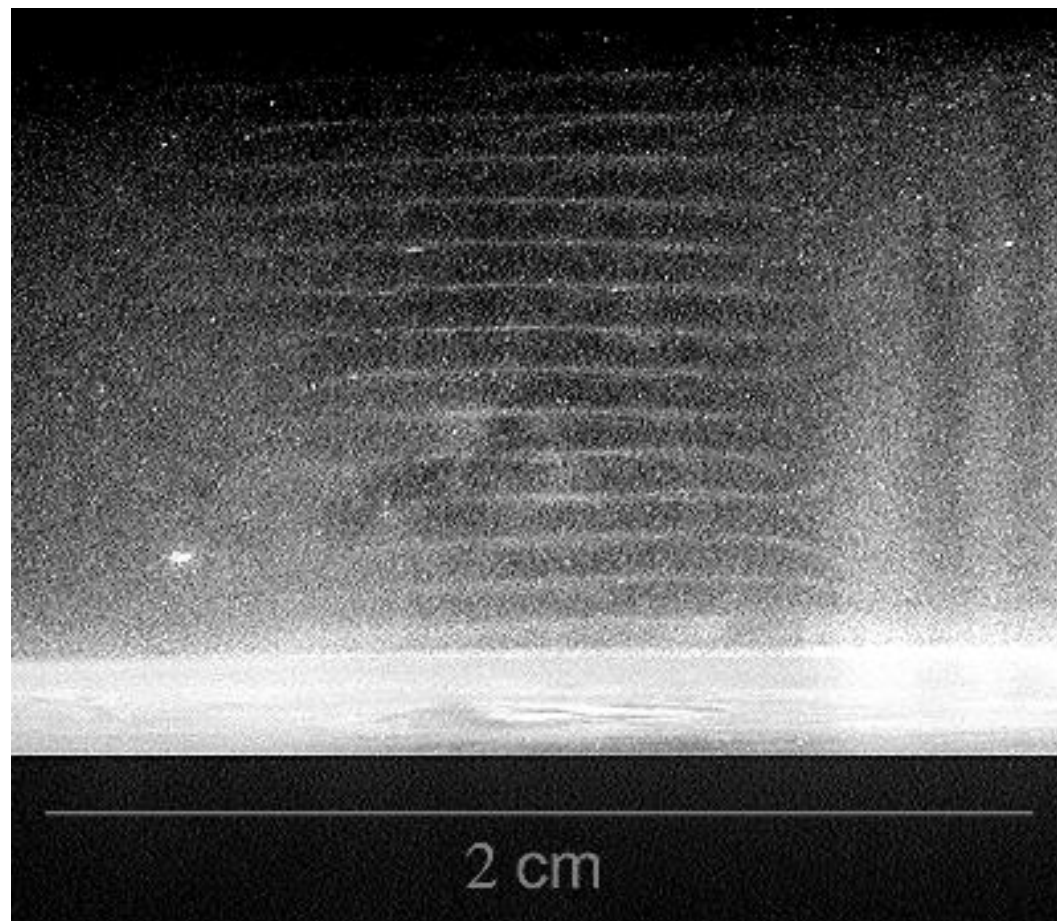


Figure 29. Column formation of cornstarch using transducer II. Drive voltage was at 22.5 volts peak-peak.

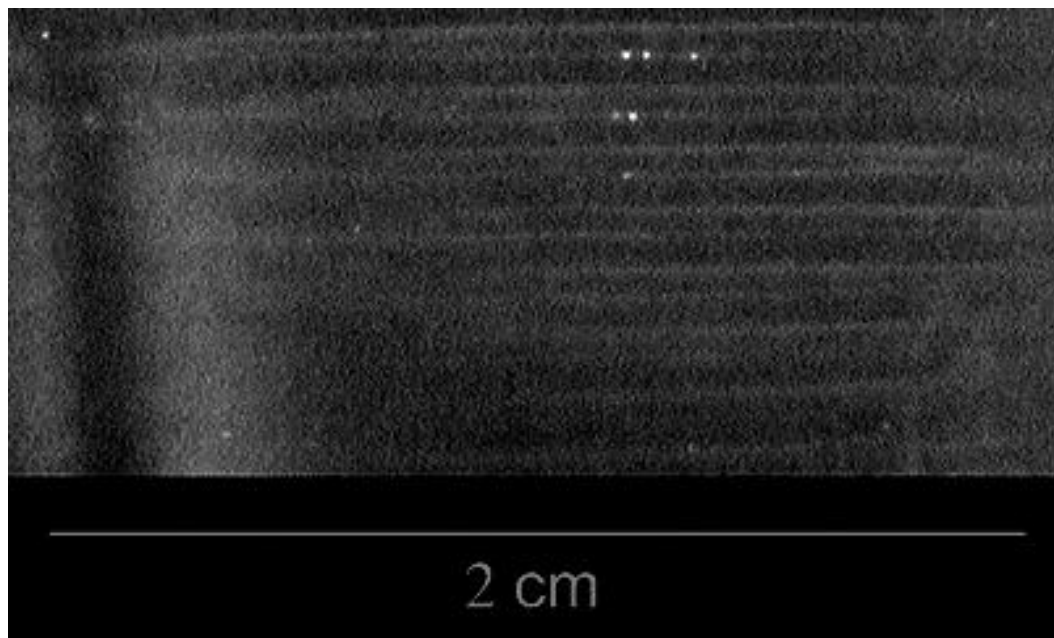


Figure 30. Column formation of approximately 9.0 micron diameter isobutane encapsulated microbubbles and 19.0 micron polystyrene microspheres using transducer II. Drive voltage was at 11.2 volts peak-peak.

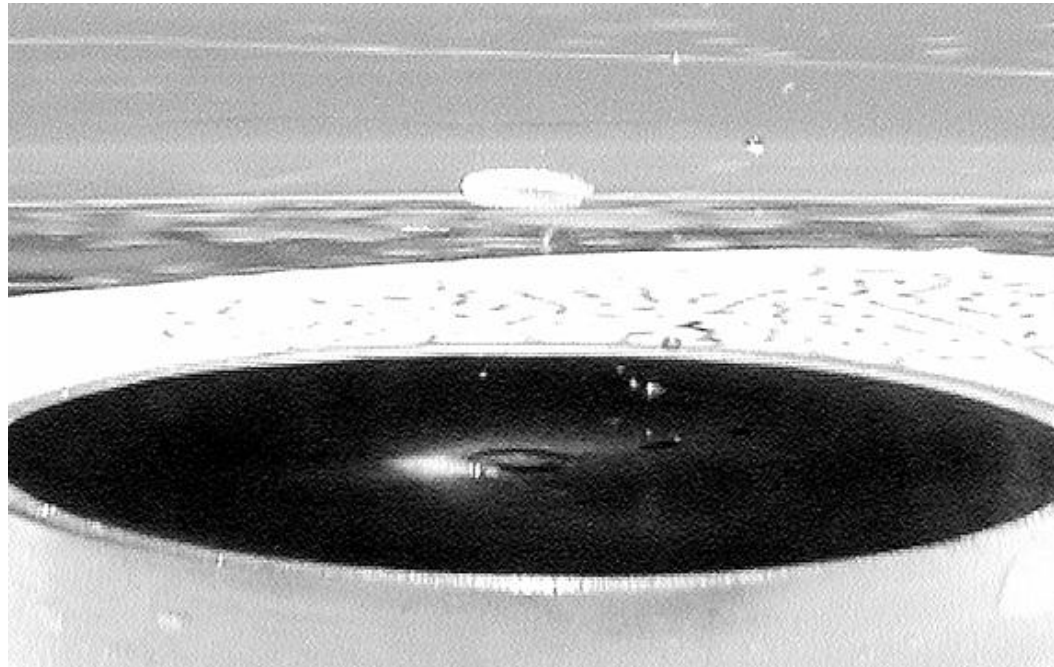


Figure 31. Ring formation of 19.0 micron polystyrene microspheres using transducer II. The ring was located 15 mm above the transducer face and is approximately 3 mm in diameter. A shadow of the ring is seen on the transducer surface. Drive voltage was at 16.9 volts peak-peak.



Figure 32. Column formation of food coloring dye using transducer II. Drive voltage was at 22.5 volts peak-peak.

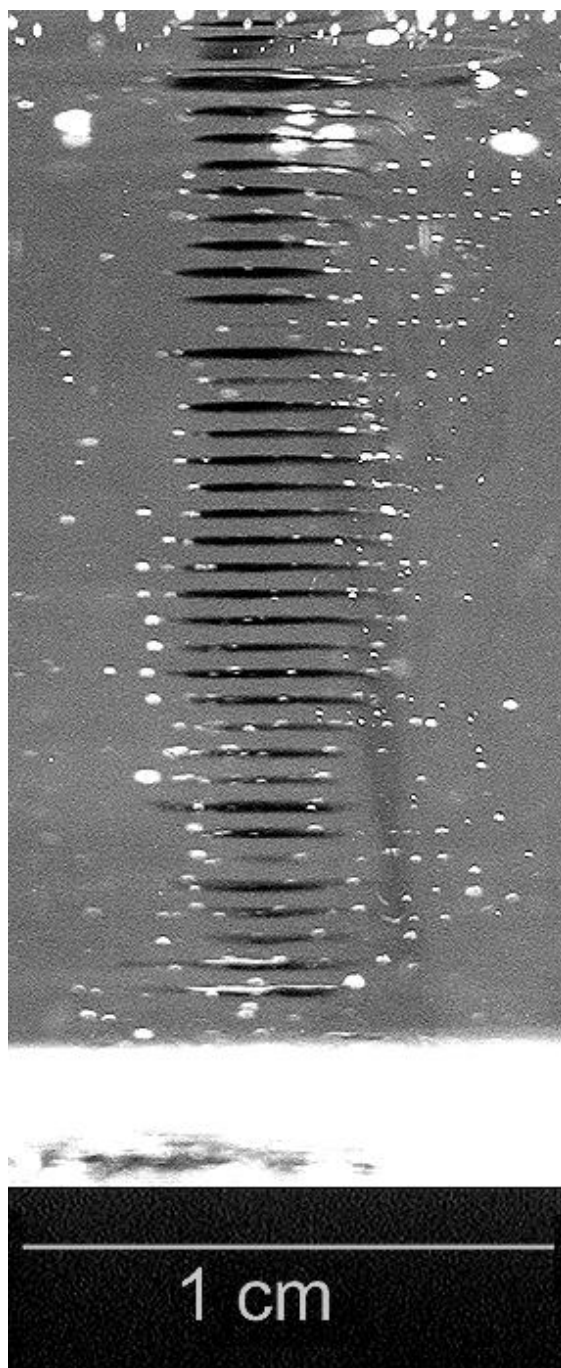
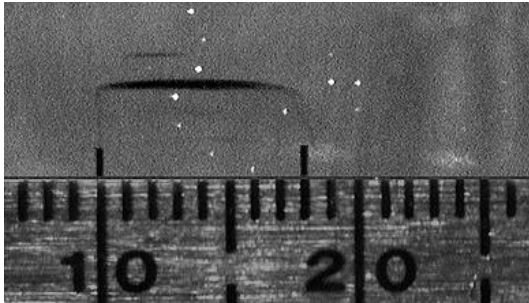
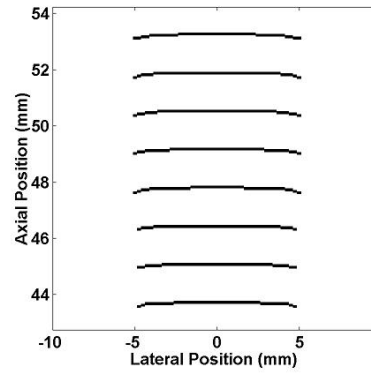


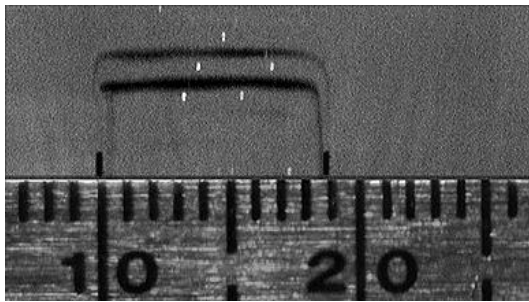
Figure 33. Column formation of glycerine (contrasted with a few drops of food coloring dye) using a transducer II. Drive voltage was at 22.5 volts peak-peak.



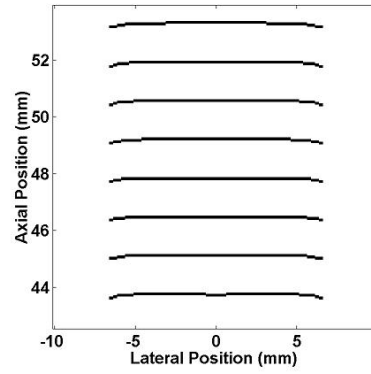
(a) 19.7 volts peak/ 211.6 kPa/ 8.0 mm



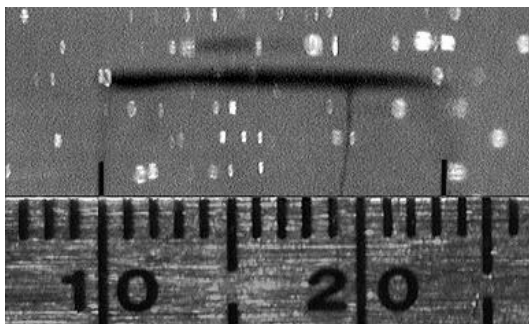
(b) 211.6 kPa/ 10.5 mm



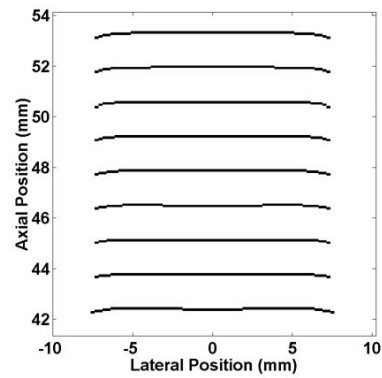
(c) 28.1 volts peak/ 307.9 kPa/ 9.0 mm



(d) 307.9 kPa/ 13.0 mm



(e) 33.7 volts peak/ 360.1 kPa/ 13.5 mm



(f) 360.1 kPa/ 15.0 mm

Figure 34. Column formation of glycerine (contrasted with a few drops of food coloring dye) using transducer II. At left are photographs of the measured column widths located 50 mm from the transducer surface. At right are figures of the column widths predicted by the force model In (e), the 3D nature of the column formation is revealed by the glycerine 'falling' off the column edge at 19.5 mm.

Table 15. Measured versus Predicted Minimum Trap Pressures

Particle	Diameter (μm)	Transducer Used	Minimum Trap Pressure (kPa)		Error from Measured (%)
			Measured	Predicted	
decafluorobutane	3.0	I	1.6	1.3	18.8
air ^a	35.0	II	4.8	4.2	12.5
isobutane	9.0	II	5.9	5.2	11.9
isobutane	40.0	II	2.4	2.2	8.3
isopentane	30.0	II	2.9	2.7	6.9
polystyrene	0.5	II	N/A ^a	52.7	N/A ^a
polystyrene	15.5	II	81.1	52.7	35.0
polystyrene	19.0	II	52.9	52.7	0.4
cornstarch	N/A	II	108.9	N/A ^b	N/A ^b
glycerine	N/A	II	119.5	118.4	9.2
food coloring dye	N/A	II	76.9	N/A ^b	N/A ^b

a - particle could not be levitated due to acoustic streaming and thermal convection.

b - minimum trap pressures could not be predicted because

a - the particle acoustic properties are unknown.

For most photographs, the presence of unencapsulated air bubbles could not be avoided. This tended to confuse results, since air bubbles are found everywhere in the pressure field, including at the pressure nodes and antinodes. Since these bubbles are unencapsulated their diameters are not controlled, so in accordance with theory they could be located at pressure nodes or antinodes depending on their size. In some cases the bubbles are far enough from the axial centerline that they are relatively uninfluenced by the primary radiation force, and in other cases the secondary radiation forces strongly influenced the microbubble location. The secondary radiation forces between gas bubbles and solid microspheres might also affect the location of solid microspheres.

Food coloring column formation has been previously reported.³⁶ The helical pattern seen in the photograph are of interest and are probably a consequence of fluid motion introduced during injection of the food coloring. Azimuthal rotating modes have been previously reported,³⁷ but in that case strong chamber resonances were present.

The results of the column width experiments (Figure 34) are encouraging. As drive voltage increased, chamber pressures increased and column widths increased. However, the measured column widths do not agree with predictions. Some inaccuracy between prediction and measurement is expected because of inaccuracy in the hydrophone calibration. Since the predictions use the pressure field model, it is probable some of the differences between predicted and measured column widths are in part due to pressure effects not directly related to the transducer (i.e. indirect

coupling of the transducer to the chamber which induced chamber resonances). Referring to Section 5, spectral peaks directly attributable to the chamber resonances do not appear to be linearly proportional to the transducer drive voltage (i.e. like the second harmonic transducer resonances, the indirect coupling is also probably nonlinear). It can be concluded from this that in order to guarantee the accuracy of the force model with the current chamber design, the pressure field needs to be accurately mapped at every drive voltage. This is an impractical solution, and points to the need for a chamber design which entirely eliminates chamber resonance effects and for a pressure model that considers non-linear phenomena.

Referring to Table 15, predicted and measured minimum trap pressures are within 10% with two exceptions. For the decafluorobutane microbubbles, the error may be because the pressures are quite low and the particle size was sufficiently small that visualization was difficult. For the 15.5 μm diameter polystyrene microspheres, these particles have a fluorescent coating and are also doped with 10% divinyl benzoate, whereas the acoustic properties used for the predictions assumed the microspheres were 100% pure polystyrene. For the remainder of the particles, less than 10% error is acceptable considering the difficulty in visualizing cell-sized particulate column formation near to the width of a single point within a large chamber with depth-of-field 2.5 cm.

8. FUTURE RESEARCH

From the material presented, future research on this topic may be broken into three parts, each part referring to changes to the pressure model, force model and chamber.

8.1. Prediction of the Pressure Field

Based on the results of Section 5, further work is necessary to obtain closer agreement between the measured and predicted pressure fields. In order to minimize chamber resonances that might perturb the sound field, there are two courses of action available. As a first possibility, materials can be chosen so that energy is not transmitted into the walls and base of the acoustic levitation chamber (i.e. perfect reflector). Alternatively, multiple reflections between the water/air surface and the chamber base and walls can be eliminated. The walls and base can be completely lined with sound absorbing materials such as silicon foam rubber, and use a high attenuation fluid medium. The pressure model can be modified to consider medium attenuation via using Field II.

Another alternative is to use the chamber resonances. The chamber geometry can be designed to produce standing waves by efficiently mechanically coupling the transducer to the chamber. The pressure model would not be based on a plane piston solution, but rather would be a solution to the Helmholtz equation. A disadvantage of this alternative is similar to the problem with the Field II calculations. Solutions to the Helmholtz equations only provide information on the topography of the pressure field. The true pressure magnitudes in the chamber can only be predicted by knowing

the mechanical coupling coefficient between transducer and chamber, the material properties of the chamber base and walls, and an equation which can relate the properties to the Helmholtz solution.³⁴⁻³⁸

8.2. Extension of the Force Model

Currently only the primary radiation force and buoyancy force are considered in the force model. The model may be improved by addition of any of the other forces discussed in Section 3, but in particular the effects of secondary radiation forces. Also, for future work with biologic cells, viscous dissipation must be considered and shape correction factors introduced to account for the cells of non-spherical geometry.

With these changes, the force model can then be extended with small, spherical particles with biologically active coatings (i.e. molecular bonds), such that the predicted net particle force has an adhesive bond force component. Similar to the method for calculation of the minimum trap pressure (Section 2), a relation between the chamber pressure and particle molecular bond rupture strength may be obtained.

8.3. Chamber Redesign

The next group of levitation experiments should be specifically aimed towards biologic materials. To achieve this aim, several design changes to the chamber will need to be made. Considering the pressures predicted by the force model to levitate red blood cells is 105.3 kPa, cavitation, rectified diffusion, and acoustic streaming will require careful management. Static pressurization of the chamber may be necessary to

prevent rectified diffusion and subsequent cavitation effects, although the pressurization will limit the capability to spatially map the pressure field. Acoustic streaming can still be handled by use of low attenuation phantoms, acoustically transparent film, and/or a high viscosity medium. Since the magnitude of large-scale Quartz wind streaming is proportional to the particle mean free path length, reduction of the chamber height may minimize this problem. Photography and illumination of the chamber and particles has been troublesome with the current chamber design due to the depth-of-field and large volume of the chamber, so reduction of the chamber dimensions would also prove beneficial.

Based on the knowledge gained from this linear wave propagation approach, and provided non-linear effects can be minimized, the chamber can be scaled down in size and the frequency scaled up to achieve similar results in a microchamber. If the cylindrical chamber geometry in all aspects was reduced by a factor of 6, it would be of 1 cm radius by 1 cm height, and uses a 3 mm diameter transducer operating at 3 MHz. The new chamber volume will be less than 20 ml (as compared to 640 ml). At the higher operating frequency, the distance between particle columns will be reduced from 1.49 to 0.25 mm, so observation of column widths is improved but observation of individual columns will be difficult.

Staying within power ratings of the transducer will be a challenge. A crystal with a high electrical-mechanical coupling coefficient k_{33} and material figure of merit M_o , such as PZT-4, will be required. By using the reduced chamber geometry just described, from Equation (15) increasing by a factor of 6 to an operating frequency

of 3 MHz will allow a reduction of pressure amplitudes by a factor of $\sqrt{6}$. From Equation (48), the drive voltage will also be reduced by $\sqrt{6}$ and power dissipation will therefore be reduced by 6. Further improvements can be made by utilizing duty factors between 0.4 and 1. At a pressure of 150 kPa, sufficient for levitation of red blood cells in the reduced chamber geometry, power dissipation of the transducer at duty factor 0.4 would be approximately 0.150 Watts, near the typical manufacturer ratings of 0.125 Watts.

The transducer power ratings and medium properties are strongly dependent on the medium used. From Equation (27), any means used to minimize the density difference between the medium and red blood cells, $\rho - \rho_o$, will allow column formations at lower pressures, so that manufacturer ratings will never be exceeded, even at duty factor 1.0. Reduction in required levitation pressures also means acoustic streaming, rectified diffusion and cavitation will be less significant problems, so that perhaps static pressurization of the chamber may be unnecessary.

There is a medium called Ficoll-400 which is used extensively by biologists to simulate physiologic conditions. It comes in a powder and can be freely mixed with water and salt solutions in various ratios to achieve a range of densities from 1 to 1.2 g/cm³ and therefore lower minimum trap pressures. The material in solution has a higher viscosity than water (e.g. it is an alternative to using plasma or dextrose solutions), so acoustic streaming effects may be further minimized. It is also an attenuating medium so chamber resonances may be reduced.

Scaling the current chamber geometry down more than a factor of 6 introduces

new problems. Transducer aperture sizes below 3 mm are not standard manufacturer offerings and visualization of column formations become difficult without magnification (i.e. microscope assemblies). Microfabrication of the chamber and transducer may be required. Various microfabrication transducer designs are under investigation by several authors.^{47,90,91} At heart of these investigations is quantification of the power capabilities and material properties of the transducers. Generally, pressure field measurements and prediction for a given drive voltage are both difficult, owing to the chamber microgeometry and lack of knowledge of the transducer material properties.

8.4. Measurement of Molecular Bonds

With the benefit of the aforementioned improvements, we will be in a position to study the behavior of suspensions of microparticles with and without biologically active coatings. With the aid of Coulter counters or plug-flow cytometry, accurate counts of adhesively bonded particles can be made. Incrementally increasing the chamber pressures and recounting the attached and newly separated particles will lead to determination of a threshold pressure above which a statistically significant quantity of the particles are separated. Assuming only one type of molecular bond is involved, using the force model for suspensions of particles with identical acoustic properties, the molecular bond rupture strength can be calculated based on the threshold pressure.

Other techniques may be used with this for even greater accuracy. Suspensions of particles could be used, consisting of more than one particle type each with very different acoustic properties. For instance, pairs of attached particles could be selected

such that a strong net repulsive force between the particles arises: the primary radiation force pushes one particle to a pressure node and the other particle to a pressure antinode, while the secondary radiation force between the particles is repulsive. The particles may be manufactured with appropriate biologic coatings, or may be biologic cells. For the latter, appropriate forces might be generated by insertion of gas-filled encapsulated microbubbles or other microparticles into the cells. For example, gas-filled encapsulated microbubbles can be phagocytized by neutrophils, aiding in drug delivery.⁹² Successful application of the techniques discussed in this section will lead to successful completion of the long-term research goal.

9. CONCLUSIONS

Beginning with a linear model of a standing wave pressure field, a chamber was designed to match the model based on a plane piston radiator source and a water/air surface reflector. Given established theory that accurately models the pressure field, acoustic radiation theory was applied to predict the forces on particles in the pressure field. Predictions of acoustic transparency, particle trap pressures, and particle column location and dimensions were found to match results of levitation experiments within the chamber. Within the limits of accuracy of the pressure model, acoustic radiation theory was found to apply in these experiments. The force model revealed the parameters of the piston radiator source (e.g. drive voltage, crystal properties) that allow formation of columns of a given width using particles of specific acoustic properties in a chosen medium.

The pressure model was a challenging aspect of this research; the model did not accurately predict the chamber pressure field. A fundamental assumption of the model was that linear theory applies, and a complex chamber-transducer system could be modeled as though contributions from the chamber to the overall system response are negligible. This was not the case; non-linear resonances were present, and the chamber could not be effectively decoupled from the transducer using the current design. Changes to the chamber can eliminate or exploit chamber-transducer coupling, thus allowing the continued use of linear theory. But if it turns out non-linear resonances still exist in the new chamber, non-linear acoustic theory will need to be employed.

Our investigation into particle levitation experiments did teach us much. It was discovered that other processes such as acoustic streaming and cavitation were indirectly generated by the acoustic radiation due to the high pressures required for the particle levitation. These processes are complex in nature, and cannot be modelled easily. By employing methods to minimize these processes, it can be assumed their contributions to the pressure and force models are negligible. It is anticipated that pressures required to levitate biological cells will match or exceed the pressures used thus far, so mitigation of these processes is essential. Low attenuation phantoms, static pressurization and scaled down chambers will be the methods of choice for future research.

Prediction of intercellular molecular bond rupture strengths is not simple, but now appears possible. Assuming linear acoustic theory can be used pressures and forces in a scaled down chamber can be predicted with confidence. Along with the addition of secondary radiation forces and introduction of a variable describing the molecular bond rupture strength, the force model can be extended to identify the minimum pressure required to break a specific molecular bond. Combined with plug-flow cytometry for statistical analysis of attached particles, these measurements may prove more useful and accurate than current discrete particle analysis methods such as laser tweezers and atomic force microscopy.

APPENDIX A. COMPREHENSIVE EQUIPMENT LIST

1. Electronic Components

- (a) LeCroy LW420B Wavestation arbitrary waveform generator
- (b) ENI 240L 40 Watt radio frequency linear power amplifier
- (c) ENI 3100LA 100 Watt radio frequency linear power amplifier
- (d) LeCroy Waverunner LT342 oscilloscope
- (e) LeCroy Wavepro 940 oscilloscope
- (f) Panametrics 5900PR pulser/receiver
- (g) Miteq AU-1324-8260-1179/WP-BNC preamplifier
- (h) Matec DIP-3 diplexer
- (i) Kay Elemetrics 837 manual step attenuator
- (j) Mini-Circuits 1.9 MHz 50 Ohm coaxial low pass filter
- (k) 50 Ohm coaxial cable with BNC and UHF male connectors as needed

2. Transducers

- (a) Valpey Fisher ILO506HR diagnostic immersion transducer
- (b) Etalon LIHP-40-.5019-SCB1 immersion transducer
- (c) Valpey Fisher E0107 immersion transducer

3. Hydrophones and Hydrophone Holder

- (a) Specialty Engineering Associates PVDFZ44-0400 0.4 mm diameter polymer needle hydrophone
- (b) Specialty Engineering Associates A101dB hydrophone preamplifier
- (c) Needle hydrophone brass support collar
- (d) Hydrophone collar aluminum adaptors for positioning equipment

4. Positioning Equipment and Laboratory Table

- (a) Parker Daedal XYZ positioner with Galil motion controller
- (b) Velmex A4012Q1-S4 XYZ graduated knob Unislide assembly with A5990BSTK rotary table
- (c) Fisher Scientific jack stand
- (d) Technical Manufacturing Corporation 63-553 laboratory vibration damping table with active gimball pneumatic pistons

5. Levitation Chamber

- (a) Walls (clear cast acrylic tubing, 140 mm outer diameter/ 13 mm wall thickness)
- (b) Base plate (extruded acrylic sheet, 12.7 mm thickness)
- (c) Support base (unfilled nylon rod, 150 mm diameter)
- (d) GE Silicones interior rubber sealant
- (e) Transducer custom O-rings
(RTV silicon moldmaking rubber with activator,

38 mm diameter copper mixing pot,
19 mm diameter aluminum transducer mockups)

- (f) Westlake Plastics TPX DX845 clear film
- (g) Agar-silicon carbide low-attenuation phantoms
- (h) Silicon vacuum grease
- (i) Rubber test swatches
 - i. Silicon foam rubber
 - ii. Polyurethane rubber
 - iii. Natural latex rubber
 - iv. So-Abs rubber

6. Lighting and Photography Equipment

- (a) Dolan-Jenner Industries Inc. Fiber Lite 181 dual gooseneck high intensity fiber optic illuminator
- (b) Opti-Quip 1200 mercury arc lamp
- (c) Edmund Industrial Optics 25 mm² extended hot mirrors
(425-675 nm transmission/ 750-1150 nm reflection)
- (d) Oriel Instruments optical mounting rods and holders
- (e) 150 mm metal ruler with metric scale
- (f) Olympus Camedia C3030 digital zoom camera
- (g) Olympus Digital Optics V-37 polarizing light filter

(h) Tripod assembly base

7. Particles and Particle Handling Equipment

(a) Denver Instruments Co. TR6101 digital scale

(b) °C Thermometer

(c) Glass stirring rods

(d) USA Scientific 10 μl micropipettor

(e) USA Scientific TipOne 10 μl natural pipet tips

(f) 3, 10 and 20 cc syringes with 16 - 30.5 gauge needles

(g) Deionized/ degassed water

(h) Mallinkrodt MP-1950 contrast agent microbubbles

(decafluorobutane, lipid shell wet packaged,

3 μm diameter)

(i) Bangs Laboratories Dynospheres PS07N

(polystyrene wet packaged, Lot 2018,

19.0 \pm 0.8 μm diameter)

(j) Polysciences Polybead 15709 microspheres

(polystyrene wet packaged, Lot 480157,

0.457 \pm 0.010 μm diameter, blue-dyed)

(k) Molecular Probes Fluospheres F-8844

(polystyrene wet packaged, Lot 54A1-1,

15.5 μm diameter, yellow-green fluorescence,
505 nm excitation/ 515 nm emission)

- (l) Expancel 551-DU-20 microbubbles
(isobutane dry packaged, Lot 996201,
9.0 μm diameter)
 - (m) Pierce & Stevens Dualite M6001AE02 microbubbles
(isobutane dry packaged, Lot B9901112,
40.0 μm diameter)
 - (n) Pierce & Stevens Dualite MS7020-02 microbubbles
(isopentane dry packaged Lot B0006156,
30.0 μm diameter)
 - (o) Kingsford cornstarch
 - (p) McCormick food coloring dye (green, yellow, red, blue)
 - (q) Humco glycerine (99.5% purity)
8. Software running on a Dell Optiplex GX1p Pentium computer
- (a) Microsoft Windows NT
 - (b) Microsoft Office 97
 - (c) Mathworks Matlab 5.3
 - (d) National Instruments Labview 5.1 and 6.0
 - (e) Olympus Camedia Master 2.0 and Adobe Photoshop 5.5

(f) Adobe Illustrator 8.01

(g) WinEdt 5 and LaTeX 2e

REFERENCES

1. T. X. Zhao and B. Jacobson, "Quantitative correlations among fibrinogen concentration, sedimentation rate and electrical impedance of blood," *Medical and Biological Engineering and Computing* **35-3**, pp. 181–185, May 1997.
2. N. B. Woodland, K. Cordatos, W. T. Hung, A. Reuben, and L. Holley, "Erythrocyte sedimentation in columns and the significance of ESR," *Biorheology* **33-6**, pp. 477–488, November-December 1996.
3. M. M. Brigden, "The erythrocyte sedimentation rate: still a helpful test when used judiciously," *Postgraduate Medicine* **103-5**, pp. 257–274, May 1998.
4. M. C. Saadeh, "The erythrocyte sedimentation rate: old and new clinical applications," *Southern Medical Journal* **91-3**, pp. 220–225, March 1998.
5. A. Sakanishi, A. Yoshikoshi, and Y. Naito, "Mobility of erythrocyte from sedimentation rate at different osmotic pressures," *Colloids and Surfaces B* **18-2**, pp. 119–124, August 2000.
6. M. Iino, "Effects of a homogeneous magnetic field on erythrocyte sedimentation and aggregation," *Bioelectromagnetics* **18-3**, pp. 215–222, 1997.
7. S. Si, K. Huang, and Y. Fung, "Study of erythrocyte sedimentation behavior by piezoelectric crystal impedence sensor," *Biosensors and Bioelectronics* **14-8/9**, pp. 689–694, December 1999.
8. G. Godin, M. Violleau, and A. Caprani, "Electrochemical analysis of blood cell/substrate interactions under flow conditions," *Biorehology* **32-5**, pp. 571–582, 1995.
9. A. M. Malek, R. Ahlquist, G. H. Gibbons, V. J. Dzau, and S. Izumo, "A cone-plate apparatus for the in vitro biochemical and molecular analysis of the effect of shear stress on adherent cells," *Methods in Cell Science* **17-3**, pp. 165–176, September 1995.
10. J. Fritzand, A. G. Katopodis, F. Kolbringer, and D. Anselmetti, "Force-mediated kinetics of single P-selectin/ligand complexes observed by atomic force microscopy," *Biophysics* **95-21**, pp. 12283–12288, October 1998.
11. M. Radmucher, "Single molecules feel the force," *Physics Today* **54-9**, pp. 33–37, September 1999.
12. C. Gay and L. Leibler, "On stickiness," *Physics Today* **54-11**, pp. 48–52, November 1999.

13. B. S. Edwards, F. W. Kuckuck, E. R. Prossnitz, A. Okun, J. T. Ransom, and L. A. Sklar, "Plug flow cytometry extends analytical capabilities in cell adhesion and receptor pharmacology," *Cytometry* **43-3**, pp. 211–216, March 2001.
14. J. Frohlich and H. Konig, "New techniques for isolation of single prokaryotic cells," *FEMS Microbiology Reviews* **24-5**, pp. 567–572, December 2000.
15. C. Hoyer, S. Monajembashi, and K. O. Greulich, "Light as a microtool: laser microbeams and optical tweezers in molecular and cellular biotechnology," *Science Progress* **79-3**, pp. 233–254, 1996.
16. E. Evans, A. Leung, D. Hammer, and S. Simon, "Chemically distinct transition states govern rapid dissociation of single L-selectin bonds under force," *Proceedings of the National Academy of Sciences* **98-7**, pp. 3784–3789, March 2001.
17. G. Kada, L. Blayney, L. H. Jeyakumar, F. Kienberger, V. P. Pastushenko, S. Fleischer, H. Schindler, F. A. Lai, and P. Hinterdorfer, "Recognition force microscopy/spectroscopy of ion channels: applications to the skeletal muscle Ca^{2+} release channel (RYR1)," *Ultramicroscopy* **86-1/2**, pp. 129–137, January 2001.
18. A. Ashkin, "Optical trapping and manipulation of neutral particles using lasers," *Proceedings of the National Academy of Sciences* **94-10**, pp. 4853–4860, May 1997.
19. Z. Ulanowski and I. K. Ludlow, "Compact optical trapping microscope using a diode laser," *Measurement Science and Technology* **11-12**, pp. 1778–1785, December 2000.
20. K. Konig, "Laser tweezers and multiphoton microscopes in life sciences," *Histochemistry and Cell Biology* **114**, pp. 79–92, 2000.
21. M. W. Berns, "Laser scissors and tweezers," *Scientific American* **278-4**, pp. 52–57, April 1998.
22. Y. C. Jong, H. M. Chen, J. H. Hsu, and W. S. Fann, "Constructions and applications of a simple optical tweezers," *Zoological Studies* **34 Supp. 1**, pp. 209–211, 1995.
23. G. Rempe, "Quantum mechanics with single atoms and photons," *Physics Today* **55-12**, pp. 37–42, December 2000.
24. S. Chu, "Laser trapping of neutral particles," *Scientific American* **266-2**, pp. 71–76, February 1992.
25. C. G. Baumann, S. B. Smith, V. A. Bloomfield, and C. Bustamante, "Ionic effects on the elasticity of single DNA molecules," *Proceedings of the National Academy of Sciences* **94-12**, pp. 6185–6190, June 1997.

26. S. B. Smith, Y. Cui, and C. Bustamante, "Overstretching *B*-DNA: the elastic response of individual double-stranded and single-stranded DNA molecules," *Science* **271**, pp. 795–798, February 1996.
27. Y. Cui and C. Bustamante, "Pulling a single chromatin fiber reveals the forces that maintain its higher-order structure," *Proceedings of the National Academy of Sciences* **97-1**, pp. 127–132, January 2000.
28. T. Nishizaka, R. Seo, H. Tadakuma, K. Kinosita, and S. Ishiwata, "Characterization of single actomyosin rigor bonds: load dependence of lifetime and mechanical properties," *Biophysical Journal* **79-2**, pp. 962–974, August 2000.
29. N. Ponelies, J. Scheef, A. Harim, G. Leitz, and K. O. Geulich, "Laser micromanipulators for biotechnology and genome research," *Journal of Biotechnology* **35**, pp. 109–120, 1994.
30. S. C. Kuo and M. P. Sheetz, "Force of single kinesin molecules measured with optical tweezers," *Science* **260**, pp. 232–234, April 1993.
31. S. Henon, G. Lenormand, A. Richert, and F. Gillet, "A new determination of the shear modulus of the human erythrocyte membrane using optical tweezers," *Biophysical Journal* **76-2**, pp. 1145–1151, February 1999.
32. L. M. Walker, A. Holm, L. Cooling, L. Maxwell, A. Oberg, T. Sundqvist, and A. J. E. Haj, "Mechanical manipulation of bone and cartilage cells with optical tweezers," *FEBS Letters* **459-1**, pp. 39–42, October 1999.
33. T. Tlusty, A. Meller, and R. Bar-Ziv, "Optical gradient forces of strongly localized fields," *Physical Review Letters* **81-8**, pp. 1738–1741, August 1998.
34. W. T. Coakley, G. Whitworth, M. A. Grundy, R. K. Gould, and R. Allman, "Ultrasonic manipulation of particles and cells," *Bioseparations* **4-2**, pp. 73–83, 1994.
35. K. Higashitani, M. Fukushima, and Y. Matsuno, "Migration of suspended particles in plane stationary ultrasonic fields," *Chemical Engineering Science* **36-12**, pp. 1877–1882, 1981.
36. T. L. Tolt, *Agglomeration and collection of fine secondary phases in flowing suspensions utilizing resonant ultrasonic fields*. PhD thesis, Case Western Reserve University, August 1990.
37. T. L. Tolt and D. L. Feke, "Separation of dispersed phases from liquids in acoustically driven chambers," *Journal of Engineering Science* **48-3**, pp. 527–540, 1993.

38. K. Yasuda, S. Umemura, and K. Taked, "Concentration and fractionation of small particles in liquid by ultrasound," *Japanese Journal of Applied Physics* **1-5B**, pp. 2715–2720, May 1995.
39. S. Gupta, "Fractionation of mixed particulate solids according to compressibility using ultrasonic standing waves," *Chemical Engineering Science* **50-20**, pp. 3275–3284, 1998.
40. O. Doblehoff-Dier, T. Gaida, H. Katinger, W. Burger, M. Groschl, and E. Benes, "A novel ultrasonic resonance field device for the retention of animal cells," *Biotechnology Progress* **10**, pp. 428–432, 1994.
41. K. Yasuda, S. Haupt, S. S. Umemura, T. Toyi, M. Nishida, and Y. Shibata, "Using acoustic radiation force as a concentration method for erythrocytes," *Journal of the Acoustical Society of America* **102-1**, pp. 642–645, July 1997.
42. M. Groschl, "Ultrasonic separation of suspended particles I. fundamentals," *Acustica* **84-3**, pp. 432–447, May-June 1998.
43. M. Groschl, "Ultrasonic separation of suspended particles II. design and operation of separation devices," *Acustica* **84-4**, pp. 632–642, July-August 1998.
44. M. Groschl, W. Burger, B. Handl, O. Doblhoff-Dier, T. Gaida, and C. Schmatz, "Ultrasonic separation of suspended particles III. application in biotechnology," *Acustica* **84-5**, pp. 815–822, September-October 1998.
45. S. M. Woodside, B. D. Bower, and J. M. Piret, "Measurement of ultrasonic forces for particle-liquid separations," *Journal of the American Institute of Chemical Engineers* **43-7**, pp. 1727–1736, July 1997.
46. S. M. Woodside, J. M. Piret, M. Groschl, E. Benes, and B. D. Bower, "Acoustic force distribution in resonators for ultrasonic particle separation," *Journal of the American Institute of Chemical Engineers* **44-9**, pp. 1976–1984, September 1998.
47. A. W. Wang, A. H. Meng, and R. M. White, "Ultrasonic sample concentration for microfluidic systems." Lawrence Livermore National Laboratory, June 2000.
48. L. A. Crum, "Acoustic force on a liquid droplet in an acoustic standing wave," *Journal of the Acoustical Society of America* **50-1 Pt. 2**, pp. 157–163, February 1971.
49. G. Whitworth and W. T. Coakley, "Particle column formation in a stationary ultrasonic field," *Journal of the Acoustical Society of America* **91-1**, pp. 79–84, January 1992.
50. M. A. H. Weiser and R. E. Apfel, "Interparticle forces on red blood cells in a standing wave field," *Acustica* **56-2**, pp. 114–119, October 1984.

51. G. T. Haar and S. J. Wyard, "Blood cell banding in ultrasonic standing wave fields: a physical analysis," *Ultrasound in Medicine and Biology* **4-2**, pp. 111–123, 1978.
52. H. M. Hertz, "Standing-wave acoustic trap for noninvasive positioning of microparticles," *Journal of Applied Physics* **78-8**, pp. 4845–4849, October 1995.
53. G. W. C. Kaye and T. H. Laby, *Tables of Physical and Chemical Constants*, Longman, New York, 1986.
54. M. Greenspan and C. Tschiegg, "Tables of the speed of sound in water," *Journal of the Acoustical Society of America* **31-1**, pp. 75–76, January 1959.
55. A. Eller, "Force on a bubble in a standing acoustic wave," *Journal of the Acoustical Society of America* **43**, pp. 170–171, September 1967.
56. R. Lofsted and S. Putterman, "Theory of long wavelength acoustic radiation pressure," *Journal of the Acoustical Society of America* **90-4**, pp. 2027–2033, October 1991.
57. L. Brillouin, *Tensors in Mechanics and Elasticity*, Academic Press, New York, 1964.
58. L. E. Kinsler, A. B. Coppas, A. R. Frey, and J. V. Sanders, *Fundamentals of Acoustics*, John Wiley and Sons, New York, 3rd ed., 1982.
59. K. Yosioka and Y. Kawasima, "Acoustic radiation pressure on a compressible sphere," *Acustica* **5**, pp. 167–173, 1955.
60. J. Wu and G. Du, "Acoustic radiation force on a small compressible sphere in a focussed beam," *Journal of the Acoustical Society of America* **87-3**, pp. 997–1003, March 1990.
61. C. P. Lee and T. G. Wang, "Acoustic radiation force on a bubble," *Journal of the Acoustical Society of America* **93-3**, pp. 1637–1640, March 1993.
62. L. A. Crum and A. Properetti, "Nonlinear oscillations of gas bubbles in liquids: an interpretation of some experimental results," *Journal of the Acoustical Society of America* **73-1**, pp. 121–127, January 1983.
63. A. A. Doinikov, "Acoustic radiation force on a spherical particle in a viscous heat-conducting fluid I. general formula," *Journal of the Acoustical Society of America* **101-2**, pp. 713–721, February 1997.
64. A. A. Doinikov, "Acoustic radiation force on a spherical particle in a viscous heat-conducting fluid II. force on a rigid sphere," *Journal of the Acoustical Society of America* **101-2**, pp. 722–730, February 1997.
65. A. A. Doinikov, "Acoustic radiation force on a spherical particle in a viscous heat-conducting fluid III. force on a liquid drop," *Journal of the Acoustical Society of America* **101-2**, pp. 731–740, February 1997.

66. A. A. Doinikov, "Acoustic radiation force on a bubble: viscous and thermal effects," *Journal of the Acoustical Society of America* **103-1**, pp. 143–146, January 1998.
67. T. J. Asaki and P. L. Marston, "Acoustic radiation force on a bubble driven above resonance," *Journal of the Acoustical Society of America* **96-5 Pt. 1**, pp. 3096–3099, November 1994.
68. A. Prosperetti, "Bubble phenomena in sound fields: part two," *Ultrasonics* **22-3**, pp. 115–121, May 1984.
69. V. N. Alekseev, "Force produced by the acoustic radiation pressure on a sphere," *Akust. Zh. (Soviet Physics-Acoustics)* **29-2**, pp. 77–80, March/April 1983.
70. T. Hasegawa, N. Inoue, and K. Matsuzawa, "A new rigorous expansion for the velocity potential of a circular piston source," *Journal of the Acoustical Society of America* **74-3**, pp. 1044–1047, September 1983.
71. T. Hasegawa, T. Kido, N. Inoue, and K. Matsuzawa, "Acoustic radiation force on a rigid sphere in the near field of a circular piston vibrator," *Journal of the Acoustical Society of America* **88-3**, pp. 1578–1583, September 1990.
72. L. P. Gor'kov, "On the forces acting on a small particle in an acoustical field in an ideal fluid," *Soviet Physics Doklady - English Translation* **6**, pp. 773–775, 1962.
73. P. Gonnard, P. Champ, and L. Eyraud, "Characterization of piezoelectric ceramics for high power transducers," in *Power Sonics and Ultrasonic Transducer Design*, 1988.
74. A. A. Doinikov, "Radiation force due to a spherical sound field on a rigid sphere in a viscous fluid," *Journal of the Acoustical Society of America* **96-5/1**, pp. 3100–3105, November 1994.
75. L. A. Crum, "Bjerknes forces on a bubble in a stationary sound field," *Journal of the Acoustical Society of America* **57-6 Pt.1**, pp. 1363–1370, June 1975.
76. J. Spengler and M. Jekel, "Ultrasound conditioning of suspensions - studies of streaming influence on particle aggregation on a lab- and pilot-plant scale," *Ultrasonics* **38-5**, pp. 624–628, March 2000.
77. A. R. Williams, *Ultrasonic biological effects and potential hazards*, Academic Press-Medical Science Series, 1983.
78. T. J. Asaki, *Shape oscillations of bubbles in H₂O driven by modulated ultrasonic radiation pressure and applications to interfacial dynamics*. PhD thesis, Washington State University, May 1995.

79. J. W. Wladimiroff and D. G. Talbert, "The changing fine structure of erythrocyte formations when trapped in ultrasonic standing waves," *Physical Medicine and Biology* **18**, pp. 888–891, 1973.
80. Dintenfass, *Blood microrheology - viscosity factors in blood flow, ischemia and thrombosis*, Butterworth Press, 1971.
81. L. Pederson and A. Selfridge, "Tables of material properties." Specialty Engineering Associates Website, December 2000.
82. J. A. Jensen, *Field II Simulation Program*. Department of Information Technology, Building 344, Technical University of Denmark, DK-2000, Lyngby, Denmark.
83. M. A. H. Weiser and R. E. Apfel, "Extension of acoustic levitation to include the study of micro-size particles in a more compressible host liquid," *Journal of the Acoustical Society of America* **71-5**, pp. 1261–1268, May 1982.
84. E. L. Madsen, J. A. Zagzebski, R. A. Banjavie, and R. Jutila, "Tissue mimicking materials for ultrasound phantoms," *Medical Physics* **5-5**, pp. 391–395, September/October 1978.
85. A. R. Selfridge, "Approximate material properties in isotropic materials," *IEEE Transactions on Sonics and Ultrasonics* **50SU-32-3**, pp. 381–384, May 1985.
86. E. L. Madsen. Personal correspondence, October 2001.
87. F. Dunn, P. D. Edmonds, and W. J. Fry, "Absorption and dispersion of ultrasound in biological media," in *Biological Engineering*, H. P. Schwann, ed., vol. 9 of *Inter-University Electronic Series*, ch. 3, p. 214, McGraw Hill, 1982.
88. P. Collas and M. Barmatz, "Acoustic radiation potential on a sphere in plane, cylindrical, and spherical standing wave fields," *Journal of the Acoustical Society of America* **77-3**, pp. 928–945, March 1985.
89. P. Collas, M. Barmatz, and C. Shipley, "Acoustic levitation in the presence of gravity," *Journal of the Acoustical Society of America* **86-2**, pp. 777–787, August 1989.
90. M. Koch, N. Harris, A. G. R. Evans, N. M. White, and A. Brunnsweiler, "A novel micro-machined pump based on thick film piezoelectric actuation," *Sensors and Actuators A* **70**, pp. 98–103, 1998.
91. X. Zhu and E. S. Kim, "Microfluidic motion generation with acoustic waves," *Sensors and Actuators A* **66-2**, pp. 355–360, April 1998.
92. P. Dayton, J. Chomas, A. Lum, S. Simon, and K. Ferrara, "Acoustical and physical dynamics of phagocytosed microbubble contrast agents," in *2000 IEEE Ultrasonics*

Symposium. Proceedings., S. Schneider, M. Levy, and B. McAvoy, eds., vol. 2, pp. 1877–80, 2000.